ISSN 2838-0037 (Print)
ISSN 3154-8016 (Online)

Malaysian Journal of Energy and Applications

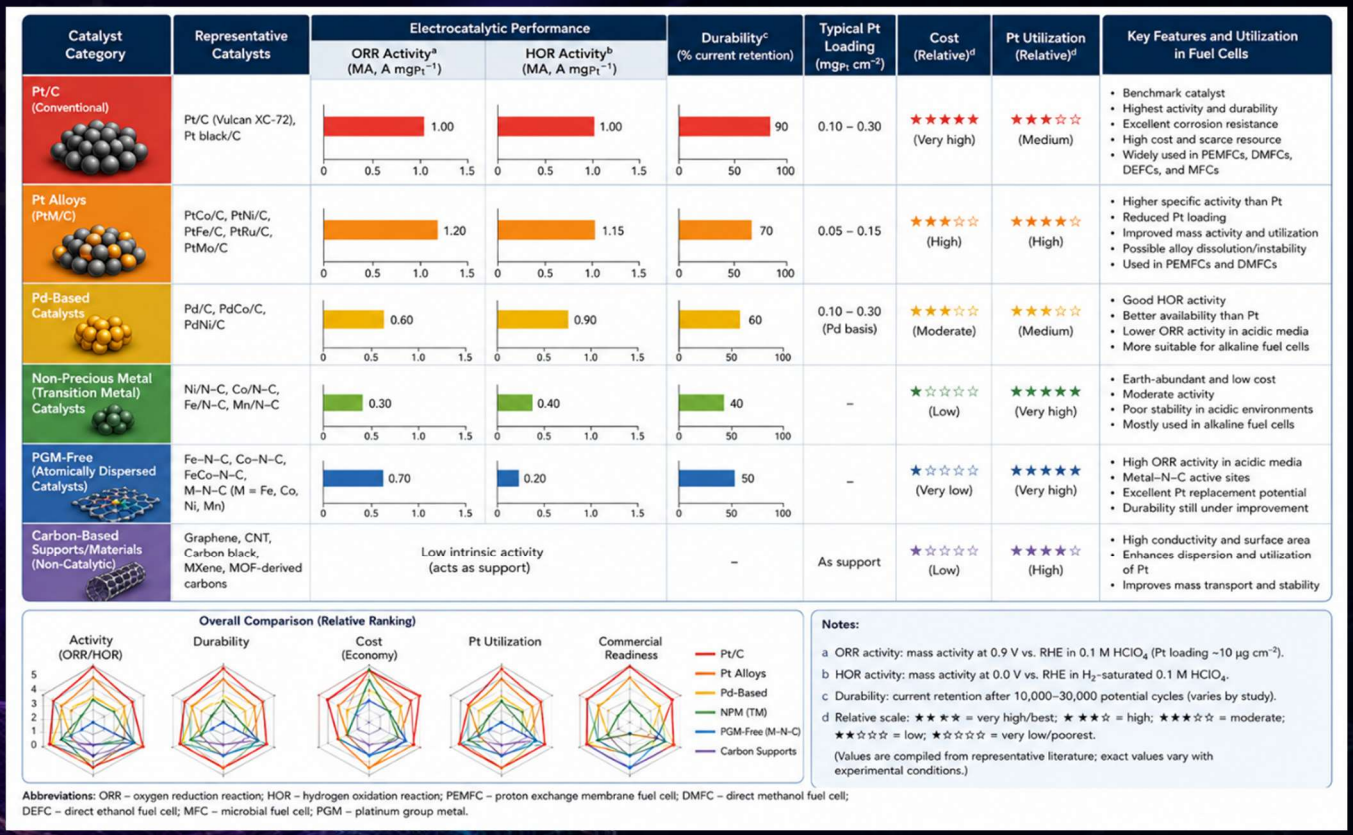

Catalyst Category	Representative Catalysts	Electrocatalytic Performance: ORR Activity[a] (MA, A mg_{Pt}^{-1})	Electrocatalytic Performance: HOR Activity[b] (MA, A mg_{Pt}^{-1})	Durability[c] (% current retention)	Typical Pt Loading (mg_{Pt} cm^{-2})	Cost (Relative)[d]	Pt Utilization (Relative)[d]	Key Features and Utilization in Fuel Cells
Pt/C (Conventional)	Pt/C (Vulcan XC-72), Pt black/C	1.00	1.00	90	0.10 – 0.30	★★★★★ (Very high)	★★★☆☆ (Medium)	• Benchmark catalyst • Highest activity and durability • Excellent corrosion resistance • High cost and scarce resource • Widely used in PEMFCs, DMFCs, DEFCs, and MFCs
Pt Alloys (PtM/C)	PtCo/C, PtNi/C, PtFe/C, PtRu/C, PtMo/C	1.20	1.15	70	0.05 – 0.15	★★★☆☆ (High)	★★★★☆ (High)	• Higher specific activity than Pt • Reduced Pt loading • Improved mass activity and utilization • Possible alloy dissolution/instability • Used in PEMFCs and DMFCs
Pd-Based Catalysts	Pd/C, PdCo/C, PdNi/C	0.60	0.90	60	0.10 – 0.30 (Pd basis)	★★★☆☆ (Moderate)	★★★☆☆ (Medium)	• Good HOR activity • Better availability than Pt • Lower ORR activity in acidic media • More suitable for alkaline fuel cells
Non-Precious Metal (Transition Metal) Catalysts	Ni/N–C, Co/N–C, Fe/N–C, Mn/N–C	0.30	0.40	40	–	★☆☆☆☆ (Low)	★★★★★ (Very high)	• Earth-abundant and low cost • Moderate activity • Poor stability in acidic environments • Mostly used in alkaline fuel cells
PGM-Free (Atomically Dispersed Catalysts)	Fe–N–C, Co–N–C, FeCo–N–C, M–N–C (M = Fe, Co, Ni, Mn)	0.70	0.20	50	–	★☆☆☆☆ (Very low)	★★★★★ (Very high)	• High ORR activity in acidic media • Metal–N–C active sites • Excellent Pt replacement potential • Durability still under improvement
Carbon-Based Supports/Materials (Non-Catalytic)	Graphene, CNT, Carbon black, MXene, MOF-derived carbons	Low intrinsic activity (acts as support)		–	As support	★☆☆☆☆ (Low)	★★★★☆ (High)	• High conductivity and surface area • Enhances dispersion and utilization of Pt • Improves mass transport and stability

Notes:

a ORR activity: mass activity at 0.9 V vs. RHE in 0.1 M $HClO_4$ (Pt loading ~10 μg cm^{-2}).

b HOR activity: mass activity at 0.0 V vs. RHE in H_2-saturated 0.1 M $HClO_4$.

c Durability: current retention after 10,000–30,000 potential cycles (varies by study).

d Relative scale: ★★★★ = very high/best; ★★★☆ = high; ★★★☆☆ = moderate; ★★☆☆☆ = low; ★☆☆☆☆ = very low/poorest.

(Values are compiled from representative literature; exact values vary with experimental conditions.)

Abbreviations: ORR – oxygen reduction reaction; HOR – hydrogen oxidation reaction; PEMFC – proton exchange membrane fuel cell; DMFC – direct methanol fuel cell; DEFC – direct ethanol fuel cell; MFC – microbial fuel cell; PGM – platinum group metal.

Vol. 1 | Issue 1 | June 2026

MALAYSIAN JOURNAL OF ENERGY AND APPLICATIONS (MyJEA)

Volume 1 | Issue 1 | June 2026

Published by:

Fuel Cell Institute (SELFUEL)
Universiti Kebangsaan Malaysia
43600 UKM Bangi, Selangor Darul Ehsan, Malaysia
Email: selfuel@ukm.edu.my
Website: https://www.ukm.my/myjea

Publication Frequency:

Published Semi-Annually (June and December)

ISSN (Print): 2838-0037
ISSN (Online): 3154-8016

On the Cover: The cover feature highlights a comparative evaluation of platinum and alternative electrocatalysts in fuel cells, showcasing their electrocatalytic performance, durability, and cost-effectiveness.
Featured Article: Elham, O. S. J., Kamarudin, S. K., Zakaria, Z., Ahmad Zaidi, N. H., Azad, A. K., & Osman, S. H. (2026). *Platinum Catalysis in Fuel Cell: An Overview*. Malaysian Journal of Energy and Applications, 1(1), 84–98.

EDITORIAL BOARD

TABLE OF CONTENTS

PREFACE

The Malaysian Journal of Energy and Applications (MyJEA) is a peer-reviewed academic journal published by the Fuel Cell Institute (SELFUEL), Universiti Kebangsaan Malaysia (UKM). The journal serves as a premier international platform dedicated to disseminating high-quality original research, technical innovations, and critical reviews across all domains of clean energy systems, fuel cell science, electrochemistry, and green technology applications.

This inaugural issue (Volume 1, Issue 1, 2026) features five high-impact articles addressing fundamental and applied advances in energy conversion technology:

1. Microbial Fuel Cells (MFCs): A diagnostic framework examining internal resistance, bioanode charge transfer, and physical contact degradation.
2. Direct Methanol Fuel Cells (DMFCs): A comparative structural evaluation of conventional membrane electrode assemblies versus microfluidic membrane-less architectures.
3. Composite Membranes for Electrolysis: The optimization of quaternized PVA/GO anion exchange membranes tailored for green hydrogen generation.
4. System Dynamic Modeling: Temperature-dependent simulation of a 400-cell PEMFC stack operating under dynamic dynamic loading using MATLAB-Simscape.
5. Electrocatalysis Overview: A critical review of platinum catalysts, low-loading strategies, core-shell architectures, and PGM-free alternatives.

Through these contributions, MyJEA aims to support the global clean energy transition and align research efforts with the United Nations Sustainable Development Goals, specifically SDG 7 (Affordable and Clean Energy) and SDG 13 (Climate Action).

Editor-in-Chief
Malaysian Journal of Energy and Applications (MyJEA)
Fuel Cell Institute (SELFUEL), Universiti Kebangsaan Malaysia

Malaysian Journal of Energy and Applications 1 (2026): 1-23
https://doi.org/10.17576/myjea.2026.01.1

QUANTIFYING SYNERGISTIC ENERGY LOSSES INDUCED BY INTERNAL RESISTANCE IN MICROBIAL FUEL CELL BIOANODES: THE ROLE OF PHYSICAL CONNECTIVITY AND IONIC STRENGTH

Nor Syazwanie Mohd Saidi, Muhammad Farhan Hil Me, Yashawini Phriya Rauichandran, Ryan Yow Zhong Yeo, Mohammad Sherjeel Javed Khan, Swee Su Lim*

Fuel Cell Institute (SELFUEL), Universiti Kebangsaan Malaysia, 43600 UKM Bangi, Selangor, Malaysia

**Corresponding author: limss@ukm.edu.my*

Received 4/4/2026; Received in Revised Form 13/6/2026; Accepted 13/6/2026; Available Online 20/07/2026.

Abstract

Internal resistance R_{int} is a critical bottleneck that dictates the power output and efficiency of microbial fuel cells (MFCs). This study investigates the synergistic impact of gradated internal resistance on bioanode performance by systematically manipulating electrode contact integrity to establish three distinct R_{int} levels: 20 Ω (Group 1), 60 Ω (Group 2), and 182 Ω (Group 3). Results indicate that elevated R_{int} triggers a cascade of potential energy losses; Group 3 exhibited a 22% reduction in peak power density (0.07 W/m^2) compared to the optimized Group 1 (0.09 W/m^2). Electrochemical Impedance Spectroscopy (EIS) identified the anodic interface as the primary site of degradation, with interfacial resistance (R_2) surging from 3 Ω in Group 1 to 140.19 Ω in Group 3. Cyclic Voltammetry (CV) revealed that high R_{int} might have altered the redox behavior in the electrogenic biofilm, evidenced by a +0.36 V positive transition in midpoint potential (E_{mid}), suggesting increased electrochemical energy demand and altered apparent redox behavior. Furthermore, sensitivity analysis via One-Factor-at-a-Time (OFAT) optimization identified a 10:5:50 mM (NaAc:NH4Cl:PBS) electrolyte ratio as optimal, driving current density to a peak of ≈ 2.1 A/m^2 by mitigating secondary chemical bottlenecks. These findings suggest that poor connection is not merely a hardware failure but an electrochemical stress factor that affects the catalytic response of the bioelectrochemical interface.

Keywords: Bioanode kinetics, internal resistance gradation, electrochemical impedance spectroscopy (EIS), charge transfer resistance, microbial electron transfer pathways.

Introduction

The escalating trajectory of global energy consumption and the concomitant surge in wastewater contamination represent two of the most formidable challenges of the 21st century. As of 2026, global energy demand continues to rise, driven by industrialization and population growth, while "water bankruptcy"—the state where water demand exceeds sustainable supply—afflicts nearly one-third of the world's population (Wang et al., 2026). Environmental pollution has reached critical levels, with untreated industrial and domestic effluents severely degrading aquatic ecosystems worldwide (Boutarbouch et al., 2026; Kurniawan et al., 2026). These challenges directly impede the progress of the United Nations Sustainable Development

Goals (SDGs), specifically SDG 6 (Clean Water and Sanitation) and SDG 7 (Affordable and Clean Energy), which mandate a global shift toward sustainable resource recovery (Baba et al., 2026; Saghir et al., 2026). Locally, this claim is strengthened by the National Energy Policy (DTN) 2022–2040 and the Water Sector Transformation 2040 (WST 2040), which emphasize Malaysia's commitment to achieving a low-carbon economy and a circular water cycle through the adoption of indigenous, high-efficiency green technologies (Rani et al., 2025).

Traditional wastewater management relies heavily on conventional biological treatments, such as activated sludge processes. While effective, these methods are characterized by massive energy footprints, primarily due to the aeration required to oxidize organic and inorganic contaminants to meet standard discharge values for Chemical Oxygen Demand (COD) and Biochemical Oxygen Demand (BOD) (Ravindran et al., 2025). Globally, discharge standards are becoming increasingly stringent; for instance, many international frameworks now mandate BOD levels below 10–20 mg/L before environmental release. Locally, the Department of Environment (DOE) Malaysia enforces the Environmental Quality (Industrial Effluents) Regulations, which categorize discharge into Standard A (for upstream catchments) and Standard B (for downstream areas), necessitating advanced treatment to reach these benchmarks (*Environmental Requirements: A Guide For Investors* 2010).

Beyond biological methods, alternative treatments such as advanced electrochemical oxidation (EO), adsorption, and chemical precipitation are frequently employed to meet stringent discharge standards, such as Standard A and B enforced by the Department of Environment (DOE) Malaysia. Advanced electrochemical oxidation (EO) utilizes electrical energy to generate highly reactive hydroxyl radicals (·OH) at an anode to mineralize complex pollutants, such as textile dyes or landfill leachate, into CO_2 and water (Solomon et al., 2020; Wilk et al., 2022). In contrast, adsorption is a surface-based phenomenon where molecules adhere to solids like activated carbon or biochar to remove pharmaceutical residues or heavy metals, while chemical precipitation utilizes reagents like lime or alum to turn dissolved contaminants into insoluble solids for sedimentation (Nemeș et al., 2026). Although effective, these technologies incur high operational costs due to significant electrical energy inputs and the continuous requirement for chemical reagents, highlighting the need for passive, energy-recovering alternatives like Microbial Fuel Cells (MFCs) (Feng et al., 2024).

Microbial Fuel Cells (MFCs) have emerged as a transformative technology capable of simultaneous wastewater treatment and bioelectricity generation. The core principle involves the use of electrochemically active microorganisms to catalyze the oxidation of organic matter in wastewater, converting chemical energy directly into electrical energy (Feng et al., 2024; Musa et al., 2026). A typical microbial fuel cell (MFC) functions through the coordinated action of several essential components: an anode where anaerobic microbes oxidize substrates like acetate to release electrons and protons, a cathode where these electrons arriving via an external circuit combine with protons and an oxygen electron acceptor to form water, and a membrane (such as a Cation Exchange Membrane) that facilitates proton transport while preventing oxygen crossover. Central to this process is the microbial consortium, often enriched from sludge or existing electrochemical systems to establish an electrogenic biofilm that serves as the metabolic engine of the device (Lim et al., 2021; Nawaz et al., 2020; Zadeh et al., 2024).

Despite their potential, the practical application of MFCs is hindered by significant technical bottlenecks that limit power density and scalability (Mahmoud et al., 2022). Literature suggests various strategies for improvement, including electrode modification and optimizing microbial communities (Hegazy et al., 2025; Zadeh et al., 2024). However, a fundamental limiting factor that requires deeper mechanistic understanding is internal

resistance. Internal resistance (R_{int}) plays a pivotal role in the operational efficiency of bioelectrochemical systems (BES), serving as a primary determinant of the manageable power output. In systems such as MFCs, R_{int} is comprised of ohmic, activation, and mass-transport overpotentials which collectively dictate the rate of extracellular electron transfer (EET) (Kanani et al., 2025). As this resistance increases, it significantly impedes the flow of electrons from the electrogenic biofilm to the electrode surface, resulting in a substantial decrease in the overall electrochemical performance of the BES. Consequently, a fundamental objective in BES engineering is to maintain R_{int} at the lowest possible threshold to eliminate potential energy losses and maximize thermodynamic efficiency (Kim et al., 2021).

While many studies focus on the chemical aspects of resistance, such as ionic strength and substrate availability, the impact of physical connectivity—specifically the contact integrity between the electrode and current collector—is often overlooked. Poor physical connections are not merely passive resistors; they may alter the electrochemical environment of the bioanode. To investigate this critical role, three distinct levels of internal resistance were systematically established in this study (20, 60, and 182 Ω) to map the mechanistic insights into electricity generation at the bioanode. The performance of these systems was evaluated by recording and analyzing power and current generation profiles. To provide a high-resolution breakdown of the kinetic bottlenecks, advanced electrochemical characterizations including cyclic voltammetry (CV) and electrochemical impedance spectroscopy (EIS) were utilized. Specifically, these tools allow for the partitioning of charge transfer and interfacial resistances, facilitating a deeper understanding of how physical poor connections escalate activation and mass transport limitation. This study aims to clarify whether bioanode performance degradation is a matter of perception or a direct consequence of poor physical connection integrity.

Unlike previous MFC studies that mainly examined internal resistance through electrode spacing, membrane type, electrolyte conductivity, substrate concentration, or reactor architecture, this study specifically isolates poor physical contact between the electrode and current collector as a controlled source of internal resistance. By creating three resistance levels and combining polarization, EIS, and CV analysis, this work provides a diagnostic framework for identifying how physical connection quality contributes to ohmic, interfacial, activation, and apparent mass-transport losses in MFC bioanodes.

Materials and Methods

Reactor Configuration and Bioanode Enrichment

The experimental architecture, including the schematic of the microbial fuel cell (MFC) and the laboratory-scale assembly, is detailed in Figure 1. Six identical dual-chamber bioelectrochemical systems (BES) were operated as MFCs. Each reactor was constructed from two symmetrical polyacrylic blocks with external dimensions of 70 × 70 × 20 mm (See Figure 1(c)). The internal compartments were precision-fabricated to 50 × 50 × 10 mm, providing a net working volume of 25 mL per chamber. The reactor assembly was secured using four M5 diagonal screws to ensure a leak-proof seal. The electrode assembly and membrane specifications were as follows:

- **Anode:** Plain carbon felt (5 ×5 ×1 cm) served as the bioanode.
- **Cathode:** Carbon felt of identical dimensions, coated with 0.5 mg Pt/cm^2 to facilitate the oxygen reduction reaction (ORR).

- **Membrane:** A cation exchange membrane (CMI-7000, Membrane International Inc.) was positioned between the chambers to mediate proton transport.

Saturated silver-silver chloride (Ag/AgCl) reference electrodes (REs) were utilized to provide a stable potential baseline for all measurements. As illustrated in Figure 1(b), the REs were positioned at a fixed distance of approximately 0.5 cm from the respective working electrodes (anode and cathode) to minimize iR drop during data acquisition. A conversion factor of +0.197 vs. Ag/AgCl was applied to align the data with the Standard Hydrogen Electrodes (SHE) scale at 25°C unless stated otherwise.

Controlled Internal Resistance Gradation

To investigate the critical role of internal resistance and provide mechanistic insights into the resulting bioelectrochemical behavior, a controlled resistance gradient was established across the test groups. The contact integrity between the carbon felt electrodes and the titanium wire connectors (facilitating the external circuit interface) was systematically manipulated to simulate varying degrees of connection quality. These modifications were designed to create three distinct levels of internal resistance (R_{int}) as categorized in Table 1.

Table 1 Experimental Design and Controlled Internal Resistance (R_{int}) Gradation

MFC Group	Connection Integrity	Targeted R_{int} (Ω)	Resistance Multiplier	Research Objective
1	Optimized, high-integrity contact	**20**	1× (Baseline)	Establish baseline bioelectrochemical performance.
2	Moderate manual loosening of Ti-electrode interface	**60**	3×	Study intermediate potential energy losses and kinetic shifts.
3	Significant contact restriction / poor connectivity	**180**	9×	Simulate severe connection gaps and synergistic energy losses.

The internal resistance levels were created by adjusting the physical contact between the carbon felt electrode and the titanium wire current collector. The titanium wire was tied to the carbon felt to provide the electrical connection between the electrode and the external circuit. For the optimized connection condition, the titanium wire was tied firmly to ensure good contact with the carbon felt. For the higher-resistance conditions, the titanium wire was gradually loosened to reduce the contact between the titanium wire and carbon felt. The degree of loosening was adjusted until the desired internal resistance levels were obtained.

The internal resistance was estimated from the voltage response of the MFC under no-load and under-load conditions. The open-circuit voltage was first measured using a digital multimeter under no-load condition. The circuit was then connected to a known external resistance, and the loaded voltage was measured. The internal resistance was calculated by comparing the no-load voltage and loaded voltage with the known external resistance. The reported resistance values of 20, 60, and 182 Ω represent calculated values obtained from these voltage measurements. The measurements were performed before and after the experiment to confirm that the resistance levels remained consistent throughout the operation. This procedure was carried out to ensure that the observed performance differences were mainly related to the controlled physical connection condition rather than uncontrolled changes in the electrode assembly.

All configurations were operated in duplicate to assess reproducibility. This deliberate gradation allowed for the precise mapping of how physical connection gaps—often perceived as minor assembly errors—affect the activation, ohmic, and apparent mass-transport kinetics of the bioanode.

Inoculation and Media Composition

The microbial inoculum was sourced from a combination of sediment collected from the UKM Engineering Lake and an existing microbial fuel cell (MFC) setup that had been in continuous operation for over three years. The inoculation process involved mixing the concentrated sludge with the anodic medium at a 1:1 ratio. The chemical compositions of the electrolytes were:

- **Anolyte:** Sodium acetate (0.41 g/L) as the primary electron donor, supplemented with NH_4Cl (1.07 g/L), KCl (0.11 g/L), $NaH_2PO_4 \cdot 2H_2O$ (0.66 g/L), $Na_2HPO_4 \cdot 2H_2O$ (1.03 g/L), and Wolfe's mineral/vitamin solutions. The basal medium was autoclaved at 121°C for 20 minutes. Post-sterilization, the Wolfe's mineral and vitamin solutions were added via 0.2 µm membrane filtration to prevent thermal degradation. To ensure anaerobic conditions, the completed medium was purged with high-purity nitrogen (N_2) to remove dissolved oxygen prior to use.
- **Catholyte:** A 50 mM phosphate buffer (pH 7.0) comprising $NaH_2PO_4 \cdot 2H_2O$ (3.30 g/L), $Na_2HPO_4 \cdot 2H_2O$ (5.14 g/L), and KCl (0.11 g/L). The catholyte was air-saturated via an aquarium pump to maintain dissolved oxygen (DO) levels above 3 mg/L.

Operational Start-up and Data Acquisition

The complete experimental configuration was assembled as illustrated in Figure 1(a). The anolyte and catholyte were fed independently from 5 L reservoirs into their respective chambers at a constant flow rate of 0.17 mL/min using a multi-channel peristaltic pump. The operational protocol was executed in the following stages:

- **Inoculation:** The inoculum source was injected into the anodic chambers, and the remaining volume was filled with the stock medium.
- **Monitoring:** Potential was monitored via a data logger (Pico ADC-16) and PicoLog software, with data points recorded at 15-minute intervals.
- **Conditioning:** The reactors were initially maintained under open-circuit conditions for 24 hours to establish a baseline potential.
- **Startup:** On the second day, the circuits were closed across a 25 Ω external resistor. Following a 48-hour stabilization period, continuous feeding of the anodic reactors was initiated at the designated flow rate to sustain steady-state power generation.

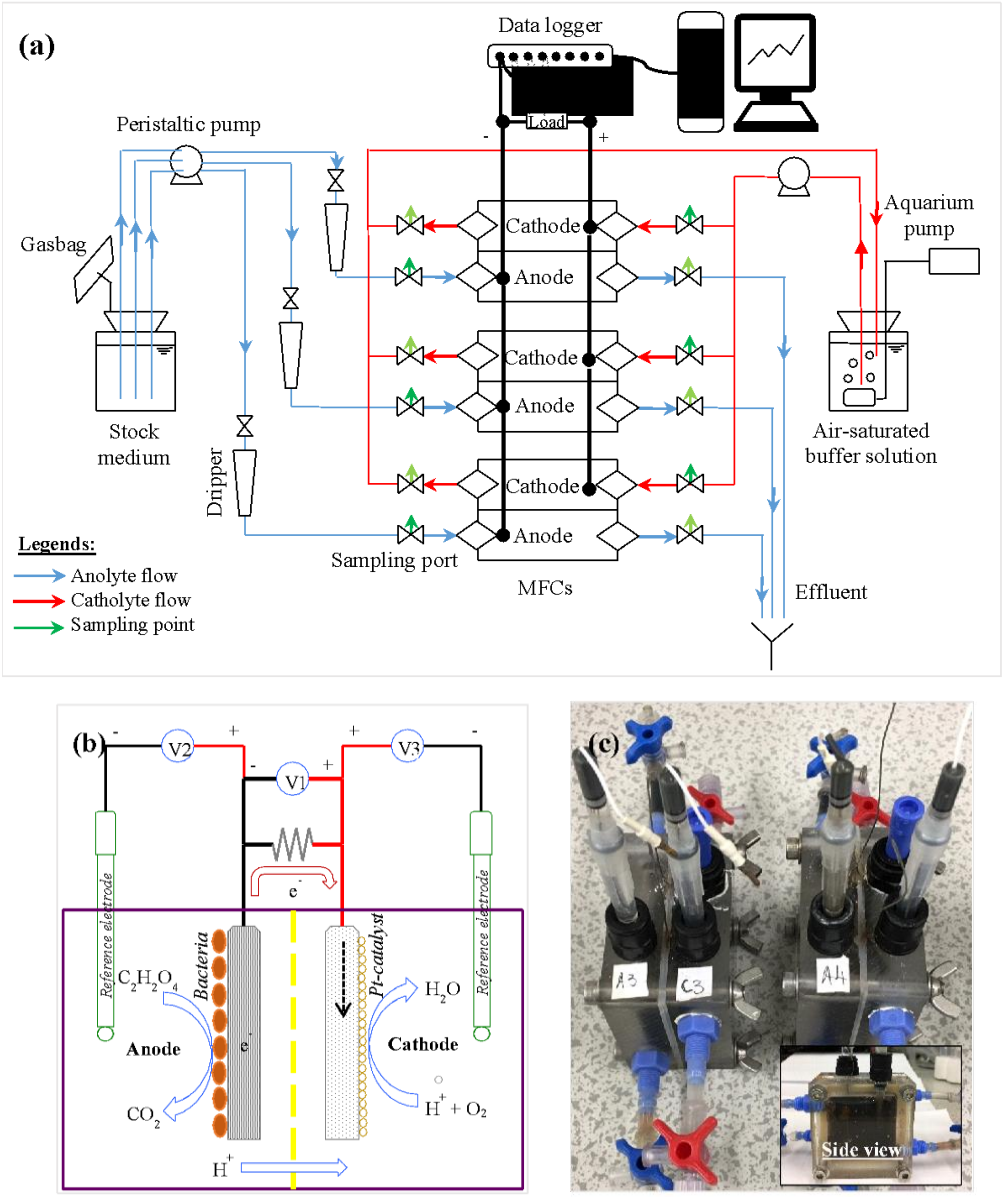

Figure 1 Schematic of (a) experiment arrangement, (b) single MFC and (c) the lab-scale MFCs

Electrochemical Characterization: EIS, CA, and CV

Upon reaching a steady-state power generation plateau (typically after >100 days of continuous operation), the MFCs were subjected to a suite of electrochemical analyses to characterize the internal resistance and kinetic behavior.

Electrochemical Impedance Spectroscopy (EIS)

Comprehensive impedance characterization was performed using a PGSTAT128N potentiostat equipped with an FRA32M frequency response analyzer module (Metrohm, Netherlands). To capture the full spectrum of electrochemical signatures—ranging from high-frequency ohmic shifts to low-frequency diffusion kinetics—measurements were conducted under Open Circuit Potential (OCP) across a frequency range of 100 kHz to 0.01 Hz, utilizing a resolution of 71 data points per logarithmic decade.

To achieve a high-resolution breakdown of the internal resistance (R_{int}), three distinct wiring configurations were employed:

- **Whole-Cell Analysis (2-Terminal):** Quantified the total internal resistance of the MFC, integrating all anodic, cathodic, and membrane-related losses.
- **Half-Cell Analysis (3-Terminal):** Utilized a reference electrode (SHE) to isolate the individual impedance of the bioanode and the abiotic cathode, focusing on the charge transfer resistance (R_1) and interfacial kinetics (R_2).
- **Membrane and Material Interface (4-Terminal):** Employed to measure the specific ohmic drop across the CMI-7000 membrane and the electrolyte, effectively separating bulk solution resistance (R_s) from the electrode-interface phenomena.

The resulting Nyquist and Bode plots were analyzed using Nova 11.1 software by fitting the raw data to a modified R(RQ)(RQT) equivalent circuit model. This approach allowed for the precise quantification of the capacitive element (T), the charge transfer resistance (R_1), and the interfacial resistance (R_2), providing a mechanistic map of the electrochemical bottlenecks within each cell component.

Stepwise Chronoamperometry (CA) and Polarization

To derive the polarization and power density curves, stepwise chronoamperometry was employed. The applied potential was decreased from the OCP to 0 V in decrements of 0.05 V. Each potential step was maintained for at least 15 minutes to ensure the system reached a pseudo-steady state. Only the stabilized current value at the end of each step was recorded for the construction of the polarization profiles.

Cyclic Voltammetry (CV)

Following the polarization tests, the MFCs were allowed to re-equilibrate under normal operating conditions for several days to ensure bioanode recovery. CV was then performed to evaluate the redox activity and electron transfer pathways of the biofilm.

- **Potential Range:** -0.5 V to +0.6 V vs. Standard Hydrogen Electrode (SHE).
- **Scan Rate:** 0.01 V/s (unless otherwise specified).
- **Data Selection:** At least three cycles were performed for each cell, with only the final scan used for analysis to ensure reproducibility.

Analytical Methods and Physicochemical Characterization

The organic strength and chemical environment of the MFCs were monitored using the following standardized protocols:

- **COD Analysis:** The organic concentration of the influent and effluent was quantified using high-range photometric cell test kits (Product No. 114541; range: 25–1500 mg/L) supplied by Merck, UK. Samples were prepared in reagent vials according to the manufacturer's procedures and determined colorimetrically using a Spectroquant® Pharo 300 spectrophotometer (Merck, UK).
- **pH and Conductivity Measurements:** The pH and electrical conductivity of the anolyte and catholyte were monitored using a calibrated multi-parameter meter to ensure a stable electrochemical environment.Anolyte Stability: The sodium acetate-based anodic medium was maintained at a near-neutral pH (7.0±0.2) to provide an optimal metabolic environment for the electrogenic microbial consortium.

- **Catholyte Conditions:** The 50 mM phosphate basal solution (pH 7.0) was monitored to ensure that proton consumption during the oxygen reduction reaction (ORR) did not result in localized pH shifts.
- **Correlation with Resistance:** Conductivity data was integrated with the EIS analysis to confirm that variations in solution resistance (R_s) were driven by physical connection quality rather than electrolyte fluctuations.

Mathematical Estimation and Mechanistic Correlation of Energy Losses

To quantify and interpret the overpotentials occurring during MFC operation, the polarization behavior was fitted using a semi-empirical model. This model dissects the cell potential (V) as a function of current density (I_D) by accounting for activation, ohmic, and mass-transport losses:

$$V = E_o - b\ log\ log\ I_D\ - RI_D - \gamma e^{\omega I_D} \qquad \textbf{(Equation 1)}$$

where V is the measured cell potential, E_0 is the theoretical open-circuit potential, b is the activation coefficient, R is the ohmic resistance coefficient, I_D is the current density, γ is the diffusion or concentration coefficient, and ω is the current consumption coefficient. The terms in Equation 1 were used to estimate the contribution of activation, ohmic, and concentration-related losses during MFC operation. The fitted parameters were then compared with the EIS and CV results to support the interpretation of the internal resistance effect.

The parameters are defined and correlated with physical characterization tools as follows:

- **V (V):** The final potential output, reflecting the cumulative energy losses in the system.
- **E_o (V):** The theoretical open-circuit potential where no energy loss occurs.
- **b (V) (Activation Coefficient):** Represents the initial potential energy required to activate redox reactions. This coefficient is directly linked to the charge transfer resistance (R_1) found in EIS and the midpoint potential shifts in CV. An increase in b (from 0.0266 V to 0.0415 V) correlates with the higher R_1 values in Groups 2 and 3, signaling a hindered initiation of electron transfer.
- **R (Ω) (Ohmic Coefficient):** Accounts for potential losses during electron and ion transport between electrodes. This parameter correlates with the solution resistance (R_s) and membrane resistance measured in EIS. The modeled R values (e.g., 3.18 Ω for Group 3) quantify the voltage drop caused by the physical poor connections or connection gaps identified in the experimental setup.
- **γ (V) and ω (m²/A) (Diffusion/Concentration Coefficients):** γ explains the energy consumed to transport reactants to the electrode surface, while ω estimates the rate of current consumption per surface area. These are validated by the Warburg element (W) in the EIS equivalent circuit and the linear relationship between peak current and scan rate in CV, which confirms whether the system is diffusion-limited.
- **Mechanistic Insight:** By linking these coefficients, the model suggests that increased internal resistance may not only increase ohmic loss, but may also contribute to activation and apparent mass-transport losses.

Results and discussion

Bioanode Enrichment and Steady-State Performance

The enrichment of electrogenic bioanodes was performed under continuous flow conditions (0.17 mL/min) to maintain a consistent substrate supply during the initial colonization phase.

Following this 50-day period, the operational mode was transitioned to fed-batch, which triggered a significant performance enhancement. As illustrated in Figure 2(a), the current density surged twofold, increasing from 0.15 to a stable plateau of 0.30 A/m^2. This trend aligns with typical microbial growth phases, where an initial logarithmic increase is followed by a steady-state maintenance period (Li et al., 2025; Lim et al., 2020).

The electron recovery was evaluated using Coulombic Efficiency (CE), which was calculated based on the total charge recovered from the current profile and the theoretical charge available from COD removal. The influent COD was approximately 363 mg/L, while the final COD values were 318, 292, and 305 mg/L for MFC Groups 1, 2, and 3, respectively. These values correspond to COD removals of approximately 45, 71, and 58 mg/L. Therefore, the CE result was interpreted together with the COD removal data to avoid overestimating electron recovery from the substrate.

Coulombic efficiency (CE) was calculated based on the ratio between the total charge recovered as current and the theoretical charge available from COD removal, as shown in Equation 2.

$$CE = \frac{M \int I\, dt}{FbV_{an}\Delta COD} \times 100 \qquad \textbf{(Equation 2)}$$

Where M is the molecular weight of oxygen (32 g/mol), I is the current (A), t is time (s), F is Faraday's constant (96,485 C/mol e^-), b is the number of electrons exchanged per mole of oxygen, V_{an} is the anode liquid volume (L), and ΔCOD is the COD removed during the operating period.

The shift to fed-batch operation was pivotal in this performance gain. This mode provides the electrogenic microbes with extended residence time, allowing for the comprehensive utilization of the organic content in the medium. The optimization of bioanode performance is intrinsically linked to the strategic management of operational modes and substrate availability. According to (Lim et al., 2017), providing a stable carbon source and appropriate applied potentials directly enhances microbial metabolism and catalytic activity within the biofilm. This is further supported by evidence that transitioning from continuous flow to fed-batch operation prevents the washout of essential metabolic intermediates, thereby yielding superior peak power densities and coulombic efficiencies. Ultimately, as identified in related studies on microbial electrolysis cells, the robust enrichment of the bioanode remains the primary determinant of total system performance, with mature biofilms capable of sustaining high oxidation rates (approximately 0.36 A/m^2) that mirror the steady-state results achieved in this study (Daud et al., 2018; Elreedy et al., 2024). This "recharge and utilize" cycle inherent in fed-batch operation allows the microbial consortium to maximize electron extraction per mole of substrate as substrate concentration remains constant throughout (Choudhury et al., 2020), thereby reducing mass-transport limitations that can occur in continuous systems with higher internal resistance (Rossi et al., 2021).

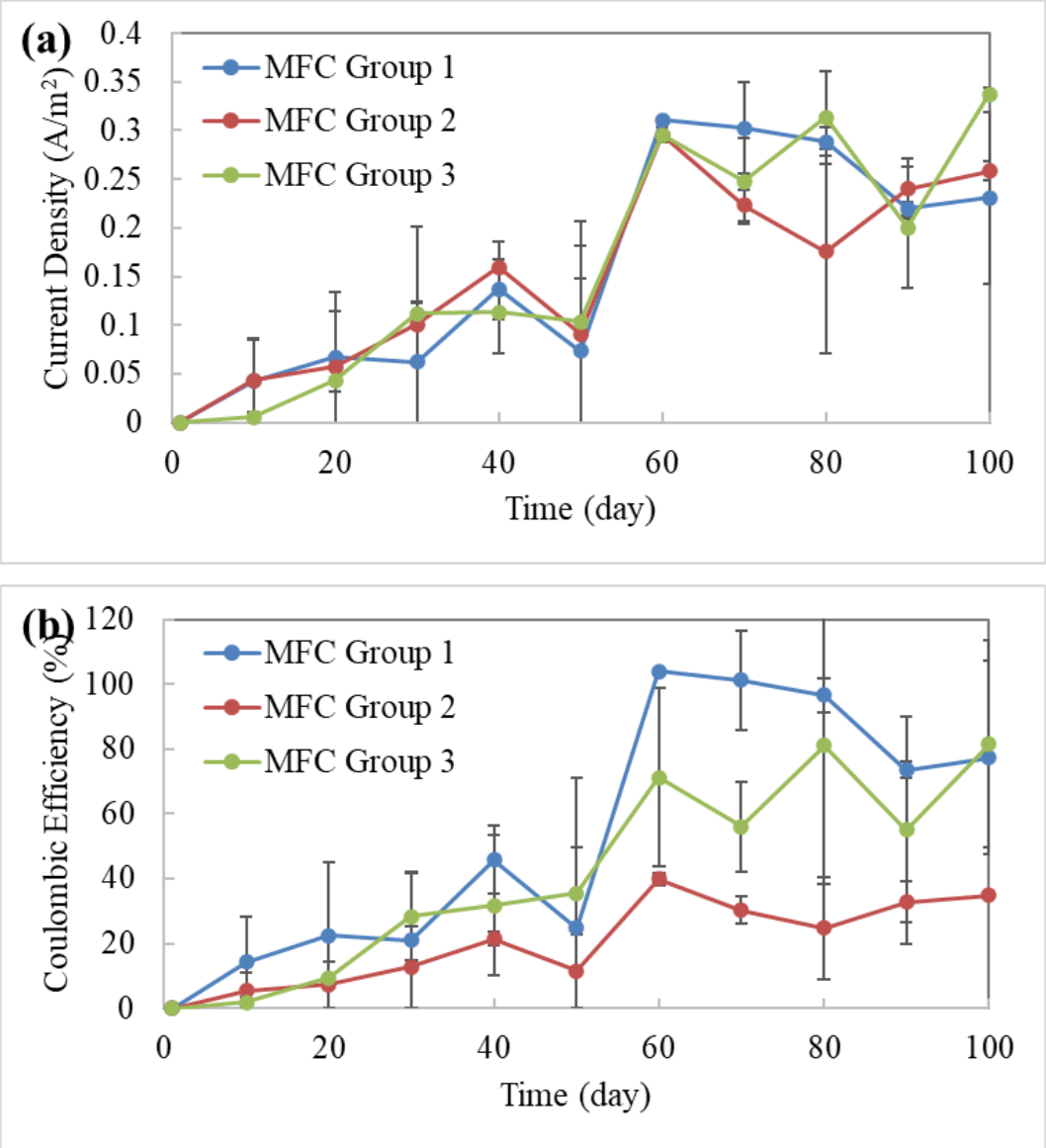

Figure 2 (a) Current density and (b) Coulombic efficiency of tested MFCs with different internal resistance. Data are presented as mean ± standard deviation from duplicate reactors (n = 2). Note that the current density plateaued after day 50.

Impact of Internal Resistance on Electrochemical Polarization

The internal resistance (R_{int}) serves as a critical bottleneck in the scalable power output of microbial fuel cells (MFCs). By deliberately manipulating the physical connectivity of the electrodes, we established a clear correlation between elevated R_{int} and the degradation of electrochemical performance (Chen et al., 2024). This relationship is quantitatively captured in Figure 3(a), where the polarization and power density curves reveal a systematic decline in maximum power output as the resistance gradation moves from Group 1 to Group 3.

The polarization behavior was modeled using Equation 1 to dissect the various energy losses (activation, ohmic, and concentration).

- **Maximum Power Density:** Group 1 achieved a peak power density of approximately 0.09 W/m^{2}at a current density of 0.22 A/m^2. In contrast, the significant connection restriction in

Group 3 limited the peak power to 0.07 W/m^2, representing a ≈ 22 % performance loss associated to the poor connection configuration.

- **Voltage Drop Trends:** As illustrated in Figure 3 (c), the voltage drop was most pronounced in Group 3 (black markers), where the increased ohmic coefficient (R) led to a steeper decline in cell potential compared to the optimized Group 1 (blue markers).
- **External Resistance Correlation:** The calculated external resistances at the peak power points were 414.0 Ω (Group 1), 476.5 Ω (Group 2), and 476.4 Ω (Group 3), indicating that the system's optimal load shifts slightly as internal losses increase.

To identify the specific physical origin of these losses, the charge transfer resistance (R_{ct}) was partitioned into cell components using Electrochemical Impedance Spectroscopy (EIS).

- **Anodic Bottleneck:** The bioanode was identified as the primary site of performance degradation. As seen in Figure 3 (d), the anodic resistance surged from a baseline of 3 ± 1 Ω in Group 1 to a staggering 135 ± 52 Ω in Group 3.
- **Total Cell Resistance:** The overall cell resistance followed the targeted experimental gradation, recording 16 ± 2 Ω for Group 1, 55 ± 8 Ω for Group 2, and 182 ± 6 Ω for Group 3. These values closely mirror the voltage-estimated resistance levels established in the methodology section (20, 60, and 180 Ω).

The data suggest that poor connection increased internal resistance, which then reduced MFC performance. This may be associated with changes in the apparent redox behavior caused by the increase in R_{int}. Recent literature indicates that when internal resistance is high, the biofilm may require higher electrochemical energy for electron transfer to overcome the anodic energy barrier (Ashiq et al., 2025; Miller et al., 2019). This shift is reflected in the positive midpoint potential transition observed in the CV results, moving from -0.2092 V (Group 1) to +0.1594 V (Group 3). This possible bioelectrochemical response may reduce the net potential difference for electricity generation, effectively widening the catalytic band and decreasing overall cell efficiency (Cao et al., 2012; Chadwick et al., 2019).

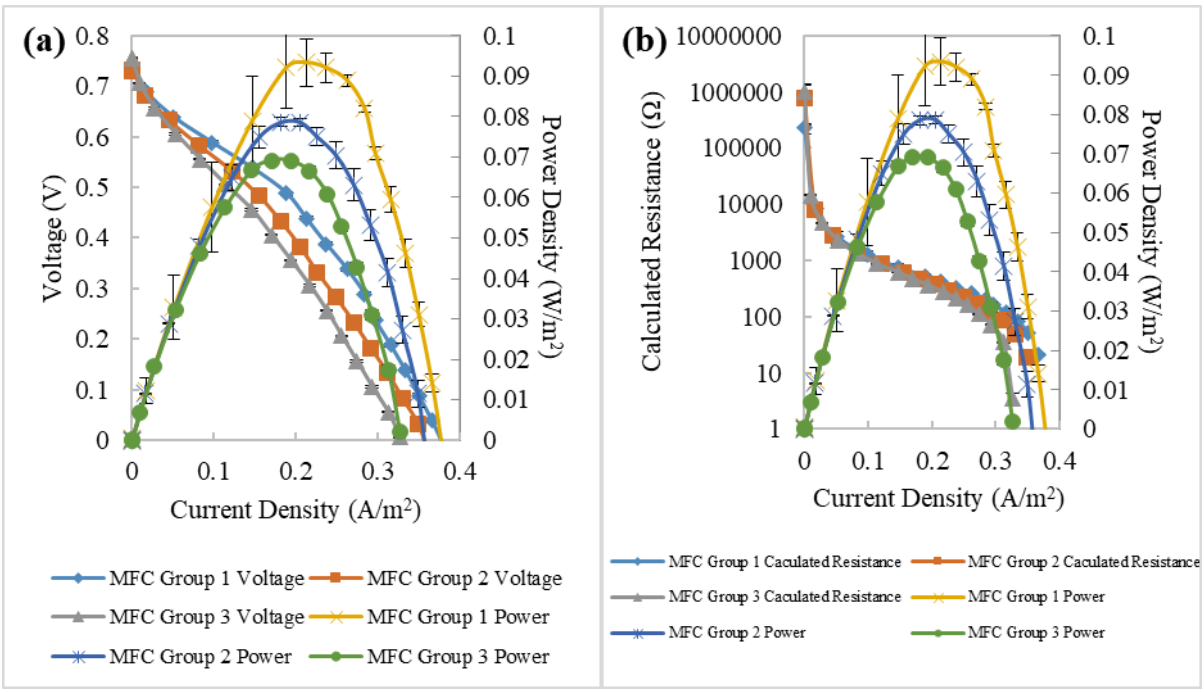

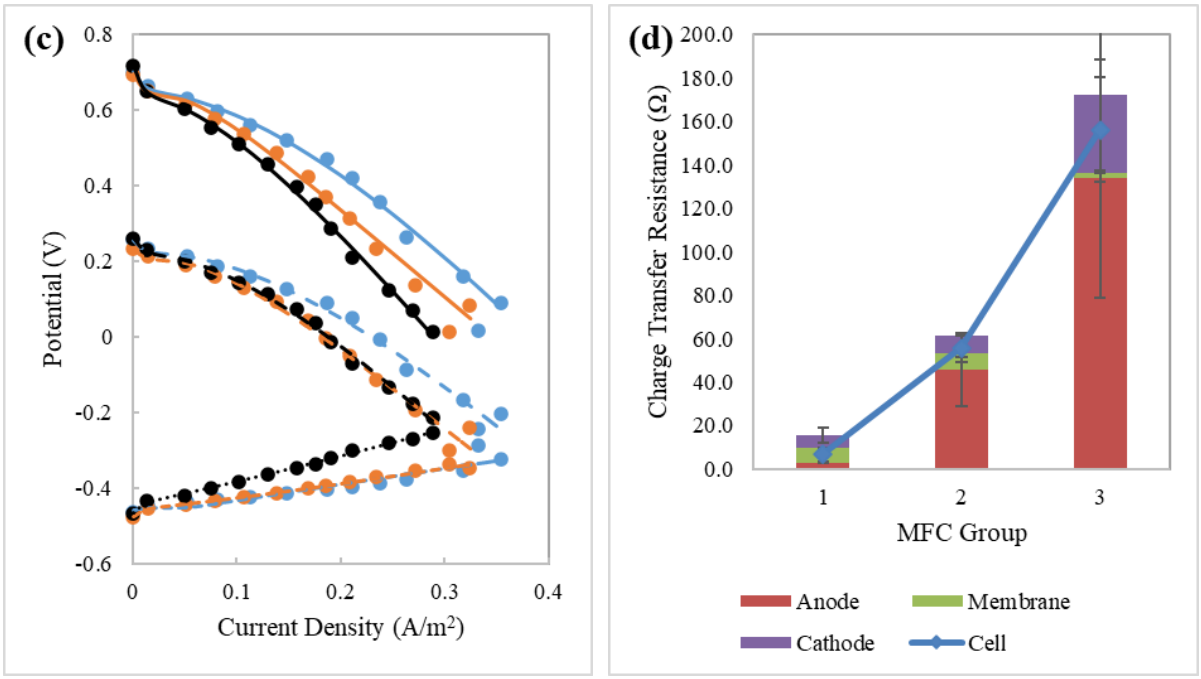

Figure 3 (a) Polarization and power curves, (b) calculated external resistance from a specific current withdrawn, (c) cell and half-cell potential and (d) charge transfer resistance of the MFC with different internal resistances. Data are presented as mean ± standard deviation from duplicate reactors (n = 2).

The empirical coefficients derived from the polarization equation (Table 2) confirm that internal resistance (R_{int}) does not act as an independent variable. Instead, it triggers a synergistic escalation across the three primary overpotential categories, fundamentally altering the cell's efficiency.

- **Ohmic Losses (R):** The ohmic coefficient reached its peak in Group 3 (3.1876 Ω for the cell; 3.4364 Ω for the summed components). This 13% increase relative to Group 1 (3.0875 Ω) is the direct mathematical manifestation of the poor connection design. The disparity between the measured "Cell" R and the "Sum" of components (R_{anode} + $R_{cathode}$) suggests that interfacial contact resistance at the titanium-carbon felt junction contributes significantly to the total voltage drop (iR drop).
- **Activation Losses (b):** A notable trend was observed in the activation coefficient, which rose from 0.0266V (Group 1) to 0.0415V (Group 3) This increase indicates that high R_{int} imposes a greater energy barrier for the initiation of electron transfer (López Zavala & Cámara Gutiérrez, 2023). Mechanistically, poor physical connectivity may require the electrogenic consortium to operate under higher electrochemical energy demand.
- **Mass Transport and Diffusion Losses (γ and ω):** The diffusion coefficient (γ) and the rate of current consumption (1/ω) showed significant variance across groups. In Group 3, the 1/ω value of -0.0988 A/m^2 suggests a more rapid onset of mass transport limitation compared to Group 1 (-0.2026 A/m^2). The fitted diffusion parameters suggest that the higher resistance condition was associated with greater concentration-related losses. However, because direct substrate concentration gradients of ion transport profiles were not measured, the result is interpreted as an apparent mass transport limitation rather than direct evidence of substrate diffusion limitation. This suggests that the higher-resistance condition may be associated with concentration-related losses at lower current densities

(Kanani et al., 2025), although direct ion transport or substrate gradient measurements would be required to confirm the specific mass-transport mechanism.

Table 2 Coefficients calculated from polarization equation (1) based on different internal resistance

Coefficient	Parameter	MFC Group 1	MFC Group 2	MFC Group 3
E_o (V)	Open Circuit Potential	1.2742	0.7623	0.9227
b (V)	Activation	0.0266	0.0372	0.0415
R (Ω)	Ohmic	3.0875	2.2496	3.1876
γ (V)	Diffusion	0.6682	0.2028	0.3553
1/ω (A/m^2)	Consumption Rate	-0.2026	-0.0496	-0.0988

Electrochemical Component Analysis and Resistance Distribution

The internal resistance (R_{int}) of the MFCs was partitioned using Electrochemical Impedance Spectroscopy (EIS) to identify the specific contributors to voltage de-rating. Theoretically, the total cell resistance is the summation of individual ohmic and non-ohmic components:

$$R_{cell} = R_{solution} + R_{anode} + R_{membrane} + R_{cathode} \quad \textbf{(Equation 3)}$$

To further elucidate the electrochemistry at the solid-liquid interfaces and within the bulk solution, each component represented in Equation 3 was decomposed into an equivalent electrical circuit (EEC). This approach allows for the characterization of electronic and ionic behaviors using resistors (R), constant phase elements (Q), and capacitive elements (T).

In this study, the EIS fitting parameters were used to identify the main source of resistance in the MFC. R_s represents the ohmic resistance from the electrolyte, membrane, and solution pathway. R_1 represents the charge transfer resistance, which is related to the electron transfer process at the electrode or biofilm–electrode interface. R_2 represents the interfacial resistance. In this study, R_2 may be related to the contact between the carbon felt and titanium wire, the porous structure of the carbon felt, and the interaction between the biofilm and electrode surface. The T element represents the pseudo-capacitive behavior of the porous biofilm/electrode interface, which is associated with charge storage and relaxation during the electrochemical process. Therefore, these parameters were used to explain how poor physical connection increased the resistance contribution in the MFC system.

As illustrated in Figure 4, distinct EEC models were employed to fit the high-resolution impedance data obtained from the 2-, 3-, and 4-terminal configurations:

- **Whole-Cell and Electrode Interface (Figure 4(a)):** The bioanode and cathode were modeled using an $R_s(R_1Q_1)(R_2Q_2T)$ configuration. Here, the nested RQ elements account for the porous nature of the carbon felt and the charge transfer resistance (R_1) at the biofilm-electrode interface. The inclusion of the T element specifically captures the pseudo-capacitive behavior of the electrogenic biofilm and the interfacial storage of ions (R_2).
- **Membrane and Solution Resistance (Figure 4(b)):** The membrane component was simplified to an $R_s(R_1Q_1)(R_2Q_2)$ circuit. This reflects the predominantly ohmic nature of the CMI-7000 separator (R_s) combined with the limited capacitive behavior (Q) arising from the ionic concentration gradient at the membrane-solution boundary.

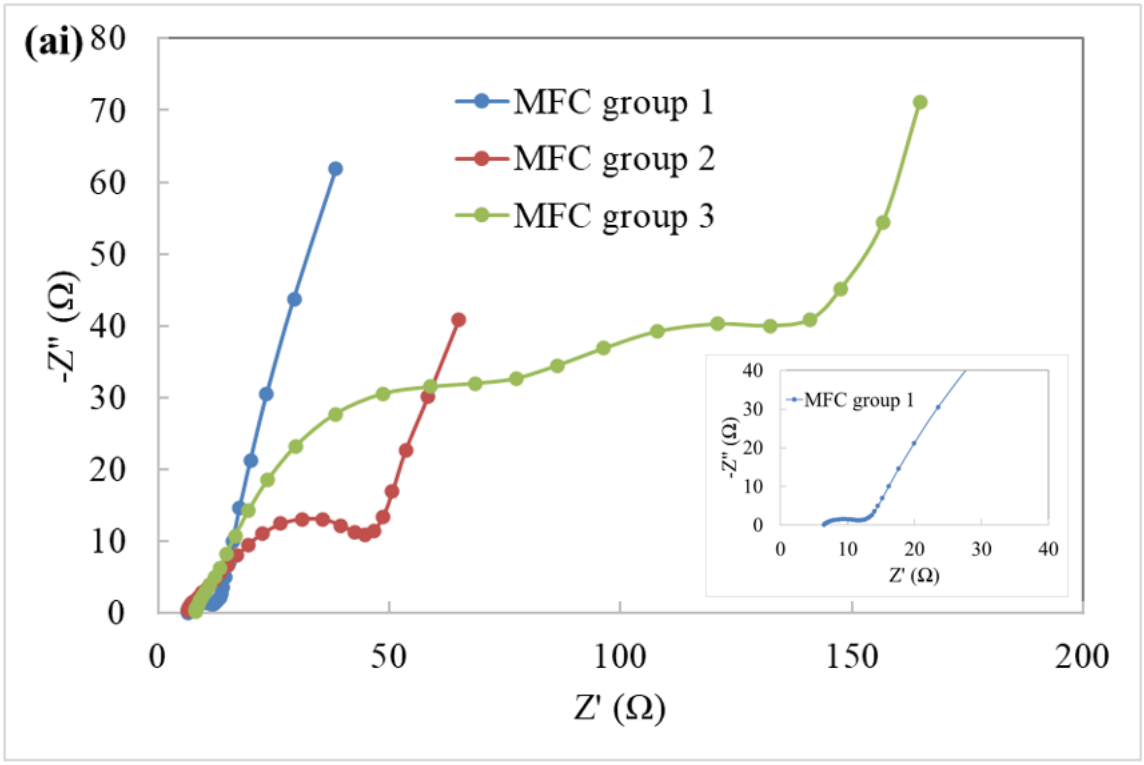
(ai)
MFC group 1
MFC group 2
MFC group 3
-Z'' (Ω)
Z' (Ω)
0
10
20
30
40
50
60
70
80
0
50
100
150
200
MFC group 1
-Z'' (Ω)
Z' (Ω)
0
10
20
30
40

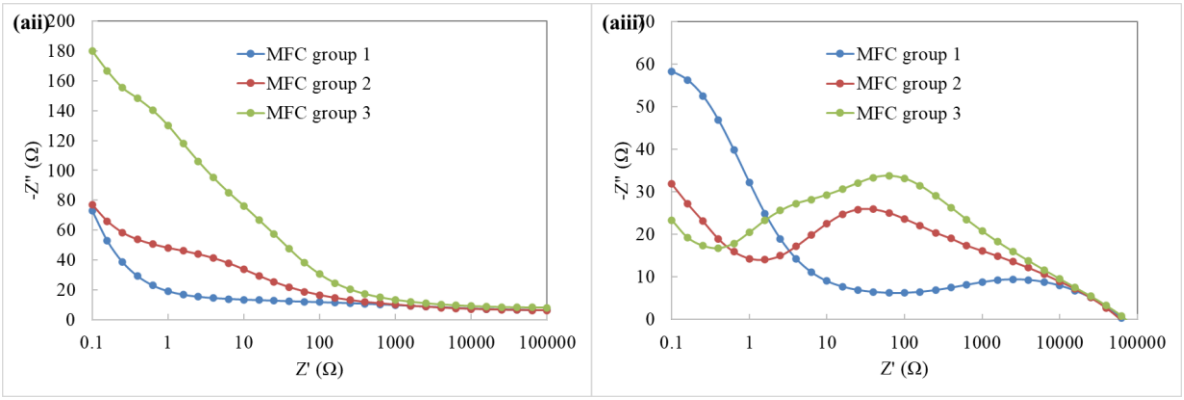
(aii)
MFC group 1
MFC group 2
MFC group 3
-Z'' (Ω)
Z' (Ω)
0.1
1
10
100
1000
10000
100000
(aiii)
MFC group 1
MFC group 2
MFC group 3
-Z'' (Ω)
Z' (Ω)
0.1
1
10
100
1000
10000
100000

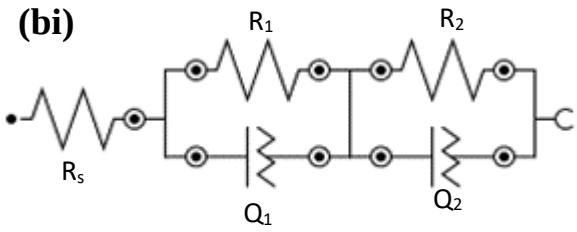
(bi)
R1
R2
Rs
Q1
Q2

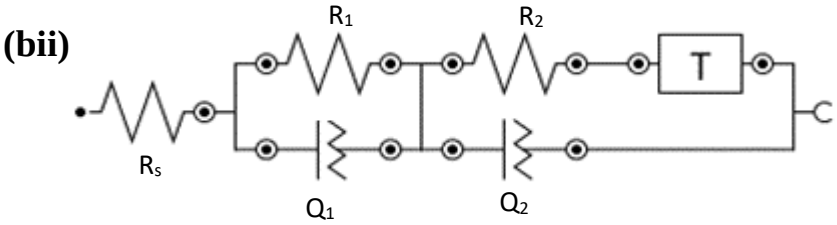
(bii)
R1
R2
T
Rs
Q1
Q2

Figure 4 Electrochemical Impedance Spectroscopy (EIS) Characterization and Equivalent Electrical Circuit (EEC) Models. Sub-panels (a) illustrate the raw impedance spectra: (ai) Nyquist plots showing the distribution of ohmic and polarization arcs across MFC Groups 1–3; (aii) Bode magnitude plots depicting the frequency-dependent impedance response; and (aiii) Bode phase plots identifying the relaxation times of the bioelectrochemical interfaces. Sub-panels (b) present the fitted EEC configurations: (bi) The primary $R_s(R_1Q_1)(R_2Q_2T)$ model used to partition resistances in the whole cell, bioanode, and cathode, where T represents the pseudo-capacitive behavior of the biofilm; and (bii) The simplified $R_s(R_1Q_1)(R_2Q_2)$ model for the membrane component, isolating the ionic transport resistance from the electrode-interface kinetics. Solid lines in the spectra represent the best-fit data, with fit reliability confirmed by χ^2 values ≈ 0.005.

The breakdown of these resistances reveals that any increase in a specific component—most notably the Anode R_2 surge to 140.19 **Ω** in Group 3—directly correlates with the voltage drops observed in the polarization curves. Mechanistically, as R_{cell} increases, the system undergoes significant potential de-rating, which is manifested as a "widening" of the catalytic band in the CV derivatives. This widening signifies that a larger potential window is required to drive microbial electron transfer, effectively lowering the net power generation (Rosman et al., 2026).

By utilizing this multi-terminal EIS approach, the results suggest that the poor-connection condition in Group 3 mainly affected the anodic interfacial zone, transforming a highly conductive biofilm (0.6 **Ω** in Group 1) into the primary kinetic bottleneck of the entire system.

Table 3 Summary of fitted EIS internal resistance components for MFC Groups 1, 2, and 3. Values represent the mean ± fitting error from the data. Parameters were extracted using R(RQ)(RQT) equivalent circuit models.

Element	Parameter	MFC Group 1 (Value ± Error)	MFC Group 2 (Value ± Error)	MFC Group 3 (Value ± Error)
R_s (Ohmic)	R (Ω)	6.286 ± 0.787	5.874 ± 1.198	7.442 ± 0.386
R_1 (Charge Transfer)	R (Ω)	5.475 ± 0.763	17.597 ± 14.562	33.957 ± 22.773
Q_1 (CPE 1)	Y_0 ($mS \cdot s^n$)	0.001 ± 0.000	0.002 ± 0.002	0.002 ± 0.002
	n	0.617 ± 0.057	0.651 ± 0.103	0.698 ± 0.257
R_2 (Interfacial)	R (Ω)	3.936 ± 3.601	31.515 ± 21.807	140.19 ± 28.800
Q_2 (CPE 2)	Y_0 ($mS \cdot s^n$)	0.015 ± 0.002	0.006 ± 0.005	0.001 ± 0.000
	n	0.645 ± 0.064	0.512 ± 0.156	0.639 ± 0.100
T (Capacitive Element)	Y_0 ($mS \cdot s^n$)	0.103 ± 0.077	0.133 ± 0.090	0.152 ± 0.117
	B	0.184 ± 0.155	0.184 ± 0.155	0.342 ± 0.238
χ^2 (Fit Quality)		0.005 ± 0.001	0.019 ± 0.005	0.005 ± 0.001

The data were fitted using the R(RQ)(RQT) equivalent circuit model, where the capacitive element (T) represents the biofilm's ability to store and transfer charge.

- **Capacitance (T) and Surface Roughness (B):** The Y_0 value of the T element increased from 0.103 (Group 1) to 0.152 $mS \cdot s^n$ (Group 3). This suggests that in high-resistance

environments, the biofilm may increase its thickness or surface complexity in a possible change in interfacial charge storage or biofilm/electrode response under high-resistance conditions (Vijay et al., 2023).

- **Fit Quality:** The low chi-squared (χ^2) values (≈ 0.005) across all groups confirm the high reliability of this model in describing the synergistic relationship between ohmic, kinetic, and interfacial energy losses.

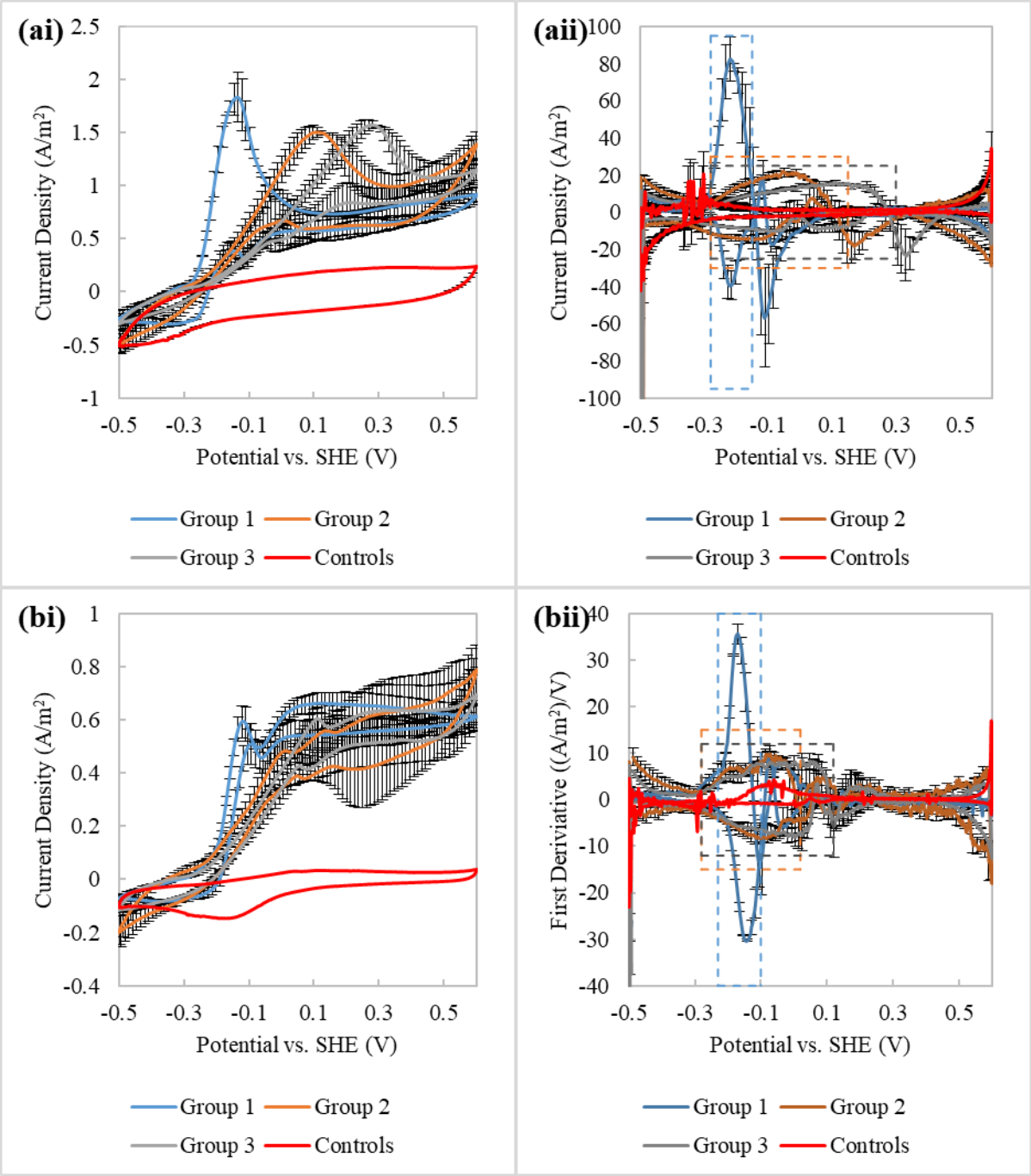

Figure 5 Bioelectrochemical characterization of enriched bioanodes via Cyclic Voltammetry (CV). Profiles were recorded at scan rates of (a) 0.01 V/s and (b) 0.001 V/s. Sub-panels illustrate: (i) the raw cyclic voltammograms highlighting pseudo-reversible redox peaks, and (ii) the first-order derivative (dI/dV) of the

forward scans used to pinpoint the midpoint potential (E_{mid}) and define the catalytic activity band. The widening of these bands across MFC Groups 1–3 suggests increased electrochemical energy demand and apparent overpotential development under higher internal resistance conditions.

Sensitivity Analysis: Effect of medium composition and ionic strength

This section is presented as a supporting sensitivity analysis and is separated from the main controlled internal resistance experiment. While the physical connection integrity remains the primary determinant of bioanode performance, the results in Figure 6 demonstrate that electrolyte composition significantly modulates the output by altering the solution resistance (R_s) and substrate availability. Using the OFAT approach, the impact of Sodium Acetate (NaAc), Ammonium Chloride (NH_4Cl), and Phosphate Buffer Solution (PBS) was evaluated against the baseline configuration (10:5:10 mM).

The most significant surge in current density, reaching a peak of ≈ 2.1 A/m^2 between days 59 and 61, was triggered by increasing the PBS concentration to 50 mM. This behavior is directly linked to a reduction in the internal resistance (Mohyudin et al., 2022) via two mechanisms:

- **Ohmic Reduction:** Higher PBS concentrations increase the ionic conductivity of the electrolyte, effectively lowering the R_s component of the total R_{int} (Guo et al., 2021).
- **Proton Transport:** Enhanced buffering capacity prevents localized pH drops within the bioanode biofilm, facilitating more efficient EET (Cao et al., 2022). Conversely, at low PBS concentrations (1 mM), the current density plummeted to < 0.2 A/m^2, suggesting that even with an optimized electrode connection, a poorly conductive medium can become the dominant limiting factor (Sydow et al., 2017).

The sensitivity to substrate concentration was less pronounced than that of the buffer. Increasing NaAc from 1 mM to 20 mM led to a gradual, incremental rise in current, plateauing around 0.5 A/m^2. This indicates that while the internal resistance dictates the "ceiling" of power output, substrate availability dictates the steady-state maintenance level. Similarly, the addition of NH^{4+} showed a minor positive correlation with performance, likely due to its role as a nitrogen source for biofilm maintenance and its minor contribution to the electrolyte's ionic strength (Ishaq et al., 2025).

These findings indicate that bioanode performance is a multi-variant function. To achieve maximum power density, it is important to address not only the poor physical connection (the physical R_{int}) but also optimize the "chemical R_{int}" (ionic strength). As seen in the sudden current drop when switching from 50 mM back to 10 mM PBS on day 61, a high internal resistance—whether caused by a loose titanium connector or a low-conductivity medium—may substantially reduce the catalytic activity of the biofilm (Gadkari et al., 2020; Guo et al., 2021).

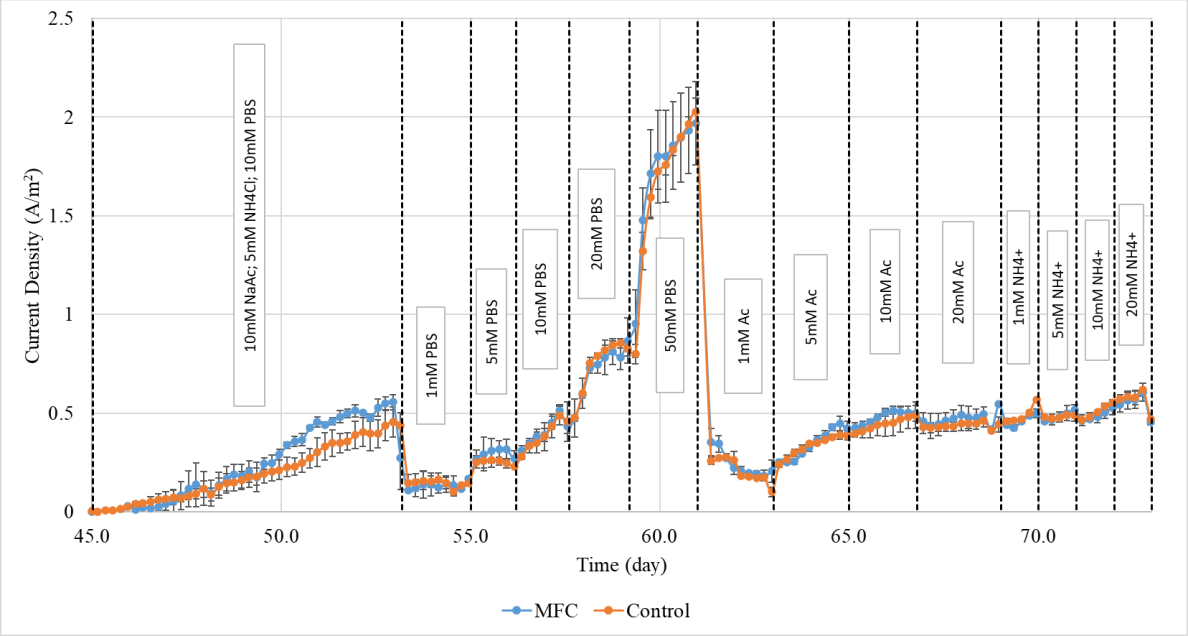

Figure 6 Dynamic Current Density Profile during OFAT Sensitivity Analysis. Continuous monitoring of bioanode current density during the systematic optimization of the anodic medium composition. The profile illustrates the transition from the baseline configuration (10:5:10 mM) to the optimized C:N:PBS ratio (10:5:50 mM). The marked surge to a peak of ≈ 2.1 A/m^2 on day 61 highlights the critical role of increased buffering capacity (50 mM PBS) in mitigating localized pH gradients and reducing solution resistance (R_s), thereby maximizing the electrocatalytic output of the enriched biofilm.

The OFAT sensitivity analysis identifies the 10:5:50 mM (NaAc:NH4Cl:PBS) ratio as the optimized medium composition for maximizing bioanode current density. While substrate and nutrient availability (NaAc and NH_4Cl) are essential for maintaining steady-state metabolic activity, the fivefold increase in buffer concentration (from 10 to 50 mM PBS) was shown to be the most influential chemical factor, driving the current density to a peak of ≈ 2.1 A/m^2. This suggests that in systems where physical internal resistance is already a challenge, maintaining high electrolyte conductivity and superior pH buffering is important to prevent a substantial decrease of the bioelectrochemical interface (Zhang et al., 2019).

Conclusion

This study quantified the effect of physical connection on internal resistance and bioanode performance in microbial fuel cells. By creating different resistance levels through controlled electrode–current collector contact conditions, the results showed that poor physical connection can increase internal resistance and reduce power output. This indicates that connection gaps, although often considered as minor assembly issues, can affect the stability and scalability of MFC performance.

The findings suggest that increased internal resistance does not only contribute to ohmic losses, but may also increase activation and diffusion-related losses. EIS analysis showed that the bioanode interface was the most affected component, with R2 becoming the main contributor to total cell resistance under poor-connection conditions. This highlights that the bioanode interface is highly sensitive to physical contact quality.

CV analysis showed a positive shift in apparent midpoint potential and broadening of the catalytic response at higher resistance. These changes suggest that the bioanode required higher electrochemical energy for electron transfer. However, this should be interpreted carefully because CV alone cannot confirm microbial metabolic adaptation or specific changes in electron-transfer pathways. Further biological analyses, such as microbial community analysis, biofilm imaging, EPS quantification, or mediator analysis, are needed to confirm whether these electrochemical changes are related to specific microbial or biofilm changes.

The OFAT analysis also showed that medium composition and ionic strength affected current generation, with 50 mM PBS improving buffering capacity and electrolyte conductivity. Overall, this study suggests that both physical connection and electrolyte composition should be considered when optimizing MFC performance.

Acknowledgements

The authors would like to express their gratitude to Universiti Kebangsaan Malaysia for supporting this research through the Research University Grant (GUP-2023-004) and Innovation Fund (INOVASI-2024-007). Financial support was also provided by the Malaysian Ministry of Higher Education under the Fundamental Research Grant Scheme (FRGS/1/2024/TK09/UKM/03/1) and the Pahang State Government via the Rompin State Park Forestry Research and Education Grant (RA-2024-003). Additionally, the authors gratefully acknowledge Mohd Asri Yusof, Mohd Fareeq Ahmad Fudzi, and Nik Samila Che Yusoff for their technical expertise and invaluable assistance with reactor fabrication, experimental design, and laboratory operations.

Author Contributions

Nor Syazwanie Mohd Saidi: Conceptualization, Methodology, Investigation, Data Curation, Writing – Original Draft. **Muhammad Farhan Hil Me:** Investigation, Validation, Visualization, Software (EIS Fitting). **Yashawini Phriya Rauichandran:** Investigation, Resources, Writing – Review & Editing. **Ryan Yow Zhong Yeo:** Investigation, Formal Analysis (CV Kinetics), Data Curation. **Mohammad Sherjeel Javed Khan:** Investigation, Validation, Writing – Review & Editing. **Swee Su Lim:** Conceptualization, Supervision, Project Administration, Funding Acquisition, Writing – Review & Editing.

Declaration of Competing Interest

The authors declare that they have no known competing financial interests or personal relationships that could have appeared to influence the work reported in this paper.

References

Ashiq, N. M., Aldarmaki, A. A. J. A. R., Alketbi, M. S. S., Alshehhi, H. A. A., Alkaabi, A. S. O., Alshamsi, N. S. M. S., & Hassan, A. A. (2025). Challenges in Operating a Microbial

Electrolysis Cell (MEC): Translating Biofilm Activity to Electron Flow and Hydrogen. *Sustainability*, *17*, 32. https://doi.org/https://doi.org/10.3390/su172411216

Baba, I. A., Abdulkareem, A. S., & Tijani, J. O. (2026). Photo-Fenton treatment of emerging pollutants in municipal wastewater using nanocatalysts: A sustainable approach. *Results in Chemistry*, *20*, 102999. https://doi.org/https://doi.org/10.1016/j.rechem.2025.102999

Boutarbouch, M., El-Moustaqim, K., Azoulay, K., Boudoudou, D., Abarkan, A., Moufti, A., & Mabrouki, J. (2026). Solar-Powered Electrochemical Processes for Sustainable Wastewater Treatment and Green Hydrogen Production: A Review [10.1051/bioconf/202621504009]. *BIO Web Conf.*, *215*.

Cao, B., Majors, P. D., Ahmed, B., Renslow, R. S., Silvia, C. P., Shi, L., Kjelleberg, S., Fredrickson, J. K., & Beyenal, H. (2012). Biofilm shows spatially stratified metabolic responses to contaminant exposure. *Environmental Microbiology*, *14*(11), 2901–2910. https://doi.org/https://doi.org/10.1111/j.1462-2920.2012.02850.x

Cao, M., Yin, J., Song, T., & Xie, J. (2022). Effects of the presence of phosphate buffer solution on removal efficiency of Pb and Zn in soil by solid phase microbial fuel cells. *Biotechnology Letter*, *44*, 11. https://doi.org/https://doi.org/10.1007/s10529-022-03315-1

Chadwick, G. L., Jiménez Otero, F., Gralnick, J. A., Bond, D. R., & Orphan, V. J. (2019). NanoSIMS imaging reveals metabolic stratification within current-producing biofilms. *Proceedings of the National Academy of Sciences*, *116*(41), 20716–20724. https://doi.org/10.1073/pnas.1912498116

Chen, T., Liu, H., & Li, J. (2024). Research on minimizing the MFC internal resistance via a shared electrode MFC-MEC coupling system [Article]. *Biochemical Engineering Journal*, *203*, Article 109195. https://doi.org/10.1016/j.bej.2023.109195

Choudhury, P., Ray, R. N., Bandyopadhyay, T. K., & Bhunia, B. (2020). Fed batch approach for stable generation of power from dairy wastewater using microbial fuel cell and its kinetic study. *Fuel*, *266*, 117073. https://doi.org/https://doi.org/10.1016/j.fuel.2020.117073

Daud, S. M., Daud, W. R. W., Kim, B. H., Somalu, M. R., Bakar, M. H. A., Muchtar, A., Jahim, J. M., Lim, S. S., & Chang, I. S. (2018). Comparison of performance and ionic concentration gradient of two-chamber microbial fuel cell using ceramic membrane (CM) and cation exchange membrane (CEM) as separators. *Electrochimica Acta*, *259*, 365–376. https://doi.org/https://doi.org/10.1016/j.electacta.2017.10.118

Elreedy, A., Härrer, D., Ali, R., Hille-Reichel, A., & Gescher, J. (2024). Efficacious enrichment of butyrate-oxidizing exoelectrogens upgrades energy recovery in relevant bioelectrochemical systems. *Environmental Technology & Innovation*, *36*, 103871. https://doi.org/https://doi.org/10.1016/j.eti.2024.103871

Environmental Requirements: A Guide For Investors (2010). Department of Environment Ministry of Natural Resources and Environment

Feng, F., Wu, C.-H., Li, F., Wang, X., Zhu, J., Zhang, R., & Chen, S.-C. (2024). Research on the integration of microbial fuel cells with conventional wastewater treatment technology: Advantages of anaerobic fermentation. *Energy Conversion and Management: X*, *23*, 100680. https://doi.org/https://doi.org/10.1016/j.ecmx.2024.100680

Gadkari, S., Fontmorin, J.-M., Yu, E., & Sadhukhan, J. (2020). Influence of temperature and other system parameters on microbial fuel cell performance: Numerical and experimental investigation. *Chemical Engineering Journal*, *388*, 124176. https://doi.org/https://doi.org/10.1016/j.cej.2020.124176

Guo, F., Luo, H., Shi, Z., Wu, Y., & Liu, H. (2021). Substrate salinity: A critical factor regulating the performance of microbial fuel cells, a review. *Science of The Total Environment*, *763*, 143021. https://doi.org/https://doi.org/10.1016/j.scitotenv.2020.143021

Hegazy, G. E., Soliman, N. A., Abdel-Fattah, Y. R., & Taha, T. H. (2025). Enhanced voltage generation in microbial fuel cells (MFCs) using bacterial isolates from seawater and industrial wastewater. *Microbial Cell Factories*, *25*(1), 21. https://doi.org/10.1186/s12934-025-02892-w

Ishaq, A., Said, M. I. M., Azman, S. B., Houmsi, M. R., Isah, A. S., Jagun, Z. T., Mohammad, S. J., Bello, A. A. D., & Abubakar, U. A. (2025). The influence of various chemical oxygen demands on microbial fuel cells performance using leachate as a substrate. *Environmental Science and Pollution Research*, *23*, 16.

Kanani, B., Zahedi, A., Abtahi, F., & Abedi, S. (2025). Exploring operational barriers in microbial fuel cells: Enhancing energy recovery from wastewater. *Electrochemistry Communications*, *180*, 108051. https://doi.org/https://doi.org/10.1016/j.elecom.2025.108051

Kim, B., Chang, I. S., Dinsdale, R. M., & Guwy, A. J. (2021). Accurate measurement of internal resistance in microbial fuel cells by improved scanning electrochemical impedance spectroscopy. *Electrochimica Acta*, *366*, 137388. https://doi.org/https://doi.org/10.1016/j.electacta.2020.137388

Kurniawan, S. B., Roziqin, A., Ahmad, A., Ahmad, M. M., Alfanda, B. D., Pambudi, D. S. A., Said, N. S. M., Abdul, P. M., & Imron, M. F. (2026). Tackling marine pollution in the blue economy: Synergies between wastewater treatment technologies and governmental policies. *Marine Pollution Bulletin*, *222*, 118627. https://doi.org/https://doi.org/10.1016/j.marpolbul.2025.118627

Li, Y., Zong, Y., Feng, C., & Zhao, K. (2025). The Role of Anode Potential in Electromicrobiology. *Microorganisms*, *13*, 23. https://doi.org/https://doi.org/10.3390/microorganisms13030631

Lim, S. S., Fontmorin, J.-M., Izadi, P., Wan Daud, W. R., Scott, K., & Yu, E. H. (2020). Impact of applied cell voltage on the performance of a microbial electrolysis cell fully catalysed by microorganisms. *International Journal of Hydrogen Energy*, *45*(4), 2557–2568. https://doi.org/https://doi.org/10.1016/j.ijhydene.2019.11.142

Lim, S. S., Fontmorin, J.-M., Pham, H. T., Milner, E., Abdul, P. M., Scott, K., Head, I., & Yu, E. H. (2021). Zinc removal and recovery from industrial wastewater with a microbial fuel cell: Experimental investigation and theoretical prediction. *Science of The Total Environment*, *776*, 145934. https://doi.org/https://doi.org/10.1016/j.scitotenv.2021.145934

Lim, S. S., Yu, E. H., Daud, W. R. W., Kim, B. H., & Scott, K. (2017). Bioanode as a limiting factor to biocathode performance in microbial electrolysis cells. *Bioresource Technology*, *238*, 313–324. https://doi.org/https://doi.org/10.1016/j.biortech.2017.03.127

López Zavala, M. Á., & Cámara Gutiérrez, I. C. (2023). Effects of External Resistance, New Electrode Material, and Catholyte Type on the Energy Generation and Performance of Dual-Chamber Microbial Fuel Cells. *Fermentation*, *9*(4), 344.

Mahmoud, R. H., Gomaa, O. M., & Hassan, R. Y. A. (2022). Bio-electrochemical frameworks governing microbial fuel cell performance: technical bottlenecks and proposed solutions [10.1039/D1RA08487A]. *RSC Advances*, *12*(10), 5749–5764. https://doi.org/10.1039/D1RA08487A

Miller, A., Singh, L., Wang, L., & Liu, H. (2019). Linking internal resistance with design and operation decisions in microbial electrolysis cells. *Environment International*, *126*, 611–618. https://doi.org/https://doi.org/10.1016/j.envint.2019.02.056

Mohyudin, S., Farooq, R., Jubeen, F., Rasheed, T., Fatima, M., & Sher, F. (2022). Microbial fuel cells a state-of-the-art technology for wastewater treatment and bioelectricity generation. *Environmental Research*, *204*, 112387. https://doi.org/https://doi.org/10.1016/j.envres.2021.112387

Musa, Y., Wee, B. S., Chung, H. H., Chin, S. F., & Lai, S. H. (2026). Microbial fuel cells as a sustainable nexus of wastewater treatment and bioelectricity generation: Advances, challenges, and future directions in a circular bioeconomy. *Renewable and Sustainable Energy Reviews*, *232*, 116799. https://doi.org/https://doi.org/10.1016/j.rser.2026.116799

Nawaz, A., Hafeez, A., Abbas, S. Z., Haq, I. u., Mukhtar, H., & Rafatullah, M. (2020). A state of the art review on electron transfer mechanisms, characteristics, applications and recent advancements in microbial fuel cells technology. *Green Chemistry Letters and Reviews*, *13*(4), 365–381. https://doi.org/10.1080/17518253.2020.1854871

Nemeș, N. S., Negrea, A., Ciopec, M., Negrea, P., Duţeanu, N., & Duda-Seiman, D. M. (2026). Heavy Metal Ion Removal: A Global Review of Wastewater Treatment Technologies. *International Journal of Molecular Sciences*, *27*(4), 1741.

Rani, M. N. A., Wahab, H. A., & Anuar, H. M. (2025). Toward Climate-Resilient Water Governance: A Legal and Policy Analysis of Malaysia's Water Sector. *International Journal of Environmental Sciences*, *11*.

Ravindran, V. H., Nuramidah, Mohd Arish, N. A., & Awang, M. (2025). Evaluation of Anaerobic and Aerobic Treatment for Tds, Cod, and

Bod Reduction in Meatball Wastewater *International Journal of Research and Innovation in Social Science*, *9*(5). https://doi.org/https://dx.doi.org/10.47772/IJRISS.2025.905000217

Rosman, N., Yusof, N., Norddin, M. N. A. M., Jaafar, J., Salleh, W. N. W., & Sa'adon, S. (2026). Performance evaluation of POME-based microbial fuel cells: treatment efficiency, power generation, and electron loss pathways. *Energy, Ecology and Environment*. https://doi.org/10.1007/s40974-026-00412-z

Rossi, R., Baek, G., Saikaly, P. E., & Logan, B. E. (2021). Continuous Flow Microbial Flow Cell with an Anion Exchange Membrane for Treating Low Conductivity and Poorly Buffered Wastewater. *ACS Sustainable Chemistry & Engineering*, *9*(7), 2946–2954. https://doi.org/10.1021/acssuschemeng.0c09144

Saghir, M., Ayub, A., Nizami, A.-S., Baqar, M., Kamyab, H., Waqas, M., Rehan, M., & Asam, Z.-u.-Z. (2026). Sustainable valorization of leachate at Lakhodair landfill, Lahore: An integrated life cycle environmental and economic assessment of biogas production.

Biomass and Bioenergy, *205*, 108540. https://doi.org/https://doi.org/10.1016/j.biombioe.2025.108540

Solomon, D., Kiflie, Z., & Van, H. S. (2020). Integration of sequencing batch reactor and homo - catalytic advanced oxidation processes for the treatment of textile wastewater. *Nanotechnol Environ Eng*, *6*. https://doi.org/10.1007/s41204-020-0070-6

Sydow, A., Krieg, T., Ulber, R., & Holtmann, D. (2017). Growth medium and electrolyte—How to combine the different requirements on the reaction solution in bioelectrochemical systems using Cupriavidus necator. *Engineering in Life Sciences*, *17*(7), 781–791. https://doi.org/https://doi.org/10.1002/elsc.201600252

Vijay, A., Ghosh, P. C., & Mukherji, S. (2023). Power Generation by Halophilic Bacteria and Assessment of the Effect of Salinity on Performance of a Denitrifying Microbial Fuel Cell. *Energies*, *16*(2), 877.

Wang, A., Klassert, C. J. A., Karutz, R., Smilovic, M., Kahil, T., Burek, P., Zhu, Y., Zozmann, H., Klauer, B., Küblböck, K., Omann, I., Figueroa, A. J., Wada, Y., Naylor, R., & Gorelick, S. M. (2026). Drought-Driven Water Insecurity in an Emerging Indian Megacity: A Coupled Multi-Agent Systems Approach for Policy Evaluation. *Earth's Future*, *14*(3), e2025EF007976. https://doi.org/https://doi.org/10.1029/2025EF007976

Wilk, B. K., Szopińska, M., Sobaszek, M., Pierpaoli, M., Błaszczyk, A., Luczkiewicz, A., & Fudala-Ksiazek, S. (2022). Electrochemical oxidation of landfill leachate using boron-doped diamond anodes: pollution degradation rate, energy efficiency and toxicity assessment. *Environmental Science and Pollution Research*, *29*, 17.

Zadeh, P. G., Rezania, S., Fattahi, M., Dang, P., Vasseghian, Y., & Aminabhavi, T. M. (2024). Recent advances in microbial fuel cell technology for energy generation from wastewater sources. *Process Safety and Environmental Protection*, *189*, 425–439. https://doi.org/https://doi.org/10.1016/j.psep.2024.06.077

Zhang, X., Li, X., Zhaoa, X., & Li, Y. (2019). Factors affecting the efficiency of a bioelectrochemical system: a review. *RSC Advances*, *9*, 14.

Malaysian Journal of Energy and Applications 1 (2026): 24-56
https://doi.org/10.17576/myjea.2026.01.24

SYSTEM ANALYSIS OF CONVENTIONAL DMFC VERSUS MEMBRANE-LESS FUEL CELL: ELECTRODE ARCHITECTURE

Iesti Hajar Hanapi[1]*, Siti Kartom Kamarudin[1,2]*, Norazuwana Shaari[1] & Siti Hasanah Osman[1]
[1] *Fuel Cell Institute, Universiti Kebangsaan Malaysia, 43600 UKM Bangi, Selangor, Malaysia.*
[2] *Department of Chemical Engineering, Universiti Kebangsaan Malaysia, 43600 UKM Bangi, Selangor, Malaysia.*

**Corresponding author: ctie@ukm.edu.my; iestihajar@gmail.com*

Received 19/6/2026; Received in Revised Form 22/6/2026;
Accepted 22/6/2026; Available Online 20/07/2026.

Abstract

Direct methanol fuel cells (DMFC) are increasingly recognized as a promising energy conversion technology, particularly suited for compact and portable power applications, owing to the high energy density and simple fuel management. In traditional DMFC, the fundamental electrochemical unit is the membrane electrode assembly (MEA), which consists of a proton-conducting membrane sandwiched between the anode and cathode electrodes. Alternatively, the development of membrane-less DMFC systems, which employ a co-laminar microfluidic flow to establish a "virtual membrane," eliminates the necessity for a physical membrane while still facilitating proton transport and electrochemical separation. Electrodes continue to be a critical element in both systems, as they regulate the efficacy of methanol oxidation and oxygen reduction reactions, despite the architecture differences. The present review critically evaluates the present state and prospective trajectory of electrode development in both conventional and membrane-less DMFC. Engineering electrodes that provide improved catalytic activity, structural durability, and mass transport characteristics while adhering to a variety of operational constraints is the primary challenges. This paper provides a comparative analysis of the progress and limitations in each system by investigating the fundamental operating principles and reviewing recent innovations in electrode materials, and architectures. The investigation also investigates the operational stability, scalability, and performance trade-offs that are linked to real-world deployment. The review emphasizes the direct relationship between advancements in electrode technology and global sustainability initiatives, as they are consistent with the United Nations Sustainable Development Goals SDG 7 (Affordable and Clean Energy) and SDG 13 (Climate Action).

Keywords: Direct methanol fuel cell (DMFC), Membrane-less fuel cell, Electrode architecture, Microfluidic fuel cell, Laminar flow fuel cell (LFFC)

1.0 Introduction

The increasing global population has intensified global apprehensions regarding the necessity of additional energy in the daily marketplace. Malaysia's economic prosperity is significantly influenced by its production of hydrocarbons and fossil fuels. The Renewable Energy Policy was implemented in Malaysia with the objective of achieving a 9% renewable energy component in the nation's total energy blend by 2020 [1]. Malaysia has the capacity to address environmental concerns on a local, regional, and global scale by implementing renewable energy sources, such as fuel cells. This is appropriate for the nation, as Malaysia is dedicated to the promotion of renewable energy and has reaffirmed its objective of achieving a 20% share of renewable energy in its energy generation by 2025 [2]. The conversion of chemical energy

into electrical power is a cornerstone of modern infrastructure, spanning applications from megawatt-scale utility plants and kilowatt-scale electromobility to watt-scale portable electronics. To facilitate these energy transitions, various electrochemical and mechanical conversion technologies have been engineered, including electric generators, batteries, and fuel cells. Unlike closed-loop storage systems, fuel cells function as open thermodynamic systems characterized by continuous electrochemical oxidation and reduction. By utilizing steady-state reactant streams—typically hydrogen and oxygen—these devices maintain a sustained reaction flow, enabling the efficient and simultaneous generation of electricity and thermal energy [3].

Fuel cells offer significant advantages for portable power applications due to their high energy density, long operational life, simple design, and cost-effectiveness [4]. Currently, proton exchange membrane fuel cells (PEMFC) and direct methanol fuel cells (DMFC) represent two of the most developed types of low-temperature fuel cells [5]. According to a multitude of researchers, DMFC is regarded as a highly prospective and suitable solution for portable devices in order to address the impending energy crisis [6]. This is attributed to their ability to operate at low temperatures, high energy conversion efficiency, and minimal pollutant emissions [7]. Due to its affordability, ubiquitous availability, convenient storage and handling, and renewable nature, the methanol fuel is an appealing option [8].

The MEA is composed of gas diffusion layer (GDL), catalyst layer (CL), and polymer electrolyte membrane (PEM) [9]. Nevertheless, the membrane's presence elevates the likelihood of fuel crossover, which results in catalyst toxicity and an overall decrease in performance due to the reduced active surface area. Furthermore, membrane fabrication presents substantial obstacles due to its high cost and high level of complexity [10]. Consequently, researchers are conducting research on membrane-less fuel cells to resolve these concerns and eliminate the necessity for PEM. Membrane-less or microfluidic fuel cells demonstrate potential for low-power one-chip devices [11], which are suitable for lab-on-a-chip devices with variable power consumption requirements [12]. The membrane-less fuel cell system is capable of recharging secondary batteries. Abrego Martinez [13] conducted a study on the design of a 2-cell stack for devices with minimal power consumption, including LED lighting, blood diagnostics, microanalytical systems, and DNA analysis devices [14,15]. The attainment of a high-power density in microfluidic devices continues to be a substantial obstacle. Electrode research is considered a viable method for improving the efficacy of both conventional systems and membrane-less fuel cells.

Particularly in the electrochemical reactions involving the oxidation and reduction processes is significantly impacted by the electrode modifications. Several authors have investigated critical components of DMFC electrode technology. Zainoodin et al. [16] have disclosed the application of nanotechnology, Ramli et al. [17] have reviewed nanocatalysts and their obstacles, and Ke et al. [18] have investigated the structural and functional properties, applications, preparation methods, and design mechanisms of non-carbon support materials. The temporal evolution of research output in the field of DMFC and membrane-less fuel cells is depicted in Figure 1. The number of publications related to DMFC experienced a significant increase in the early 2000s, and it reached a zenith between 2010 and 2014. Subsequently, there was a gradual decline, but interest in the field persisted until 2024, as illustrated in Figure 1 (a). The growth pattern in Figure 1 (b) is consistent with a more focused trend on electrode development within DMFC, which suggests the critical role of electrode architecture in enhancing fuel cell performance. On the other hand, membrane-less fuel cell research (Figure 1 (c)) began to emerge after 2002, with a consistent increase in publications that reached a climax around 2015. This reflects the increasing interest in low-cost, simplified fuel cell systems that are appropriate for microscale and portable applications. The field is still evolving and has significant potential for innovation, as evidenced by the progressive increase in

membrane-less systems that focused on electrode development (Figure 1 (d)), which peaked more recently around 2020. This analysis of trends underscores the ongoing global research interest in both conventional and membrane-less fuel cell technologies, with a particular emphasis on the crucial role of electrode design and optimization in performance improvement. It further substantiates the relevance and timeliness of a comprehensive review that contrasts and evaluates the electrode architectures of these two fuel cell systems.

Figure 1. Temporal Evolution research of (a) direct methanol fuel cell that (b) focusing on electrode development and (c) membrane-less fuel cell that (d) focusing on electrode development.

Tables 1 and 2 provide a thorough description of recent research on both conventional and membrane-less DMFC. While existing literature frequently isolates catalyst material synthesis or macro-scale microfluidic channel geometries as primary performance drivers, such perspectives often overlook the critical intermediary role of the electrode architecture. The spatial configuration, porosity gradient, and structural topology of the electrode govern the localized multi-phase mass transport (liquid methanol and gaseous CO_2) and charge transfer kinetics that ultimately limit both systems.

The fundamental research gap this review addresses is not merely a lack of comparative literature, but a distinct engineering divergence in how electrode architectures manage internal system inefficiencies:

- In Conventional DMFCs: The electrode architecture (specifically the gas diffusion layer topology and catalyst layer thickness) serves as the primary physical barrier controlling the trade-off between local methanol mass transport and adverse methanol crossover across the polymer electrolyte membrane.
- In Membrane-less DMFCs: In the absence of a physical membrane, system stability relies entirely on laminar flow dynamics. Here, the electrode architecture must be engineered to maintain a stable electrochemical boundary layer, preventing fuel-oxidant mixing without introducing excessive parasitic pressure drops.

Therefore, optimizing the intrinsic activity of a catalyst material or refining bulk microfluidic flows is insufficient if the underlying electrode architecture fails to facilitate efficient multi-phase transport or boundary layer control. This paper provides a targeted, comparative

investigation of these architectural technologies across both traditional and membrane-less DMFCs, guided by three main objectives:

1. To trace the evolution of structural electrode designs—such as 3D porous frameworks, gradient porosities, and integrated gas-evolving topologies—tailored to the distinct mass-transport and crossover demands of both systems.
2. To bridge a critical knowledge gap by establishing the first direct comparative evaluation of how architectural principles from membrane-less configurations (e.g., boundary-layer control) can inform the mitigation of crossover in conventional systems, and vice versa.
3. To align next-generation electrode manufacturing strategies with global sustainability metrics, specifically SDG 7 (Affordable and Clean Energy) and SDG 13 (Climate Action), by emphasizing scalable, low-loading, and binder-free architectural designs.

By shifting the analytical focus from isolated material properties to integrated systemic architectures, this review aims to provide a predictive framework for researchers designing high-efficiency, commercially scalable DMFC technologies.

Table 1. Related review of the electrode for conventional DMFC

Year	Ref.	Summary
2021	[19]	This review critically evaluates the various factors that cause degradation in the MEA of conventional DMFC, which is essential for improving the reliability and efficiency of these fuel cells.
2024	[20]	This paper introduces and experimentally validates a new MEA design with a double-layered catalyst to enhance the performance of micro-DMFC by improving current distribution and reducing fuel crossover.
2022	[21]	This review explores the use of nanostructured conducting polymer-based supports for developing anode materials, highlighting their importance in lowering catalyst usage and supporting the commercial development of DAFC
2018	[22]	This review presents an overview of the methanol electrooxidation process and its underlying mechanisms on Pt and Pt-based catalysts in acidic media, focusing on catalyst size and morphology affect to the electrocatalytic performance.

Table 2: Related review for membrane-less fuel cell

Year	Ref.	Summary
[23]	2024	This paper gives insight into the computational modelling study of membrane-less fuel cell system including governing equation, the configuration of the existing systems, and studies of operational condition.

[24]	2022	This paper focuses on the recent development of paper-based membrane-less fuel cell system that invented in 2014. The fundamental, fabrication method, the geometrical design and its performance also being discussed in this work. Besides, the scale up of the system also being addressed with the future perspective to improve the performance of the system.
[25]	2021	Significant recent research efforts involving the membrane-less fuel cell classification based on reactant, flow configuration, and electrode structure. Additionally, the different types of fuel were detailed discussed in this paper including the stacking development of the system.
[26]	2021	This review article specifically focuses on the microchannel geometry, as well as the architecture and arrangement of electrodes within membrane-less fuel cell system.
[27]	2021	This paper outlines the six categories of flow configurations in membrane-less fuel cell system that reported in 2002 to 2020 that highlight on the factors that affecting the power density by modify the diffusive mixing and depletion zones.
[28]	2019	This work compares various channel shapes (Y-, T-, F-, H-, bridge-, and orthogonal), which strongly affect fuel mixing and power output. It also discusses easy fabrication techniques (CNC micromilling, soft/photolithography, and paper-based methods).
[29]	2018	Focus on the catalyst-selective strategy for the membrane-less fuel cell system.
[30]	2018	These papers addressed the membraned and membrane-less microfluidic microbial fuel cell system and its roadmap of the challenges and the opportunities for the development of this technologies.
[31]	2017	This article provides an analysis of key scientific research on enzyme fuel cells, with a focus on common challenges such as low cell voltage, limited current density, durability concerns, electrode development, device design, and system modelling.

2.0 Fundamentals of DMFC

The conventional and membrane-less DMFC system is the primary focus of this research. Conventional DMFC systems utilize liquid fuel for oxidation at the anode and air or oxygen vapor for the reduction process at the cathode. The electrons traverse an external circuit, while the ions traverse the electrolyte membrane. The conventional DMFC is capable of operating in either an acidic or alkaline environment, contingent upon the specific electrolyte used in the system. Figure 2 (a) and (b) illustrate the reaction that transpires in acidic and alkaline DMFC. The kinetics of alcohol oxidation in acidic conditions are more complex than in alkaline conditions [32].

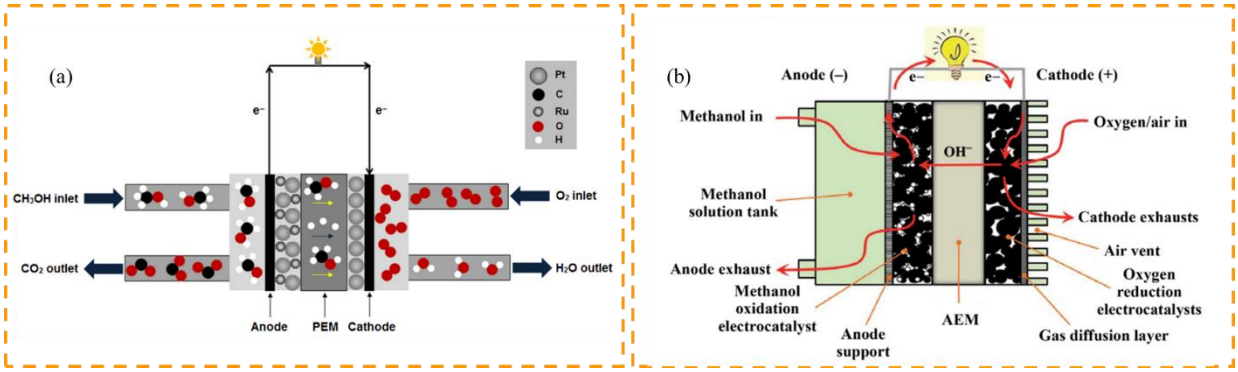

Figure 2. The working principle of (a) acidic [33] and (b) alkaline media DMFC system [34]

Perfluorosulfonic acid is commonly utilized as the electrolyte membrane in DMFC systems operating in acidic environments. In an acidic environment, methanol undergoes electrocatalytic oxidation at the anode, producing protons, electrons, and carbon dioxide as depicted in Figure 2. The protons are conducted to the cathode via the proton exchange membrane (PEM), while the electrons flow through an external circuit to generate electrical power. Oxidation occurs at the anode and reduction of oxygen at the cathode in acidic environments, as indicated by Equations (1) and (2), with Equation (3) representing the overall reaction.

Anode:

$$CH_3OH + H_2O \rightarrow CO_2 + 6H^+ + 6e^- \qquad 0.016\ V \qquad \text{eq. (1)}$$

Cathode:

$$\frac{3}{2}O_2 + 6e^- + 6H^+ \rightarrow 3H_2O \qquad 1.229\ V \qquad \text{eq. (2)}$$

Overall

$$CH_3OH + \frac{3}{2}O_2 \rightarrow CO_2 + 2H_2O \qquad 1.213\ V \qquad \text{eq. (3)}$$

Researchers have investigated a variety of solutions to the primary challenge of fuel crossover in DMFCs, which is the migration of fuel through the membrane. Cai et al. [35] discovered that polymer nano-sieves with narrow apertures effectively prevented methanol crossover at low concentrations. The power density of 132 mW cm^{-2} was achieved by stable phosphotungstic acid (HPW) self-anchored hybrid membranes (PES/PVP-HPW) that were developed by Xu et al. [36]. Additionally, You et al. [37] conducted an investigation into an alternative to Nafion by introducing composite membranes composed of sulfonated polyimide (SPI) and rice husk ash (RHA). These membranes achieved a peak power density of 13.0 mW cm^{-2}.

On the other hand, alkaline DMFC technology uses the same principle as DMFC, but with an alkaline environment and an alkaline anion exchange membrane (AEM) to exchange OH− as can be seen in Figure 2 (b) and Eq. (4) to Eq. (6) [38]. Electrochemical reactions in alkaline media are kinetically favoured over protonic ones due to OH− at the anode that accelerate MOR and carbonate and bicarbonate leaks in the outlet [39]. Furthermore, alkaline environments exhibit lower corrosiveness compared to acidic environments, enabling the

use of non-precious metal catalysts for methanol oxidation reaction (MOR) and oxygen reduction reaction (ORR) with enhanced durability [40]. In addition, the utilization of alkaline electrolytes enhances the longevity of the fuel cell components. Indeed, optimizing alkaline fuel concentrations offers a simpler approach to mitigate issues such as bipolar plate degradation [41], carbon support dissolution [42], and anodic catalyst leaching [43].

DMFC employing anion exchange membranes (AEM) present a promising solution to these limitations. This is due to several factors: firstly, they offer improved electrode kinetics and catalyst stability, enabling the use of more cost-effective non-noble metal catalysts. Secondly, the transport of hydroxide ions in the opposite direction helps reduce crossover. Lastly, AEM-based DMFC exhibit better water management [44,45]. For instance, Sajjad et al. [46] utilized a guanidinium blend AEM, achieving a power density of 2.0 mW cm^{-2} and an OCV of 0.69 V. Similarly, Gupta et al. [47] reported an OCV of 0.6 V and a power density of 7.1 mW cm^{-2} using a MEA based on KOH-doped PVA AEM. Varcoe et al. [48] demonstrated impressive results with a peak power density of 2.8 mW cm^{-2} employing a poly(ethylene-co-tetrafluoroethylene)-based AEM.

Therefore, it can be concluded that the inclusion of KOH in the fuel is essential to boost the power densities. This is because the high concentration of OH^- ions enhances conductivity and efficient electrode reactions. Burhan et al. [49] tested Fumasep® membrane (FAA3-50) in methanol and KOH solutions, achieving 5.2 mW cm^{-2} at 60 ◦C and 33.2 mW cm^{-2} at 80 ◦C peak power density. Besides, Zakaria et al. [50], the QPVA - based membrane can achieve an ionic conductivity of 1.08×10^{-2} S cm^{-1}, yielding a maximum power density of 6.92 mW cm^{-2}. This surpasses the performance of a Nafion - doped KOH membrane, which produces only 5.09 mW cm^{-2}. The author continued the study of relation between the effect of different doped KOH concentrations inside the membranes resulted a power density of 11.28 mW cm^{-2} when exposed to 2 M of KOH [51]. The Table 3 shows the previous studied of DMFC system for acidic and alkaline media.

Anode:

$$CH_3OH + 8OH^- \rightarrow CO_3^{2-} + 6H_2O + 6e^- \qquad \text{-0.810 V} \qquad \text{eq. (4)}$$

Cathode:

$$\frac{3}{2}O_2 + 6e^- + 3H_2O \rightarrow 6OH^- \qquad \text{0.401 V} \qquad \text{eq. (5)}$$

Overall

$$CH_3OH + \frac{3}{2}O_2 + 2OH^- \rightarrow CO_3^{2-} + 3H_2O \qquad \text{1.211 V} \qquad \text{eq. (6)}$$

The electrochemical conversion concept of conventional fuel cells is also applicable to membrane-less, or microfluidic DMFC as presented in Figure 3 (a) and (b). Microfluidics is referring to the investigation fluid flow and transport processes within microscale structures, typically characterized by at least one dimension between 1 and 1000 μm [52,53]. A parallel co-laminar flow is generated when two laminar streams of fluids with comparable viscosity and density travel through a microchannel, which is also referred to as a co-laminar fuel cell (LFFC). The primary distinction is the replacement of the PEM role with a mixing zone that enables the passage of ions across the channel, which is referred to as the "virtual membrane"

or "diffusion zone." The system generates a "virtual membrane" as a result of co-laminar fluxes, which facilitate the transportation of protons. Conversely, the electron is directed across the burden to generate electricity. The Table 4 represent the advantages and disadvantages of the membrane-less fuel cell system.

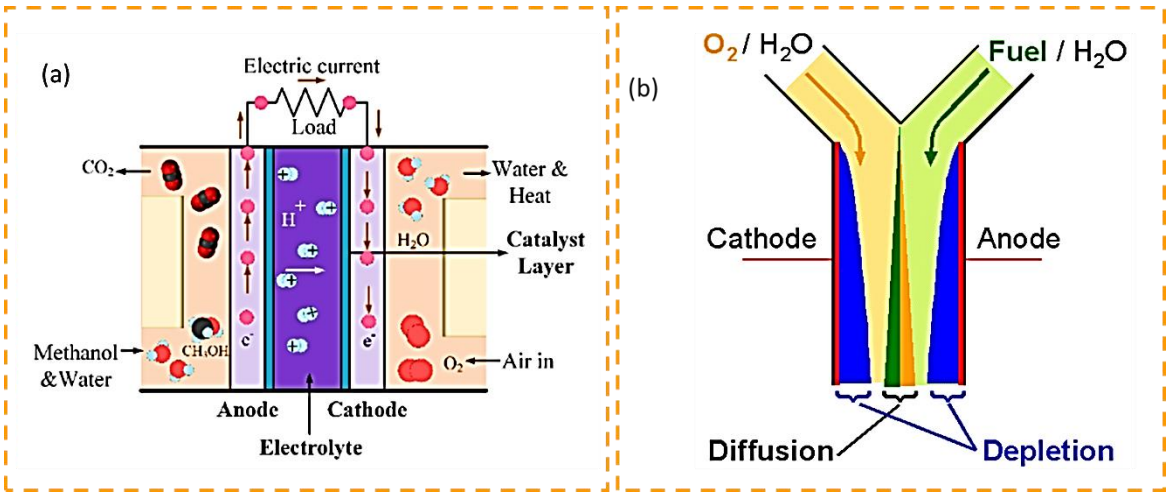

Figure 3. The working principle of the (a) conventional DMFC [54] and (b) membrane-less system [55]

The anolyte and catholyte streams flow along the microchannel after being introduced separately through various inlets. Initially, liquid anolyte and catholyte were introduced into the inlets at specific flowrates to maintain a Reynolds number below value 2100 [56]. Hanapi et al. [57] reported that the Reynolds number for the developed system is approximately to 24. Additionally, as demonstrated in Figure 4, Cohen et al. [58] used a visualising technique to ascertain the laminar flow by means of bathophenanthroline sulphonate (BPS) and $FeCl_2$. The chemicals will form a reddish-cherry solution when there is mixing in the reactants, nevertheless, the channel region at the point of contact did not exhibit any coloration.

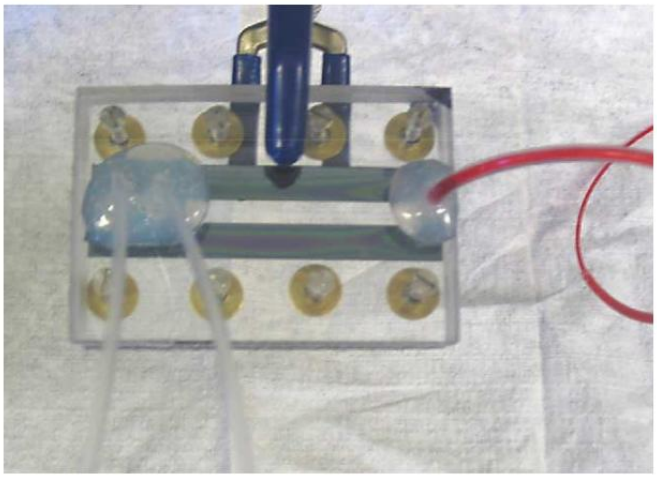

Figure 4. Visual analysis of laminar flow determination for membrane-less fuel cell [58]

Since the membrane-less fuel cell system employs liquid electrolyte, it can be designed to operate with several types of media. For example, an acid medium can be used in the cathode while an alkaline medium can be used in the anode, or vice versa. The use of dual-electrolyte media can enhance the OCV of the system without affecting its operational complexity as

presented in eq. (7) until (12). Choban et al. [59] conducted a study on the media flexibility reported a dual-electrolyte medium, commonly referred to as a mixed medium, attains an OCV up to 1.4 V and a power density of 12.0 mW cm^{-2}. The neutralisation process of OH^- and H^+ occur at the liquid-liquid interface or reactants. Based on the eq. (9) and (12), it is noted that the acidic anode and alkaline cathode media have low theoretical OCV. Most of the energy generated from oxidation reduction is by the process of water ionisation. The interaction of galvanic and methanol electrolytic reactions in this configuration has been identified as the cause of the inability to produce significant amounts of energy [60,61].

Therefore, the use of alkaline anode and acidic cathode widely used by the researcher for better performance. Ponmani et al. [60] conducted a study with dual electrolyte media produced 1.81 V OCV. Hanapi et al. [57] investigated the optimization of mixed reactants and oxidants in membrane-less DMFC, achieving a power density of approximately 30 mW cm^{-2}. Table 5 presents previous research on membrane-less fuel cell systems and their performance. Moreover, Chen and the team [62] conducted a computational fluid dynamics (CFD) analysis discovered that the type of electrodes are important for determining the system's performance. The difference of electrode development studies in the conventional and membrane-less DMFC were discussed in the next section. Additionally, the geometrical design of the membrane-less fuel cell system can be found in different shapes and sizes based on the electrode placement [63]. The electrode architecture for the conventional and membrane-less DMFC will be discussed in the next section.

Mixed-media: acidic anode, alkaline cathode

Anode:

$2CH_3OH + 2H_2O \rightarrow 2CO_2 + 12H^+ + 12e^-$ 0.02 V eq. (7)

Cathode:

$3O_2 + 6H_2O + 12e^- \rightarrow 12OH^-$ 0.04 V eq. (8)

Overall:

$2CH_3OH + 3O_2 + 8H_2O \rightarrow 2CO_2 + 12OH^- + 12H^+$ 0.38 V eq. (9)

Mixed-media: alkaline anode, acidic cathode

Anode:

$2CH_3OH + 12OH^- \rightarrow 2CO_2 + 10H_2O + 12e^-$ -0.81 V eq. (10)

Cathode:

$12H^+ + 3O_2 + 12e^- \rightarrow 6H_2O$ 1.23 V eq. (11)

Overall

$2CH_3OH + 3O_2 + 12OH^- + 12H^+ \rightarrow 2CO_2 + 16H_2O$ 2.04 V eq. (12)

Table 3: Research on conventional DMFC in acidic and alkaline medium

Fuel/oxidant	Electrode/catalyst support	Membrane	T ℃	Max power density	Ref.
3 M methanol	Pt/MC Pt/HiSPEC 3000	Nafion 115	26	24.5 22.1	[64]
1 M methanol + O2	Pt-Ru/50 wt% MWCNT + 50 wt% graphene Pt-Ru/MWCNT	Nafion 117	80	68 40	[65]
1 M methanol + O2	N-doped FWCNT Pt/C	FAA3		0.78 0.72	[66]
1 M methanol + O2	Pt-Ru/Vulcan Pt-Ru/GNF Pt-Ru/FWCNT	Nafion 115	30	3.5 13.1 20	[67]
6 M methanol + Air	Pt-Ru (CNT-MEA) Pt-Ru (CP-MEA)	Nafion		23.2 16.0	[68]
1 M methanol + O2	Pt/MC Pt/Vulcan	Nafion 212	60	58 44	[69]
3 M methanol + air	Pt/C	NA	70	63	[70]
2 M methanol	Pt/C with carbon buffer layer Pt-Ru Pt	Poly(ethylene-co-tetrafluoroethylene)	50	2.8	[48]
2 M methanol + O2	Pt-Ru/CB Pt-Ru/CNF Pt-Ru/CB + CNF	NA	NA	12.6 18.3 13.2	[71]
10 M methanol+	Pt-Ru	Nafion	NA	15	[72]

		Nafion/graphene monolayer			
3 M methanol + 1 M KOH	Pt	guanidinium-chitosan blend poly-mers	NA	2.0	[46]
1 M methanol + O2	Pt/TiC-CDC Pt/Vulcan XC-72R	Nafion 117	80	50.16 42.58	[73]
4 M methanol + Air	NA	Nafion/G-CNTs	25	41.6	[74]
		Nafion/Vulcan XC-72R		30	
2 M methanol + O2	Pt/C	SPEEK/Sfu (0.5 wt%) SPEEK		103 70	[75]
		Nafion 117		50	

Table 4. Advantages and disadvantages of the membrane-less fuel cell system [28]

Advantages	**Disadvantages**
Media flexibility	Generate lower power density
Reduced cost	Higher Ohmic loss than conventional
Size flexibility	Heavy
Simpler water management	Reduced gravimetric power and energy density
Higher energy density due to the uses of liquid fuel compared with gaseous fuel.	

Table 5. Previous research of membrane-less fuel cell system.

Fuel/oxidant	Electrolyte	Design features	Power density		Ref.
HCOOH/dissolved O2	H2SO4	PdCo supported on carbon nanotubes on anode	1.75		[76]
V2+/VO2	H2SO4	Parallel cell connection	16		[77]
HCOOH/dissolved O2	H2SO4	Carbon supported rutherium chalcogenide as cathode catalyst	1.9		[78]
H2/O2	KOH	Alkaline fuel cell	110		[79]
HCOOH/KMnO4	H2SO4	Bridged shaped	26		[80]
V2+/VO2	H2SO4	Plate-frame flow-through stack	5.8		[81]
V2+/VO2	H2SO4	Chip embedded thin film current collector	90		[82]
V2+/VO2	H2SO4	Porous carbon electrode		25	[83]
HCOOH/air	H2SO4	Air breathing with fuel reservoir	29		[84]
Formic acid/KMnO4	H2SO4	CNx nanofibers as cathode catalyst	3.43		[85]
Hydrogen peroxide (0.75 M) + Sodium hydroxide (0.75 M)	H2SO4	grooved electrodes and with general planar electrodes for	2.80		[56]

3.0 Recent Advances in Electrode Architecture

Basically, there are some distinctions for the conventional and membrane-less fuel cell system based on the electrode architecture. In conventional DMFC, the electrode present either; i) the catalyst directly on the membrane or ii) on the substrate. However, for the membrane-less system, the electrode can be in a) flow over, b) flow-through, and c) air-breathing electrodes. The key differences between conventional and membrane-less DMFC in terms of electrode and MEA design are summarized in Table 6. These types of the electrode architecture will be discussed in the following sub-section.

Table 6. Comparative analysis of electrode and MEA development in conventional and membrane-less DMFC

Aspect	Conventional	Membrane-less
MEA type	Nafion-based (CCM, GDE, integral MEAs)	No membrane; electrode-separated by laminar flow
Electrode configuration	Flat catalyst-coated layers on membrane or GDL	Planar, interdigitated, 3D porous, or flow-through
Performance limitation	Methanol crossover, membrane degradation	Fuel mixing, limited residence time, microchannel constraints

3.1 Conventional DMFC electrode system

There are four components of a conventional DMFC: the endplate, current collector, bipolar plate, and MEA. The MEA which comprises CL, MPL, and membrane, is the primary compartment as previously mentioned. The conventional DMFC system is illustrated in Figure 5 (a) in an exploded view. The electrode development which is a component of the MEA will be the primary focus of this topic. In general, there are two fabrication methods for the electrode or MEA in conventional DMFCs: (i) applying the catalyst layer to the GDL and then hot pressing the two catalyst-coated substrates (CCS) onto a pretreated membrane, and (ii) applying the catalyst layer directly to the pretreated membrane and then combining the catalyst-coated membrane (CCM) [86], as illustrated in Figure 5 (a).

The CCS method, which is favoured for its simplicity and potential for mass production presents challenges related to the interfacial contact between the CL and the membrane [87,88]. The CCS-MEA method typically employs a substrate such as carbon paper or carbon cloth [89]. Additionally, the GDL is essential for the dispersion of reactants across the catalyst layer which in turn improves electron collection and catalyst utilization. Additionally, water flooding which can have a detrimental effect on cell performance is effectively prevented by the GDL. Screen printing, rolling, and spraying are widely used methods for fabricating GDL [90,91]. Lee et al. [92] conducted a comparison of spray coating and screen printing using the preparation procedures detailed in Figure 5 (b), to examine the influence of CL deposition methodology on electrode performance. They discovered substantial disparities in the electrochemical performance and morphology of CL between the two methodologies (Figure 5 (c)). A characteristic of the patterned mesh of the screen was the 23 μm thickness and unidirectional fractures of approximately 100 μm of the screen-printed CL. While mesh rugosity can be an issue with poorly formulated screen-printing pastes, it is frequently

rectifiable through optimization, the fractures observed in Lee et al.'s study resulted in increased voltage drops at high current densities as a result of mass transport limitations. This problem was further exacerbated by the excessive incorporation of phosphoric acid (PA) within the fissures, which exacerbated the opposition to oxygen diffusion [100]. Conversely, the spray-coated CL presented a lumpy surface with grains measuring approximately 50 µm in diameter and no discernible fractures, despite its thinner 16 µm structure. The sprayed CL's superior overall performance was a result of its higher porosity which was advantageous in mitigating PA inundation with respect to the screen-printed CL.

In addition, prior research has shown that the optimal performance of the CCS-MEA is achieved when the second layer of the GDL is present, as it functions as a water-resistant barrier. The incorporation of hydrophobic materials and carbon paper support results in the formation of a substantial aperture volume, which facilitates the transportation of reactants and catalysts. The ultimate performance of CCS-based fuel cells is influenced by these factors [93]. Achmad et al. [94] employed the direct paint method to prepare the MEA achieved a peak power density of 25 mW cm^{-2}. In addition, another study conducted by Zainoodin et al. [95] discovered CCS-MEA utilised three different techniques: direct paint (DP), ultrasonic spraying on the diffusion layer (US - D), and ultrasonic spraying directly on the membrane (US - M). The directly spray on the membrane led to the highest performance due to its ability to minimise ohmic resistance, reduce anode potential, and maximise ECSA as can be seen in Figure 6 (b).

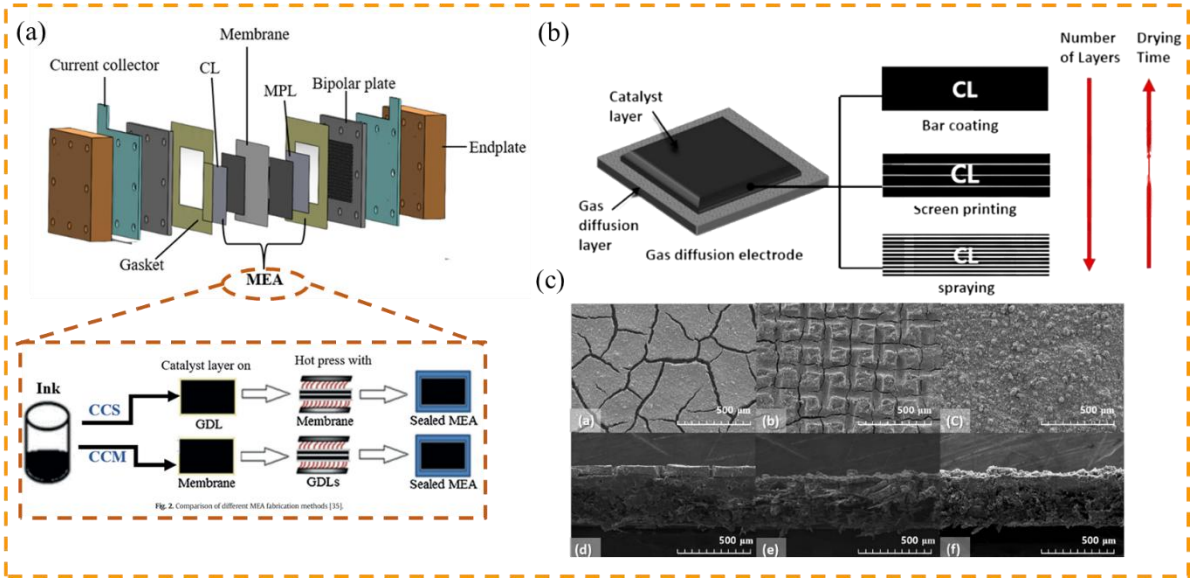

Figure 5. Exploded view of the conventional DMFC with Comparison of different MEA fabrication methods [86], (b))Schematics of the preparation methods for the CL on GDLs by Lee at al.and (c) Top-view and cross sectional SEM images of bar-coated (left), screen-printed (middle), and sprayed CLs (right) [92]

Furthermore, the sputtering procedure has effectively achieved an ultra-low platinum loading for the CCS method, without affecting the cell's performance [96]. The double cathode catalyst layer has been documented as a result of the integration of CCS with the decal method [97]. The inner portion of this layer which is positioned toward the membrane is constructed using the decal method with a Pt loading of 0.3 mg cm^{-2}. The outer portion, which is confronting the gas diffusing layer, is fabricated using the CCS method with a Pt loading of 0.1 mg cm^{-2}. Compared to the MEA generated through the conventional decal method, it resulted in a 13.5% increase in power density.

The other electrode in conventional DMFC is the CCM which have expansion that occurs during the hydration of the membrane can have detrimental effects on the CL in the process of fabricating the CCM [98]. The CCM approach enhanced the contact between the CL and electrolyte membrane resulting in an increase in active sites. This led to a reduction in interfacial resistance and an improvement in the triple phase boundary in the MEA. Shang's team [99] and Su's teams [100,101] both documented the creation of MEA using the CCM technique, by including PA from a pre-doped GDL. It found the CCM-made MEA performed better with low Pt loading than CCS method.

The membrane and catalyst layer facilitate electrochemical reactions, which results in outstanding fuel cell performance and high catalyst utilization efficiency which are advantages of CCM fabrication methods over CCS [102]. Hnat et al. [103] demonstrated that the catalyst burden can be reduced by 75% for CCM-MEA in comparison to CCS-MEA. The CCM-MEA exhibits increased efficiency, power density, and Ohmic and charge transfer resistance. This performance enhancement is primarily attributed to the structural advantages of the CCM-MEA fabrication method, which yields superior catalyst utilization compared to the CCS-MEA configuration at equivalent platinum loadings [104].

The CCM method has several advantages, particularly in terms of performance. However, it also has a drawback that may compromise the long-term performance of the MEA: its brief lifespan. Numerous studies have demonstrated that the MEA fabricated using the CCM method are fragile. It is imperative that additional research be conducted on the CCM fabrication methods to resolve these current issues. Sadeghi et al. [105] investigated the issue of creep behaviour on the CCM, as creep is a form of mechanical degradation that may result in the CCM during fabrication. This factor is important because creep is incontrovertible and is known to diminish the durability of the membrane which in turn deteriorates the system's performance. Nevertheless, researchers have identified solutions to the creep which will inevitably occur and further erode the durability. Therefore, the membrane's durability can be maintained to a certain extent by managing the three primary factors: temperature, relative humidity, and creep stress. Moreover, the catalyst decal method is an enhancement to the CCM approach. For commercial MEA production, the decal method is the most effective, as it involves the coating of catalyst inks on decal substrates, their subsequent curing, and their transfer to a membrane [106]. The decal transfer method was employed by Song et al. [107] to apply thin-film catalyst coatings onto Nafion® membranes in 2005. The resulting power density was more than twice as high as that of the system with conventional MEA. Liu et al. [108] implemented a hybrid approach—direct spraying and a catalyst-coated membrane technique. An efficient CL was effectively generated as a consequence of this innovative approach which involved a heated stereoscopic process.

A lot of research showed that the CCM method outperforms the CCS method. Li et al. [109] used CCS and CCM MEA construction methods for fuel cells and found that CCM performed better. Based on Table 7, CCM-MEA showed lower OCV in all temperatures than the CCS-MEA. Although the CCM-MEA and CCS-MEA used the same electrolyte membrane, spraying catalyst ink onto the membrane surface during preparation could deform the membrane surface due to solvent adsorption, thus increasing crossover. In another study, Rohendi et al. [110] utilized Pt-Co/C by using CCM and CCS method in DMFC and the result can be seen in Figure 6 (c) and (d). These findings are contrary to the other studies as it found that the CCS generated the better performance than CCM.

Table 7. Summary of electrochemical performance (OCV and peak power densities) of CCM-MEA and CCS-MEA with different gas conditions [109].

MEA types	Temperature	Gas condition at anode	OCV/V	Power Density /mW cm-2
CCS-MEA	160	dry	1.000	393
		10% RH	0.994	412
	180	dry	1.02	497
		10% RH	0.992	534
	200	dry	1.020	537
		10% RH	0.997	558
CCM-MEA	160	dry	0.989	500
		10% RH	0.983	526
	180	dry	0.988	598
		10% RH	0.982	613
	200	dry	0.988	614
		10% RH	0.980	617

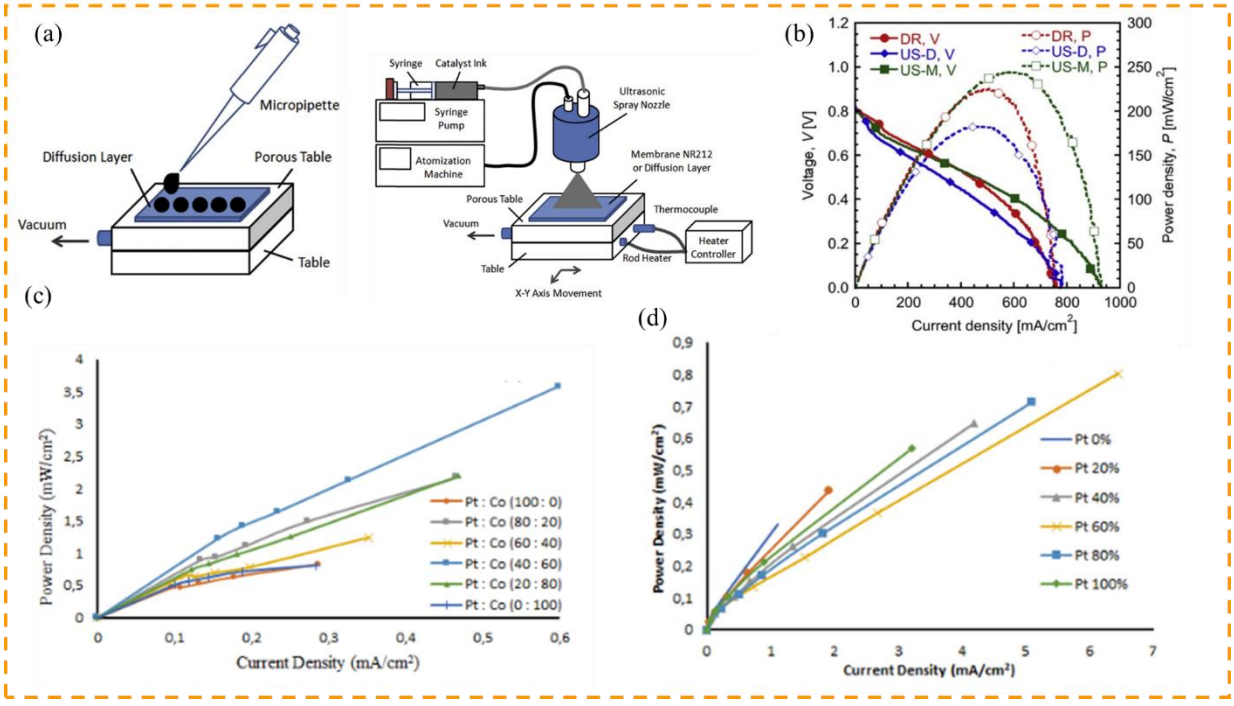

Figure 6. (a) Schematic diagram of the coating techniques of dripping (left) and ultrasonic spraying (right) [95] with (b) Polarization curves of single-cell DFAFCs prepared by the different catalyst layer coating techniques. MEA Performance of electrode with (c) CCS and (d) CCM in DMFC [110]

The conventional electrodes (CCS/CCM) are constructed of Pt/C and ionomer combined in an ink slurry and coated on a membrane or GDL [111]. This process, which starts from the top and moves downwards, generates a randomised structure of electrodes. This structure consists of complex networks of ionomer and pores that hinder the movement of mass and reduce the efficiency of the catalyst [112,113]. Hence, in a recent study by Lee et al. [114] presented the groove electrode, a different type of electrode that offers enhanced performance throughout a broad range of humidity levels with particularly better durability. The process involved creating grooved electrodes by applying a combination of Pt/C and ionomer onto a patterned Si template and then transferring them onto a Nafion membrane.

The CCS and CCM methods employed in MEA fabrication possess significant advantages and disadvantages, as indicated by the preceding discussion. Nevertheless, the primary disadvantage of the CCS fabrication method is the necessity of high Pt loadings to obtain a performance that is comparable to that of the CCM fabrication method. Due to its potential and marketability at low production costs, these factors have persuaded a significant number of researchers to conduct additional research on the CCM fabrication method. Nevertheless, the durability of the MEA is a concern with the CCM fabrication method, rendering the CCS fabrication method the sole viable alternative. The CCS is more challenging to manufacture than the CCM due to the complex technique that necessitates the management of multiple layers of catalysts. Furthermore, membrane wrinkling are not a concern during the CCM fabrication process. Therefore, the CCM fabrication method has the potential to become the primary method for preparing MEA in the future and has undergone numerous enhancements.

3.2 Membrane-less electrode system

The geometric design of membrane-less fuel cell systems is influenced by the varieties and positioning of electrodes, which can be classified as flow-over, flow-through, and air-breathing electrodes [115]. A variety of materials and processing variables must be taken into account when constructing a fuel cell. These include the selection of the carrier substrate for channel formation and the desired geometry, the determination of the catalyst structure and deposition method on the supporting substrate, and the selection of the assembly method for electrodes and channels to facilitate the creation of a liquid-tight sealed cell with interfaces for instrumentation and fuel/oxidant delivery systems.

3.2.1 Flow-over electrode

The flow-over electrodes can be categorized as side-by-side streaming and vertically-layered streaming as portrayed in Figure 7. Ferrigno et al. [116], utilized Y-shaped channel with side-by-side streaming configuration. The monolithic cell design, which integrates microchannels and electrodes within a single layer shows promise for incorporation into on-chip systems [117]. Monolithic design is an appealing approach for this type of system where both electrodes are created on a single substrate [118]. For side-by-side streaming, the vertical fuel-oxidant interface may undergo gravity-induced reorientation, leading to the failure of membrane-less system functioning. The side-by-side streaming have been widely studied for Y- and T-shaped

microchannels [57,80,119]. Whereas the vertically-layered streaming technique employs a multi-layer sandwich construction with electrodes positioned on the sides of the channel. This entire structure is then sealed between two more plates. Moreover, flow-over designs usually entail the continuous flow of anolyte and catholyte over flat electrodes. Due to insufficient convective mass transport, a depletion layer develops over each electrode, resulting in a low reactant concentration. Da Mota et al. [120] attained a power density of 270 mW cm^{-2} using thin film Pt electrodes in a flow-over configuration. Notably, the integration of a staggered herringbone mixer to produce chaotic flow was the sole means to overcome mass transfer restrictions and achieve such a high-power density. Liu et al. [121] proposed a herringbone-shaped electrode in three dimensions with 29.9 mW cm^{-2} power output.

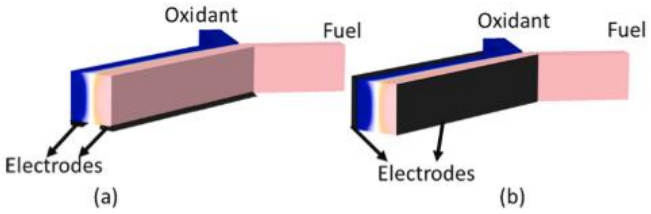

Figure 7. Flow-over electrode with (a) side-by-side streaming and (b) vertically-layered streaming. [26]

3.2.2 Flow-through electrode

In a flow-through configuration, reactant streams pass through a 3D porous electrode housing the catalytically active region. Mass transfer via diffusion/convection across these 3D electrodes replenishes the depletion layer, enhancing fuel utilization and power output. Kjeang et al. [122] demonstrated the porous electrodes can ensure the co-laminar flow phenomenon which significantly enhanced retention time for mass transfer and fuel utilization. Salloum et al. [123] conducted a study on a counter-flow and a sequential radial-flow system using porous flow-through electrodes. Recent studies have shown that the multi-layer construction approach is a powerful strategy for integrating porous flow-through electrodes, enabling enhanced structural control and performance. Krishnamurthy et al. [124] constructed a mathematical model that incorporates porous electrodes with flow-through capability resulted the power densities up to 193 mW cm^{-2}. Lee and Kjeang [82] employed a thin film current collector integrated into a chip and discovered that by optimizing the current collector design to reduce contact resistance, they could achieve a peak power density of 93 mW cm^{-2}. Li et al. [125] examined a vertically-layered that uses vanadium as fuel and has flow-through porous electrodes. In addition, Li et al. [126] examined a radial system with the similar electrode to overcome the size restrictions owing to longer active channel lengths [127]. With this configuration, the electrode size had little effect on the mixing region allowing the radial system to function at larger flow rates while keeping fuel utilisation. Wang et al. [128] conducted a computational and experimental investigation on a flow-through type, examining the behaviour of reactant species in co-laminar and counter-laminar flow configurations. The researchers discovered that the counter-laminar system displayed an uneven distribution of electric current and performed less effectively when compared to the co-laminar flow system. Salloum et al. [129] proposed a convective flow system incorporating porous disk electrodes, as illustrated in Figure 8. This configuration achieved an average OCV of 1.2 V, with peak current and power densities reaching 5.35 mA cm^{-2} and 2.8 mW cm^{-2}, respectively.

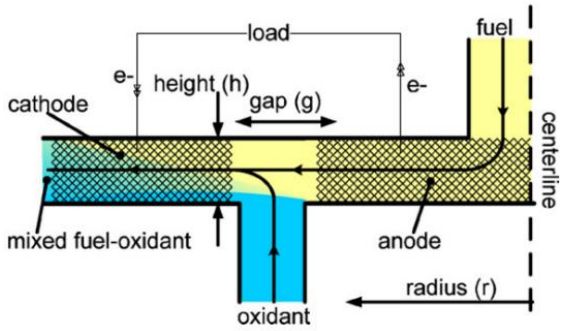

Figure 8. Flow over electrode [129]

3.2.3 Air-breathing electrode

Achieving moderate to high current density is only possible by using oxidants with greater solubility. Oxygen is an excellent choice as an oxidant due to its abundant availability in the environment. Nevertheless, it is low diffusivity that can constrain the mass transfer at cathode. Additionally, the oxygen concentration at a lower range of 2 - 4 mM is insufficient to generate a strong enough force to replenish the depleted region at the cathode [130]. Another conceptual with more inlets for boundary layer replenishment or fluids with a higher oxygen concentration may solve this limitation [131]. Therefore, this issue can be overcome by incorporating the open-air cathode system as shown in Figure 9. This allows for direct supply of oxygen from the air. This architecture is also utilised in conventional DMFC which are commonly referred to as open-air or air-breathing systems. The use of air-breathing electrodes effectively resolves many limitations in reactant mass transfer encountered when utilizing dissolved oxygen or other oxidants. Xuan et al. [132] examined the parameters that restrict the performance of air-breathing electrode system and explored if there is an adequate supply of oxygen from the surrounding air.

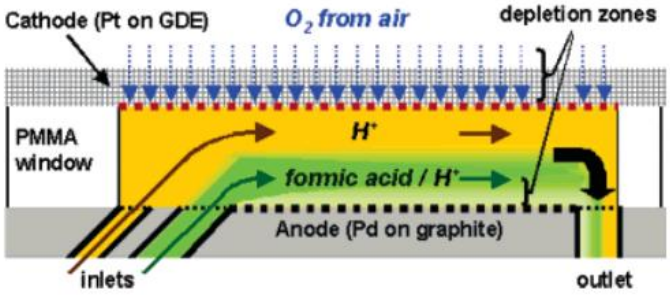

Figure 9. Air-breathing electrode [131]

Researchers have investigated novel electrode designs and methodologies to enhance the efficacy of DMFCs. A cylindrical anode system was introduced by Zhu et al. [133] through the use of a novel catalyst synthesis method. The authors emphasize that cylindrical anodes facilitate the scaling of fuel cell net power output. Furthermore, they examined the efficiency of cells and the properties of mass transfer in both acidic [133] and alkaline [134] electrolytes. Huizhi et al. [135] focused on modelling an air cathode and demonstrated that carefully regulating the electrolyte's hydrodynamic behavior can significantly lower internal transfer resistance.

The air-breathing system with an annular film [136] incorporates the principle of gas film cooling among numerous electrode combinations. A flow-over planar anode air-breathing system has been proposed to resolve the fuel transport limitation caused by the concentration boundary layer above the anode. To actively improve the depleted fuel region, Zhou et al. [137]

recommended the use of a fuel micro-jet. The comparison results indicated that the performance of an immersed fuel micro-jet was 40.9% better than that of the flow-over mode, resulting in an ideal power density of 119.3 mW cm^{-3}. It is imperative to employ standard-condition apparatus with comparable fuel/oxidant, flow rate, concentration, and other operating parameters in order to guarantee a fair comparison of power densities among various electrode types in membrane-less fuel cell systems. The impact of various electrode architectures on power density reported in the literature to date is illustrated in Figure 10, as provided by Tanveer et al. [26]. Table 8 shows the electrode configuration performance of membrane-less fuel cell from literature reviews.

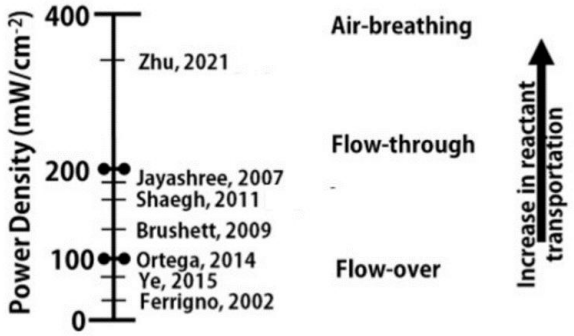

Figure 10. Comparative power density performance of different flow field architectures. [26]

Table 8. Electrode Architectures in Membrane-less Fuel Cells from literature reviews

Year	Ref	Electrode configuration	Study highlight	Results
2005	Choban et el. [59]	Flow-over	First demonstration of membraneless DMFC using co-laminar flow	Achieved power density ~45 μW cm^{-2} with graphite electrodes.
2008	Kjeang et al. [122]	Flow-through	Introduced porous electrodes with better mass transport.	3–4x power increase compared to flow-over; higher fuel utilization.
2015	Shyu et al. [138]	Air-breathing	Simplified design with passive air cathode.	Max power density of 1.23 mW cm^{-2} using methanol.
2020	Ortiz-Ortega [139]	Flow-through	The development of porous electrodes with a tunable Zn electrodeposit	Demonstrated a membraneless microfluidic Zn–air cell with flow-through electrodes, achieving high power densities.
2021	Tanveer et al. [140]	Flow-through	Proposed a membraneless microfluidic fuel cell with hollow flow channels and	Among the evaluated geometries, the hollow structure delivered the superior peak power density—exceeding that of the H-shaped, bridge-shaped, and rectangular

			porous flow-through electrodes.	channels by 6%, 18%, and a remarkable 82%, respectively.
2021	Ibáñez et al. [141]	Flow-over	Investigated diffusion and crossover issues.	Reduced cross-contamination through optimal flow control.
2023	Li et al. [142]	Flow-through	Used trapezoidal electrodes for counter-flow design.	The enhanced performance of the trapezoidal electrode is mainly due to the combined effect of a larger active surface area, lower ionic resistance, and improved fluid distribution.
2024	Liu et al. [143]	Air-breathing	Direct ammonia microfluidic cell with air cathode.	A peak power density of 8.43 mW cm^{-2} and a limiting current density of 78.58 mA cm^{-2} were achieved, exceeding the performance of most low-temperature ammonia fuel cells reported to date.

4.0 Challenges and opportunity

The path toward commercializing both conventional and membrane-less Direct Methanol Fuel Cells (DMFCs) is bottlenecked by distinct transport and manufacturing challenges that are fundamentally dictated by electrode architecture. For instance, while China successfully deployed a DMFC-powered logistics vehicle in 2019 [144], transitioning these systems to high-power applications remains economically and structurally challenging due to high noble metal dependencies and complex mass transport interfaces. In conventional CCS configurations, where the catalyst is deposited directly onto the GDL, non-uniform interfacial contact often necessitates excessively high noble metal loadings, typically exceeding 3 mg cm^{-2} or even 5 mg cm^{-2} Pt to compensate for poor catalyst utilization. Transitioning to a CCM architecture alters this paradigm by spraying the catalyst directly onto the polymer membrane which shortens proton transport pathways and enhances the triple-phase boundary. However, CCM architectures introduce severe mechanical and rheological challenges during fabrication. The localized swelling of the polymer membrane upon contact with liquid-ink solvents often leads to micro-cracking and delamination of the catalyst layer under subsequent thermal consolidation. To mitigate these structural defects, future research must shift from isolated fabrication techniques to integrated hybrid manufacturing strategies. Specifically, combining aspects of CCS and CCM, such as utilizing a dual-stage process that couples automated direct-spray deposition with automated decal transfer can optimize the gradient porosity of the electrode interface. This structural flexibility allows the electrode to adapt to dynamic volume changes under operation, unlocking superior mass-transport kinetics without compromising interfacial adhesion or requiring prohibitive Pt loadings.

Conversely, membrane-less fuel cell architectures completely eliminate the polymer membrane, shifting the primary technical bottleneck from material degradation to strict fluidic

boundary-layer management. Because these systems rely on a "virtual membrane" formed by co-laminar fluid dynamics, the electrode architecture serves as the direct physical determinant of both fluid stability and reactant utilization. Standard planar electrode architectures in microfluidic channels face severe trade-offs: increasing fluid velocities to minimize reactant crossover induces massive parasitic pressure drops across the stack, whereas slowing the flow causes rapid fuel depletion and boundary-layer breakdown. To overcome this, recent research has leveraged advanced microfabrication to transition toward 3D porous frameworks and flow-through architectures. While these high-surface-area topologies exponentially accelerate electrochemical kinetics, they cause critical architectural failure modes which intricate 3D porous electrodes can disrupt the laminar shear plane if the local permeability is non-uniform, causing premature fuel-oxidant mixing and catastrophic voltage loss. Besides, gaseous carbon dioxide bubbles generated at the anode tend to become pinned within highly tortuous porous networks. Without optimized gradient microchannel geometries, this gas entrapment blinds the reactive catalyst sites causing localized mass-transport starvation and electrolyte leakage. Consequently, unlocking the commercial scalability of membrane-less configurations requires a co-design approach where the internal porosity, pore tortuosity, and surface wettability of the 3D electrode architecture are systematically matched to the microchannel flow vectors to maintain laminar stability under dynamic load changes.

5.0 Industry and commercialization

The structural evolution of electrode architectures in both conventional and membrane-less DMFC directly dictates their viability for large-scale industrial deployment. Transitioning these systems from a laboratory setting to commercial market penetration requires shifting the analytical focus from isolated electrochemical performance metrics to systemic economic parameters, manufacturing scalability, and application-specific operating envelopes. The stark differences in the physical footprint and operational mechanics of conventional and membrane-less DMFC naturally divide their commercial trajectories into distinct market segments. Due to their robust structural containment and high volumetric power densities, conventional DMFCs are primary candidates for portable military power packs, auxiliary power units (APUs), and niche industrial logistics vehicles (e.g., forklifts and automated guided vehicles) [145,146]. For these applications, the industry requires electrode architectures that can withstand mechanical shock, vibration, and thousands of hours of start-stop cycling. Meanwhile, in membrane-less fuel cell system, the complete elimination of the physical membrane allows for extreme planar miniaturization and cost reduction. Consequently, membrane-less DMFC architectures are uniquely positioned to power micro-electromechanical systems (MEMS), remote environmental sensors, and single-use point-of-care diagnostic devices [146]. In these sub-watt applications, the primary commercial requirement is not extreme longevity, but shelf-life stability and low-cost fabrication.

For conventional configurations, scaling up CCM production requires replacing manual spraying with continuous roll-to-roll (R2R) slot-die coating. However, the industry faces an ongoing challenge: the mechanical stresses during R2R drying often induce micro-cracks in electrode architectures that feature high catalyst loadings. To achieve commercial continuity, future designs must integrate low-boiling-point solvents and binder-free, self-supporting 3D catalyst networks to ensure structural integrity during high-speed manufacturing. For membrane-less stacks, the core commercial bottleneck shifts from noble metal reduction to hydrodynamic scalability. While a single microfluidic channel operates reliably under strict laminar flow, scaling up to multi-cell industrial stacks requires distributing liquid fuel equally across hundreds of parallel microchannels. Minor variations in local electrode thickness or pore size distribution alter local hydraulic resistance, causing flow maldistribution, boundary-layer

breakdown, and severe fuel crossover. Therefore, commercialization is contingent upon developing high-precision injection molding or laser-ablation manufacturing methods capable of maintaining sub-micron tolerances across mass-produced electrode-channel assemblies [147].

Ultimately, industrial adoption must align with global sustainability initiatives, specifically UN Sustainable Development Goals for Affordable and Clean Energy (SDG 7) and Climate Action (SDG 13). Reaching this threshold requires an aggressive material transition toward earth-abundant, non-noble metal catalysts (such as transition metal oxides or nitrogen-doped carbon frameworks) embedded within recycled carbon-fiber substrate architectures [148]. Furthermore, an emerging commercial horizon involves exploring hybrid architectures that bridge the gap between both systems such as utilizing ultra-thin, highly porous inorganic separators within a microfluidic channel. This approach maintains the simplified, low-pressure plumbing of membrane-less configurations while providing a physical safeguard against crossover under dynamic load variations. By resolving these manufacturing and fluidic constraints through interdisciplinary collaboration, DMFC technologies can successfully transition from specialized academic subjects into commercially viable, sustainable energy solutions.

6.0 Conclusion

This review presents a comparative assessment of electrode development in conventional and membrane-less DMFC, emphasizing the operational principles, performance, and future prospects of each system. The MEA is a fundamental component of traditional DMFC, and it is typically CCS or CCM. The direct-spray method has emerged as a practicable fabrication approach due to its simplicity. On the other hand, membrane-less DMFCs establish a "virtual membrane" through co-laminar microfluidic flow, which eliminates the necessity for a physical membrane while still allowing for effective electrochemical separation. Electrode architecture serves as a pivotal determinant in governing the overall electrochemical performance and operational efficiency of fuel cell in both systems. In membrane-less configurations, electrodes are classified as flow-over, flow-through, and air-breathing types, with air-breathing electrodes exhibiting the most optimistic performance to date. In spite of this, the electrode fabrication process for membrane-less systems are still relatively unexplored and necessitates additional research to achieve optimal performance. Key challenges, including mechanical failure, long-term stability, and MEA durability, persist in impeding widespread implementation, despite substantial progress. Addressing these concerns is crucial for enhancing the operational reliability and longevity of the system. Ultimately, the advancement of electrode technologies in DMFCs is essential for the improvement of device performance and for the promotion of global sustainability initiatives, particularly SDG 7 (Affordable and Clean Energy) and SDG 13 (Climate Action) of the United Nations Sustainable Development Goals.

Acknowledgements

The authors gratefully acknowledge the financial support from The Ministry of Higher Education and University Kebangsaan Malaysia under Grant Number HiCoE (SelFuel): HiCoE -2023-001.

Author Contributions

The authors declare that they contributed equally to all stages of this manuscript and research.

Declaration of Competing Interest

The authors declare that they have no known competing financial interests or personal relationships that could have appeared to influence the work reported in this paper.

References

[1] National Renewable Energy Policy and Action Plan | ESCAP Policy Documents Managment n.d. https://policy.asiapacificenergy.org/node/1218 (accessed December 26, 2023).
[2] Yeo: Malaysia aiming for 20pc renewable energy use by 2025 | Malay Mail n.d. https://www.malaymail.com/news/malaysia/2019/09/03/yeo-malaysia-aiming-for-20pc-renewable-energy-use-by-2025/1786768 (accessed December 26, 2023).
[3] Osman SH, Kamarudin SK, Shaari N, Zakaria Z. Low-Temperature Fuel Cell Technology Development and Issues: An Overview. Arab J Sci Eng 2025. https://doi.org/10.1007/s13369-025-10045-9.
[4] Cacciola G, Antonucci V, Freni S. Technology up date and new strategies on fuel cells. J Power Sources 2001;100:67–79. https://doi.org/10.1016/S0378-7753(01)00884-9.
[5] Rao CRK, Trivedi DC. Chemical and electrochemical depositions of platinum group metals and their applications. Coord Chem Rev 2005;249:613–31. https://doi.org/10.1016/j.ccr.2004.08.015.
[6] Verma LK. Studies on methanol fuel cell. J Power Sources 2000;86:464–8. https://doi.org/10.1016/S0378-7753(99)00403-6.
[7] Hsieh C Te, Lin JY, Yang SY. Carbon nanotubes embedded with PtRu nanoparticles as methanol fuel cell electrocatalysts. Phys E Low-Dimensional Syst Nanostructures 2009;41:373–8. https://doi.org/10.1016/j.physe.2008.08.060.
[8] Osman SH, Kamarudin SK, Shaari N, Hanapi IH, Elham OSJ, Aminudin MA. Review on Direct Methanol Fuel Cells: Bridging the Gap between Theory and Application for Sustainable Energy Solutions. Energy and Fuels 2025. https://doi.org/10.1021/acs.energyfuels.4c05357.
[9] Porstmann S, Wannemacher T, Drossel W. A comprehensive comparison of state-of-the-art manufacturing methods for fuel cell bipolar plates including anticipated future industry trends. J Manuf Process 2020;60:366–83. https://doi.org/10.1016/j.jmapro.2020.10.041.
[10] Kjeang E, Djilali N, Sinton D. Microfluidic fuel cells: A review. J Power Sources 2009;186:353–69. https://doi.org/10.1016/j.jpowsour.2008.10.011.
[11] Goulet M-A, Kjeang E. Co-laminar flow cells for electrochemical energy conversion. J Power Sources 2014;260:186–96. https://doi.org/10.1016/j.jpowsour.2014.03.009.
[12] Esquivel JP, Buser JR, Lim CW, Domínguez C, Rojas S, Yager P, et al. Single-use paper-based hydrogen fuel cells for point-of-care diagnostic applications. J Power Sources 2017;342:442–51. https://doi.org/10.1016/j.jpowsour.2016.12.085.
[13] Abrego-Martínez JC, Moreno-Zuria A, Cuevas-Muñiz FM, Arriaga LG, Sun S, Mohamedi M. Design, fabrication and performance of a mixed-reactant membraneless micro direct methanol fuel cell stack. J Power Sources 2017;371:10–7. https://doi.org/10.1016/j.jpowsour.2017.10.026.

[14] Yeh E, Fu C, Hu L, Thakur R, Feng J, Lee LP. Self-powered integrated microfluidic point-of-care low-cost enabling (SIMPLE) chip 2017:1–12.
[15] Gajda I, Greenman J, Melhuish C, Ieropoulos I. Self-sustainable electricity production from algae grown in a microbial fuel cell system. Biomass and Bioenergy 2015;82:87–93. https://doi.org/10.1016/j.biombioe.2015.05.017.
[16] Zainoodin AM, Kamarudin SK, Daud WRW. Electrode in direct methanol fuel cells. Int J Hydrogen Energy 2010;35:4606–21. https://doi.org/10.1016/j.ijhydene.2010.02.036.
[17] Ramli ZAC, Shaari N, Saharuddin TST. Progress and major BARRIERS of nanocatalyst development in direct methanol fuel cell: A review. Int J Hydrogen Energy 2022;47:22114–46. https://doi.org/10.1016/j.ijhydene.2022.04.239.
[18] Ke Y, Yuan W, Liu Q, Zhou F, Guo W, Liu Z, et al. An overview of noncarbon support materials for membrane electrode assemblies in direct methanol fuel cells: Fundamental and applications. Mater Des 2023;233:112261. https://doi.org/10.1016/j.matdes.2023.112261.
[19] Jayakumar A, Madheswaran DK, Kumar NM. A critical assessment on functional attributes and degradation mechanism of membrane electrode assembly components in direct methanol fuel cells. Sustain 2021;13. https://doi.org/10.3390/su132413938.
[20] Zhang S, Jiang Y. Development of Membrane Electrode Assembly with Double-Catalytic Layer for Micro Direct Methanol Fuel Cell. Inventions 2024;9. https://doi.org/10.3390/inventions9010019.
[21] Halim EM, Chemchoub S, El Attar A, Salih FE, Oularbi L, EL RHAZI M. Recent Advances in Anode Metallic Catalysts Supported on Conducting Polymer-Based Materials for Direct Alcohol Fuel Cells. Front Energy Res 2022;10. https://doi.org/10.3389/fenrg.2022.843736.
[22] Gong L, Yang Z, Li K, Xing W, Liu C, Ge J. Recent development of methanol electrooxidation catalysts for direct methanol fuel cell. vol. 27. Elsevier B.V.; 2018.
[23] Wu B, Xu X, Dong G, Zhang M, Luo S, Leung DYC, et al. Computational modeling studies on microfluidic fuel cell: A prospective review. Renew Sustain Energy Rev 2024;191:114082. https://doi.org/10.1016/j.rser.2023.114082.
[24] Tanveer M, Ambreen T, Khan H, Man Kim G, Woo Park C. Paper-based microfluidic fuel cells and their applications: A prospective review. Energy Convers Manag 2022;264:115732. https://doi.org/10.1016/j.enconman.2022.115732.
[25] Wang Y, Luo S, Kwok HYH, Pan W, Zhang Y, Zhao X, et al. Microfluidic fuel cells with different types of fuels: A prospective review. Renew Sustain Energy Rev 2021;141:110806. https://doi.org/10.1016/j.rser.2021.110806.
[26] Tanveer M, Su Lim E, Kim KY. Effects of channel geometry and electrode architecture on reactant transportation in membraneless microfluidic fuel cells: A review. Fuel 2021;298:120818. https://doi.org/10.1016/j.fuel.2021.120818.
[27] Tanveer M, Kim KY. Flow configurations of membraneless microfluidic fuel cells: A review. Energies 2021;14. https://doi.org/10.3390/en14123381.
[28] Hanapi IH, Kamarudin SK, Zainoodin AM, Hasran UA. Membrane-less micro fuel cell system design and performance: An overview. Int J Energy Res 2019;43:8956–72. https://doi.org/10.1002/er.4804.
[29] Yu X, Manthiram A. Scalable Membraneless Direct Liquid Fuel Cells Based on a Catalyst-Selective Strategy. Energy Environ Mater 2018;1:13–9. https://doi.org/10.1002/eem2.12000.
[30] Goel S. From waste to watts in micro-devices: Review on development of Membraned and Membraneless Microfluidic Microbial Fuel Cell. Appl Mater Today 2018;11:270–9. https://doi.org/10.1016/j.apmt.2018.03.005.
[31] Bamgbopa MO, Almheiri S, Sun H. Prospects of recently developed membraneless cell designs for redox flow batteries. Renew Sustain Energy Rev 2017;70:506–18.

https://doi.org/10.1016/j.rser.2016.11.234.
[32] Bianchini C, Shen PK. Palladium-based electrocatalysts for alcohol oxidation in half cells and in direct alcohol fuel cells. Chem Rev 2009;109:4183–206. https://doi.org/10.1021/cr9000995.
[33] Dutta K, Kumar P, Das S, Kundu PP. Utilization of conducting polymers in fabricating polymer electrolyte membranes for application in direct methanol fuel cells. Polym Rev 2014;54:1–32. https://doi.org/10.1080/15583724.2013.839566.
[34] Ozoemena KI. Nanostructured platinum-free electrocatalysts in alkaline direct alcohol fuel cells: Catalyst design, principles and applications. RSC Adv 2016;6:89523–50. https://doi.org/10.1039/c6ra15057h.
[35] Cai W, Fan K, Li J, Ma L, Xu G, Xu S, et al. A bi-functional polymeric nano-sieve Nafion composite membrane: Improved performance for direct methanol fuel cell applications. Int J Hydrogen Energy 2016;41:17102–11. https://doi.org/10.1016/j.ijhydene.2016.07.128.
[36] Xu X, Wang H, Lu S, Peng S, Xiang Y. A phosphotungstic acid self-anchored hybrid proton exchange membrane for direct methanol fuel cells. RSC Adv 2016;6:43049–55. https://doi.org/10.1039/c6ra07318b.
[37] You PY, Kamarudin SK, Masdar MS. Improved performance of sulfonated polyimide composite membranes with rice husk ash as a bio-filler for application in direct methanol fuel cells. Int J Hydrogen Energy 2019;44:1857–66. https://doi.org/10.1016/j.ijhydene.2018.11.166.
[38] Berretti E, Osmieri L, Baglio V, Miller HA, Filippi J, Vizza F, et al. Direct Alcohol Fuel Cells: A Comparative Review of Acidic and Alkaline Systems. vol. 6. Springer Nature Singapore; 2023. https://doi.org/10.1007/s41918-023-00189-3.
[39] Vecchio C Lo, Lyu X, Gatto I, Zulevi B, Serov A, Baglio V. Performance investigation of alkaline direct methanol fuel cell with commercial PGM-free cathodic materials. J Power Sources 2023;561:1–6. https://doi.org/10.1016/j.jpowsour.2023.232732.
[40] Antolini E, Gonzalez ER. Alkaline direct alcohol fuel cells. J Power Sources 2010;195:3431–50. https://doi.org/10.1016/j.jpowsour.2009.11.145.
[41] Papadias DD, Ahluwalia RK, Thomson JK, Meyer HM, Brady MP, Wang H, et al. Degradation of SS316L bipolar plates in simulated fuel cell environment: Corrosion rate, barrier film formation kinetics and contact resistance. J Power Sources 2015;273:1237–49. https://doi.org/10.1016/j.jpowsour.2014.02.053.
[42] Hren M, Božič M, Fakin D, Kleinschek KS, Gorgieva S. Alkaline membrane fuel cells: Anion exchange membranes and fuels. Sustain Energy Fuels 2021;5:604–37. https://doi.org/10.1039/d0se01373k.
[43] Rizo R, Arán-Ais RM, Padgett E, Muller DA, Lázaro MJ, Solla-Gullón J, et al. Pt-Richcore/Sn-Richsubsurface/Ptskin Nanocubes As Highly Active and Stable Electrocatalysts for the Ethanol Oxidation Reaction. J Am Chem Soc 2018;140:3791–7. https://doi.org/10.1021/jacs.8b00588.
[44] Li W, Fang J, Lv M, Chen C, Chi X, Yang Y, et al. Novel anion exchange membranes based on polymerizable imidazolium salt for alkaline fuel cell applications. J Mater Chem 2011;21:11340–6. https://doi.org/10.1039/c1jm11093d.
[45] Ye YS, Cheng MY, Xie XL, Rick J, Huang YJ, Chang FC, et al. Alkali doped polyvinyl alcohol/graphene electrolyte for direct methanol alkaline fuel cells. J Power Sources 2013;239:424–32. https://doi.org/10.1016/j.jpowsour.2013.03.021.
[46] Sajjad SD, Liu D, Wei Z, Sakri S, Shen Y, Hong Y, et al. Guanidinium based blend anion exchange membranes for direct methanol alkaline fuel cells (DMAFCs). J Power Sources 2015;300:95–103. https://doi.org/10.1016/j.jpowsour.2015.08.002.
[47] Gupta UK, Pramanik H. Electrooxidation study of pure ethanol/methanol and their mixture for the application in direct alcohol alkaline fuel cells (DAAFCs). Int J Hydrogen

Energy 2019:421–35. https://doi.org/10.1016/j.ijhydene.2018.03.008.
[48] Varcoe JR, Slade RCT, Yee ELH, Poynton SD, Driscoll DJ. Investigations into the ex situ methanol, ethanol and ethylene glycol permeabilities of alkaline polymer electrolyte membranes. J Power Sources 2007;173:194–9. https://doi.org/10.1016/j.jpowsour.2007.04.068.
[49] Burhan H, Cellat K, Yılmaz G, Şen F. Investigation of Fumasep® FAA3-50 Membranes in Alkaline Direct Methanol Fuel Cells Carmelo. Direct Liq Fuel Cells Fundam Adv Futur 2020:71–94. https://doi.org/10.1016/B978-0-12-818624-4.00003-0.
[50] Zakaria Z, Shaari N, Kamarudin SK. Preliminary Study of Alkaline Direct Ethanol Fuel Cell by using Crosslinked Quaternized Poly (Vinyl Alcohol)/Graphene Oxide Membrane. J Kejuruter 2018;30:219–27. https://doi.org/10.17576/jkukm-2018-30(2)-12.
[51] Shaari N, Kamarudin SK, Zakaria Z. Enhanced alkaline stability and performance of alkali-doped quaternized poly(vinyl alcohol) membranes for passive direct ethanol fuel cell. Int J Energy Res 2019;43:5252–65. https://doi.org/10.1002/er.4513.
[52] Nguyen N-T, Wereley ST, House A. Fundamentals and Applications of Microfluidics - Second Edition. 2002.
[53] Whitesides GM. The origins and the future of microfluidics. Nature 2006;442:368–73. https://doi.org/10.1038/nature05058.
[54] Petrovic S, Hossain E. Development of a Novel Technological Readiness Assessment Tool for Fuel Cell Technology. IEEE Access 2020;8:132237–52. https://doi.org/10.1109/ACCESS.2020.3009193.
[55] Choban E. Microfluidic fuel cell based on laminar flow. J Power Sources 2004;128:54–60. https://doi.org/10.1016/j.jpowsour.2003.11.052.
[56] Ha S-M, Ahn Y. Laminar flow-based micro fuel cell utilizing grooved electrode surface. J Power Sources 2014;267:731–8. https://doi.org/10.1016/j.jpowsour.2014.06.005.
[57] Hanapi IH, Kamarudin SK, Zainoodin AM, Hasran UA. Optimization of Multiple Reactants in a Membrane-Less Direct Methanol Fuel Cell (DMFC) 2023:1–20.
[58] Cohen JL, Westly DA, Pechenik A, Abruña HD. Fabrication and preliminary testing of a planar membraneless microchannel fuel cell. J Power Sources 2005;139:96–105. https://doi.org/10.1016/j.jpowsour.2004.06.072.
[59] Choban ER, Spendelow JS, Gancs L, Wieckowski A, Kenis PJA. Membraneless laminar flow-based micro fuel cells operating in alkaline, acidic, and acidic/alkaline media. Electrochim Acta 2005;50:5390–8. https://doi.org/10.1016/j.electacta.2005.03.019.
[60] Ponmani K, Durga S, Arun A, Kiruthika S, Muthukumaran B. Development of Membraneless Sodium Perborate Fuel Cell for Media Flexible Power Generation. Int J Electrochem 2014;2014:1–9. https://doi.org/10.1155/2014/962161.
[61] Rathoure AK, Pramanik H. Electrooxidation study of methanol using H 2 O 2 and air as mixed oxidant at cathode in air breathing microfluidic fuel cell. Int J Hydrogen Energy 2016;41:15287–94. https://doi.org/10.1016/j.ijhydene.2016.07.058.
[62] Chen F, Chang MH, Hsu CW. Analysis of membraneless microfuel cell using decomposition of hydrogen peroxide in a Y-shaped microchannel. Electrochim Acta 2007;52:7270–7. https://doi.org/10.1016/j.electacta.2007.05.072.
[63] Rahim AHA, Salami A, Kamarudin SK, Hanapi S. An overview of polymer electrolyte membrane electrolyzer for hydrogen production : Modeling and mass transport. J Power Sources 2016;309:56–65. https://doi.org/10.1016/j.jpowsour.2016.01.012.
[64] Chen Z, Cao J, Chen Z, Xu J, Wang W. Mesoporous carbon synthesized from dual colloidal silica/block copolymer template approach as the support of platinum nanoparticles for direct methanol fuel cells. Electrochim Acta 2013;88:184–92. https://doi.org/10.1016/j.electacta.2012.10.030.
[65] Jha N, Jafri RI, Rajalakshmi N, Ramaprabhu S. Graphene-multi walled carbon

nanotube hybrid electrocatalyst support material for direct methanol fuel cell. Int J Hydrogen Energy 2011;36:7284–90. https://doi.org/10.1016/j.ijhydene.2011.03.008.
[66] Kanninen P, Borghei M, Sorsa O, Pohjalainen E, Kauppinen EI, Ruiz V, et al. Highly efficient cathode catalyst layer based on nitrogen-doped carbon nanotubes for the alkaline direct methanol fuel cell. Appl Catal B Environ 2014;156–157:341–9. https://doi.org/10.1016/j.apcatb.2014.03.041.
[67] Borghei M, Scotti G, Kanninen P, Weckman T, Anoshkin I V., Nasibulin AG, et al. Enhanced performance of a silicon microfabricated direct methanol fuel cell with PtRu catalysts supported on few-walled carbon nanotubes. Energy 2014;65:612–20. https://doi.org/10.1016/j.energy.2013.11.067.
[68] Deng H, Zhang Y, Zheng X, Li Y, Zhang X, Liu X. A CNT (carbon nanotube) paper as cathode gas diffusion electrode for water management of passive μ-DMFC (micro-direct methanol fuel cell) with highly concentrated methanol. Energy 2015;82:236–41. https://doi.org/10.1016/j.energy.2015.01.034.
[69] Bruno MM, Viva FA, Petruccelli MA, Corti HR. Platinum supported on mesoporous carbon as cathode catalyst for direct methanol fuel cells. J Power Sources 2015;278:458–63. https://doi.org/10.1016/j.jpowsour.2014.12.097.
[70] Kang YS, Jung N, Choi KH, Lee MJ, Ahn M, Cho YH, et al. Anode electrode with carbon buffer layer for improving methanol oxidation reaction in direct methanol fuel cell. Appl Surf Sci 2014;290:246–51. https://doi.org/10.1016/j.apsusc.2013.11.059.
[71] Zainoodin AM, Kamarudin SK, Masdar MS, Daud WRW, Mohamad AB, Sahari J. High power direct methanol fuel cell with a porous carbon nanofiber anode layer. Appl Energy 2014;113:946–54. https://doi.org/10.1016/j.apenergy.2013.07.066.
[72] Yan XH, Wu R, Xu JB, Luo Z, Zhao TS. A monolayer graphene - Nafion sandwich membrane for direct methanol fuel cells. J Power Sources 2016;311:188–94. https://doi.org/10.1016/j.jpowsour.2016.02.030.
[73] Schlange A, Dos Santos AR, Hasse B, Etzold BJM, Kunz U, Turek T. Titanium carbide-derived carbon as a novel support for platinum catalysts in direct methanol fuel cell application. J Power Sources 2012;199:22–8. https://doi.org/10.1016/j.jpowsour.2011.09.107.
[74] Yuan T, Yang J, Wang Y, Ding H, Li X, Liu L, et al. Anodic diffusion layer with graphene-carbon nanotubes composite material for passive direct methanol fuel cell. Electrochim Acta 2014;147:265–70. https://doi.org/10.1016/j.electacta.2014.09.124.
[75] Rambabu G, Bhat SD. Sulfonated fullerene in SPEEK matrix and its impact on the membrane electrolyte properties in direct methanol fuel cells. Electrochim Acta 2015;176:657–69. https://doi.org/10.1016/j.electacta.2015.07.045.
[76] Morales-Acosta D, Morales-Acosta MD, Godinez LA, Álvarez-Contreras L, Duron-Torres SM, Ledesma-García J, et al. PdCo supported on multiwalled carbon nanotubes as an anode catalyst in a microfluidic formic acid fuel cell. J Power Sources 2011;196:9270–5. https://doi.org/10.1016/j.jpowsour.2011.07.064.
[77] Salloum KS, Posner JD. A membraneless microfluidic fuel cell stack. J Power Sources 2011;196:1229–34. https://doi.org/10.1016/j.jpowsour.2010.08.069.
[78] Gago AS, Morales-Acosta D, Arriaga LG, Alonso-Vante N. Carbon supported ruthenium chalcogenide as cathode catalyst in a microfluidic formic acid fuel cell. J Power Sources 2011;196:1324–8. https://doi.org/10.1016/j.jpowsour.2010.08.109.
[79] Brushett FR, Naughton MS, Ng JWD, Yin L, Kenis PJA. Analysis of Pt/C electrode performance in a flowing-electrolyte alkaline fuel cell. Int J Hydrogen Energy 2012;37:2559–70. https://doi.org/10.1016/j.ijhydene.2011.10.078.
[80] López-Montesinos PO, Yossakda N, Schmidt A, Brushett FR, Pelton WE, Kenis PJA. Design, fabrication, and characterization of a planar, silicon-based, monolithically integrated micro laminar flow fuel cell with a bridge-shaped microchannel cross-section. J Power Sources

2011;196:4638–45. https://doi.org/10.1016/j.jpowsour.2011.01.037.
[81] Moore S, Sinton D, Erickson D. A plate-frame flow-through microfluidic fuel cell stack. J Power Sources 2011;196:9481–7. https://doi.org/10.1016/j.jpowsour.2011.07.024.
[82] Lee JW, Kjeang E. Chip-embedded thin film current collector for microfluidic fuel cells. Int J Hydrogen Energy 2012;37:9359–67. https://doi.org/10.1016/j.ijhydene.2012.02.155.
[83] Lee JW, Hong JK, Kjeang E. Electrochemical characteristics of vanadium redox reactions on porous carbon electrodes for microfluidic fuel cell applications. Electrochim Acta 2012;83:430–8. https://doi.org/10.1016/j.electacta.2012.07.104.
[84] Mousavi Shaegh SA, Nguyen N-T, Chan SH. Air-breathing microfluidic fuel cell with fuel reservoir. J Power Sources 2012;209:312–7. https://doi.org/10.1016/j.jpowsour.2012.02.115.
[85] Jindal A, Basu S, Chauhan N, Ukai T, Kumar DS, Samudhyatha KT. Application of electrospun CNxnanofibers as cathode in microfluidic fuel cell. J Power Sources 2017;342:165–74. https://doi.org/10.1016/j.jpowsour.2016.12.047.
[86] Shahgaldi S, Alaefour I, Li X. Impact of manufacturing processes on proton exchange membrane fuel cell performance. Appl Energy 2018;225:1022–32. https://doi.org/10.1016/j.apenergy.2018.05.086.
[87] Shahgaldi S, Zhao J, Alaefour I, Li X. Investigation of catalytic vs reactant transport effect of catalyst layers on proton exchange membrane fuel cell performance. Fuel 2017;208:321–8. https://doi.org/10.1016/j.fuel.2017.07.035.
[88] Martin S, Garcia-Ybarra PL, Castillo JL. Long-term operation of a proton exchange membrane fuel cell without external humidification. Appl Energy 2017;205:1012–20. https://doi.org/10.1016/j.apenergy.2017.08.157.
[89] Chun YG, Kim CS, Peck DH, Shin DR. Performance of a polymer electrolyte membrane fuel cell with thin film catalyst electrodes. J Power Sources 1998;71:174–8. https://doi.org/10.1016/S0378-7753(97)02792-4.
[90] Lee HK, Park JH, Kim DY, Lee TH. A study on the characteristics of the diffusion layer thickness and porosity of the PEMFC. J Power Sources 2004;131:200–6. https://doi.org/10.1016/j.jpowsour.2003.12.039.
[91] Kim CS, Chun YG, Peck DH, Shin DR. A novel process to fabricate membrane electrode assemblies for proton exchange membrane fuel cells. Int J Hydrogen Energy 1998;23:1045–8. https://doi.org/10.1016/S0360-3199(98)00021-4.
[92] Lee E, Kim DH, Pak C. Effects of cathode catalyst layer fabrication parameters on the performance of high-temperature polymer electrolyte membrane fuel cells. Appl Surf Sci 2020;510:145461. https://doi.org/10.1016/j.apsusc.2020.145461.
[93] Gallo Stampino P, Cristiani C, Dotelli G, Omati L, Zampori L, Pelosato R, et al. Effect of different substrates, inks composition and rheology on coating deposition of microporous layer (MPL) for PEM-FCs. Catal Today 2009;147:30–5. https://doi.org/10.1016/j.cattod.2009.07.023.
[94] Achmad F, Kamarudin SK, Daud WRW, Majlan EH. Passive direct methanol fuel cells for portable electronic devices. Appl Energy 2011;88:1681–9. https://doi.org/10.1016/j.apenergy.2010.11.012.
[95] Zainoodin AM, Tsujiguchi T, Masdar MS, Kamarudin SK, Osaka Y, Kodama A. Performance of a direct formic acid fuel cell fabricated by ultrasonic spraying. Int J Hydrogen Energy 2018;43:6413–20. https://doi.org/10.1016/j.ijhydene.2018.02.024.
[96] Fofana D, Natarajan SK, Hamelin J, Benard P. Low platinum, high limiting current density of the PEMFC (proton exchange membrane fuel cell) based on multilayer cathode catalyst approach. Energy 2014;64:398–403. https://doi.org/10.1016/j.energy.2013.10.021.
[97] Kim GH, Eom KS, Kim MJ, Yoo SJ, Jang JH, Kim HJ, et al. Design of an Advanced

Membrane Electrode Assembly Employing a Double-Layered Cathode for a PEM Fuel Cell. ACS Appl Mater Interfaces 2015;7:27581–5. https://doi.org/10.1021/acsami.5b07346.
[98] Shahgaldi S, Alaefour I, Li X. The impact of short side chain ionomer on polymer electrolyte membrane fuel cell performance and durability. Appl Energy 2018;217:295–302. https://doi.org/10.1016/j.apenergy.2018.02.154.
[99] Wang S, Shang Y, Wang Y, Wang J. Fabrication and electrochemical performance of Poly (2,5-benzimidazole) (ABPBI)-based MEA by catalyst coated membrane (CCM) method for high-temperature polymer electrolyte fuel cells. Int J Hydrogen Energy 2013;38:11060–6. https://doi.org/10.1016/j.ijhydene.2013.01.102.
[100] Liang H, Su H, Pollet BG, Linkov V, Pasupathi S. Membrane electrode assembly with enhanced platinum utilization for high temperature proton exchange membrane fuel cell prepared by catalyst coating membrane method. J Power Sources 2014;266:107–13. https://doi.org/10.1016/j.jpowsour.2014.05.014.
[101] Liang H, Su H, Pollet BG, Pasupathi S. Development of membrane electrode assembly for high temperature proton exchange membrane fuel cell by catalyst coating membrane method. J Power Sources 2015;288:121–7. https://doi.org/10.1016/j.jpowsour.2015.04.123.
[102] Hu M, Sui S, Zhu X, Yu Q, Cao G, Hong X, et al. A 10 kW class PEM fuel cell stack based on the catalyst-coated membrane (CCM) method. Int J Hydrogen Energy 2006;31:1010–8. https://doi.org/10.1016/j.ijhydene.2006.02.018.
[103] Hnát J, Plevova M, Tufa RA, Zitka J, Paidar M, Bouzek K. Development and testing of a novel catalyst-coated membrane with platinum-free catalysts for alkaline water electrolysis. Int J Hydrogen Energy 2019;44:17493–504. https://doi.org/10.1016/j.ijhydene.2019.05.054.
[104] Tang H, Wang S, Jiang SP, Pan M. A comparative study of CCM and hot-pressed MEAs for PEM fuel cells. J Power Sources 2007;170:140–4. https://doi.org/10.1016/j.jpowsour.2007.03.062.
[105] Sadeghi Alavijeh A, Khorasany RMH, Habisch A, Wang GG, Kjeang E. Creep properties of catalyst coated membranes for polymer electrolyte fuel cells. J Power Sources 2015;285:16–28. https://doi.org/10.1016/j.jpowsour.2015.03.082.
[106] Zhang J. PEM fuel cell electrocatalysts and catalyst layers: Fundamentals and applications. 2008. https://doi.org/10.1007/978-1-84800-936-3.
[107] Song SQ, Liang ZX, Zhou WJ, Sun GQ, Xin Q, Stergiopoulos V, et al. Direct methanol fuel cells: The effect of electrode fabrication procedure on MEAs structural properties and cell performance. J Power Sources 2005;145:495–501. https://doi.org/10.1016/j.jpowsour.2005.02.069.
[108] Sarkar J, Bhattacharyya S. Application of graphene and graphene-based materials in clean energy-related devices Minghui. Arch Thermodyn 2012;33:23–40. https://doi.org/10.1002/er.
[109] Li Y, Fu Z, Li Y, Zhang G. A Comparative Study of CCM and CCS Membrane Electrode Assemblies for High-Temperature Proton Exchange Membrane Fuel Cells with a CsH5(PO4)2-Doped Polybenzimidazole Membrane. Materials (Basel) 2023;16. https://doi.org/10.3390/ma16113925.
[110] Rohendi D, Syarif N, Said M, Utami MT, Marcelina Y. Utilization of catalyst-coated membrane (CCM) and spraying methods in fabrication membrane electrode assembly (MEA) for direct methanol fuel Cell (DMFC) using Pt-Co / C catalyst. J Phys Conf Ser 2019;1282. https://doi.org/10.1088/1742-6596/1282/1/012065.
[111] Mauger SA, Wang M, Cetinbas FC, Dzara MJ, Park J, Myers DJ, et al. Development of high-performance roll-to-roll-coated gas-diffusion-electrode-based fuel cells. J Power Sources 2021;506:230039. https://doi.org/10.1016/j.jpowsour.2021.230039.
[112] Breitwieser M, Klingele M, Vierrath S, Zengerle R, Thiele S. Tailoring the Membrane-

Electrode Interface in PEM Fuel Cells: A Review and Perspective on Novel Engineering Approaches. Adv Energy Mater 2018;8. https://doi.org/10.1002/aenm.201701257.
[113] Jinnouchi R, Kudo K, Kodama K, Kitano N, Suzuki T, Minami S, et al. The role of oxygen-permeable ionomer for polymer electrolyte fuel cells. Nat Commun 2021;12. https://doi.org/10.1038/s41467-021-25301-3.
[114] Lee CH, Kort-Kamp WJM, Yu H, Cullen DA, Patterson BM, Arman TA, et al. Grooved electrodes for high-power-density fuel cells. Nat Energy 2023;8:685–94. https://doi.org/10.1038/s41560-023-01263-2.
[115] Mousavi Shaegh SA, Nguyen NT, Chan SH. A review on membraneless laminar flow-based fuel cells. Int J Hydrogen Energy 2011;36:5675–94. https://doi.org/10.1016/j.ijhydene.2011.01.063.
[116] Ferrigno R, Stroock AD, Clark TD, Mayer M, Whitesides GM. Membraneless Vanadium Redox Fuel Cell Using Laminar Flow. J Am Chem Soc 2002;124:12930–1. https://doi.org/10.1021/ja020812q.
[117] Tominaka S, Obata H, Osaka T. On-chip direct methanol fuel cells of a monolithic design: Consideration on validity of active-type system. Energy Environ Sci 2009;2:845–8. https://doi.org/10.1039/b904339j.
[118] Maynard HL, Meyers JP. Miniature fuel cells for portable power: Design considerations and challenges. J Vac Sci Technol B Microelectron Nanom Struct Process Meas Phenom 2002;20:1287–97. https://doi.org/10.1116/1.1488641.
[119] Sun MH, Velve Casquillas G, Guo SS, Shi J, Ji H, Ouyang Q, et al. Characterization of microfluidic fuel cell based on multiple laminar flow. Microelectron Eng 2007;84:1182–5. https://doi.org/10.1016/j.mee.2007.01.175.
[120] Mota N Da, Finkelstein DA, Kirtland JD, Rodriguez CA, Stroock AD, Abruña HD. Membraneless, room-temperature, direct borohydride/cerium fuel cell with power density of over 0.25 W/cm 2. J Am Chem Soc 2012;134:6076–9. https://doi.org/10.1021/ja211751k.
[121] Liu Z, Ye D, Chen R, Zhang B, Zhu X, Liao Q. A dual-functional three-dimensional herringbone-like electrode for a membraneless microfluidic fuel cell. J Power Sources 2019;438:227058. https://doi.org/10.1016/j.jpowsour.2019.227058.
[122] Kjeang E, Michel R, Harrington DA, Djilali N, Sinton D. A microfluidic fuel cell with flow-through porous electrodes. J Am Chem Soc 2008;130:4000–6. https://doi.org/10.1021/ja078248c.
[123] Salloum KS, Posner JD. Counter flow membraneless microfluidic fuel cell. J Power Sources 2010;195:6941–4. https://doi.org/10.1016/j.jpowsour.2010.03.096.
[124] Krishnamurthy D, Johansson EO, Lee JW, Kjeang E. Computational modeling of microfluidic fuel cells with flow-through porous electrodes. J Power Sources 2011;196:10019–31. https://doi.org/10.1016/j.jpowsour.2011.08.024.
[125] Li L, Nikiforidis G, Leung MKH, Daoud WA. Vanadium microfluidic fuel cell with novel multi-layer flow-through porous electrodes: Model, simulations and experiments. Appl Energy 2016;177:729–39. https://doi.org/10.1016/j.apenergy.2016.05.072.
[126] Li L, Bei S, Liu R, Xu Q, Zheng K, She Y, et al. Design of a radial vanadium redox microfluidic fuel cell: A new way to break the size limitation. Int J Energy Res 2019;43:3028–37. https://doi.org/10.1002/er.4473.
[127] Tanveer M, Kim KY. Performance analysis of microfluidic fuel cells with various inlet locations and multiple compartments. Energy Convers Manag 2018;166:328–36. https://doi.org/10.1016/j.enconman.2018.04.043.
[128] Wang Y, Leung DYC, Zhang H, Xuan J, Wang H. Numerical and experimental comparative study of microfluidic fuel cells with different flow configurations: Co-flow vs. counter-flow cell. Appl Energy 2017;203:535–48. https://doi.org/10.1016/j.apenergy.2017.06.070.

[129] Salloum KS, Hayes JR, Friesen CA, Posner JD. Sequential flow membraneless microfluidic fuel cell with porous electrodes. J Power Sources 2008;180:243–52. https://doi.org/10.1016/j.jpowsour.2007.12.116.
[130] Zhang B, Ye D, Li J, Zhu X, Liao Q. Electrodeposition of Pd catalyst layer on graphite rod electrodes for direct formic acid oxidation. J Power Sources 2012;214:277–84. https://doi.org/10.1016/j.jpowsour.2012.04.007.
[131] Jayashree RS, Gancs L, Choban ER, Primak A, Natarajan D, Markoski LJ, et al. Air-Breathing Laminar Flow-Based Microfluidic Fuel Cell. J Am Chem Soc 2005;127:16758–9. https://doi.org/10.1021/ja054599k.
[132] Xuan J, Leung DYC, Wang H, Leung MKH, Wang B, Ni M. Air-breathing membraneless laminar flow-based fuel cells: Do they breathe enough oxygen? Appl Energy 2013;104:400–7. https://doi.org/10.1016/j.apenergy.2012.10.063.
[133] Zhu X, Zhang B, Ye DD, Li J, Liao Q. Air-breathing direct formic acid microfluidic fuel cell with an array of cylinder anodes. J Power Sources 2014;247:346–53. https://doi.org/10.1016/j.jpowsour.2013.08.119.
[134] Ye DD, Zhang B, Zhu X, Sui PC, Djilali N, Liao Q. Computational modeling of alkaline air-breathing microfluidic fuel cells with an array of cylinder anodes. J Power Sources 2015;288:150–9. https://doi.org/10.1016/j.jpowsour.2015.04.087.
[135] Wang H, Leung DYC, Xuan J. Modeling of an air cathode for microfluidic fuel cells: Transport and polarization behaviors. Int J Hydrogen Energy 2011;36:14704–18. https://doi.org/10.1016/j.ijhydene.2011.08.033.
[136] Zhu X, Zhou Y, Ye D-D, Chen R, Zhang T, Liao Q. Discrete-holes film fueling anode heads for high performance air-breathing microfluidic fuel cell. J Power Sources 2021;482:228966. https://doi.org/10.1016/j.jpowsour.2020.228966.
[137] Zhou Y, Zhang B, Zhu X, Ye DD, Chen R, Zhang T, et al. Enhancing fuel transport in air-breathing microfluidic fuel cells by immersed fuel micro-jet. J Power Sources 2020;445:227326. https://doi.org/10.1016/j.jpowsour.2019.227326.
[138] Shyu JC, Wang PY, Lee CL, Chang SC, Sheu TS, Kuo CH, et al. Fabrication and test of an air-breathing microfluidic fuel cell. Energies 2015;8:2082–96. https://doi.org/10.3390/en8032082.
[139] Ortiz-Ortega E, Díaz-Patiño L, Bejar J, Trejo G, Guerra-Balcázar M, Espinosa-Magaña F, et al. A Flow-Through Membraneless Microfluidic Zinc-Air Cell. ACS Appl Mater Interfaces 2020;12:41185–99. https://doi.org/10.1021/acsami.0c08525.
[140] Tanveer M, Kim KY. A membraneless microfluidic fuel cell with a hollow flow channel and porous flow-through electrodes. Int J Energy Res 2021;45:8536–50. https://doi.org/10.1002/er.6390.
[141] Ibáñez SE, Quintero AE, García-Salaberri PA, Vera M. Effects of the diffusive mixing and self-discharge reactions in microfluidic membraneless vanadium redox flow batteries. Int J Heat Mass Transf 2021;170:121022. https://doi.org/10.1016/j.ijheatmasstransfer.2021.121022.
[142] Li L, Ling L, Xie Y, Shan S, Bei S, Zheng K, et al. Counter-flow microfluidic fuel cell with trapezoidal electrodes. Sustain Energy Technol Assessments 2023;56. https://doi.org/10.1016/j.seta.2022.103005.
[143] Liu H, Xu Y, Zhang S, Zhou Y, Liu N, Liu J, et al. High cost-performance direct ammonia microfluidic fuel cell benefited from nickel nanoparticle anode and catalyst-free cathode. Int J Hydrogen Energy 2024;69:1417–25. https://doi.org/10.1016/j.ijhydene.2024.05.160.
[144] China: Yuantong Debuts A Direct Methanol Fuel Cell Logistics Vehicle - FuelCellsWorks n.d. https://fuelcellsworks.com/news/china-yuantong-debuts-a-direct-methanol-fuel-cell-logistics-vehicle/ (accessed January 28, 2024).

[145] Romagnoli M, Testa V, Romagnoli M, Testa V. Perspective Chapter: Methanol as a Fuel for Direct Methanol Fuel Cells (DMFCs) – Principles and Performance. Methanol Fuel Transp Sect Fuel Cells 2023. https://doi.org/10.5772/INTECHOPEN.1002872.
[146] Lo Vecchio C, Serov A, Dicome M, Zulevi B, Aricò AS, Baglio V. Investigating the durability of a direct methanol fuel cell equipped with commercial Platinum Group Metal-free cathodic electro-catalysts. Electrochim Acta 2021;394. https://doi.org/10.1016/J.ELECTACTA.2021.139108.
[147] Liu X, Fan K, Huang X, Ge J, Liu Y, Kang H. Recent advances in artificial intelligence boosting materials design for electrochemical energy storage. Chem Eng J 2024;490. https://doi.org/10.1016/J.CEJ.2024.151625.
[148] Arora NK, Mishra I. Sustainable development goal 13: recent progress and challenges to climate action. Environ Sustain 2023;6:297–301. https://doi.org/10.1007/S42398-023-00287-4.

Malaysian Journal of Energy and Applications 1 (2026): 57-70
https://doi.org/10.17576/myjea.2026.01.57

QUATERNIZED POLY(VINYL ALCOHOL)/QUATERNIZED GRAPHENE OXIDE COMPOSITE MEMBRANES: IMPACT OF FILLER LOADING ON PERFORMANCE

Kiranraj Vaiyanan Kannan[1], Ramanidevi Balachandran[2], Wai Yin Wong[1] &
Mohd Shahbudin Mastar @ Masdar[1,2]*

[1] *Fuel Cell Institute, Universiti Kebangsaan Malaysia, 43600 UKM Bangi, Selangor.*
[2] *Faculty of Engineering & Built Environment, Universiti Kebangsaan Malaysia.*

**Corresponding author email: shahbud@ukm.edu.my*

Received 1/7/2026; Received in Revised Form 13/7/2026;
Accepted 13/7/2026; Available Online 20/07/2026.

Abstract

As global efforts accelerate toward deep decarbonisation, anion exchange membrane (AEM) water electrolysis offers a versatile, zero-emission pathway to generate green hydrogen for heavy industries, grids, and hydrogen fuel cells. Pristine polyvinyl alcohol has lower conductivity and ion exchange capacity compared to quaternized polyvinyl alcohol (QPVA) due to low cationic region. Hence, QPVA faces several challenges such as lower ionic conductivity compared to commercial AEM standards, poor alkaline stability, excessive KOH uptake that causes over swelling and lower durability (membrane becomes soft). These challenges can be mitigated by studying the parameters of polymer modifications by studying implementing of nanofillers with different weight percentage ratio of quaternized graphene oxide (QGO) filler to improve ionic conductivity, improve mechanical properties of membrane while reducing excessive swelling and with degree of crosslinking can reduce overswell while improving mechanical strength. Here, composite AEMs based on quaternized poly(vinyl alcohol) (QPVA) and quaternized graphene oxide (QGO) were fabricated via doctor blade casting to evaluate the effect of QGO loading (0.5, 1.0, and 2.0 wt.%). FTIR, XRD, and FESEM-EDX confirmed successful functionalization, revealing a homogeneous filler dispersion at 1.0 wt.% but particle agglomeration at 2.0 wt.%. QGO inclusion directly modulated the dynamic viscosity, surface tension, and water contact angle of the casting solutions. Upon transitioning from 5.0 M KOH activation to 1.0 M KOH equilibration, the optimized 1.0 wt.% membrane minimized thickness swelling to 4.88% while achieving a peak ionic conductivity of 10.79 mS/cm due to its uniform microstructural pathways. Conversely, the over-loaded 2.0 wt.% sample uniquely exhibited simultaneous increases in swelling (8.29% to 8.92%) and conductivity (2.95 to 4.47 mS/cm) as water pooled within agglomeration-induced micro voids. Overall, these findings demonstrate that optimizing QGO loading to 1.0 wt.% via controlled doctor blade casting yields structurally stable composite AEMs suitable for its exploration in efficient green hydrogen generation.

Keywords: QPVA polymer matrix; QPVA/QGO composite membrane; Anion exchange membrane; green hydrogen; renewable fuel source

1.0 Introduction

Anion exchange membrane (AEM) water electrolysis has emerged as a compelling green hydrogen production technology, merging the low operational costs of alkaline water electrolysis (AWE) with the high power density of proton exchange membrane (PEM) systems

[1].Beyond its primary application in powering clean hydrogen fuel cells, the high-purity green hydrogen produced via this method serves as a versatile, low-carbon energy carrier, facilitating deep decarbonization within heavy industries and enhancing the stability of renewable energy grids. By utilizing non-noble metal electrocatalysts and polymer-based membranes functionalized with quaternary ammonium cationic groups, AEM systems significantly lower capital costs while maintaining efficient ion transport [2]. However, AEM water electrolysis still faces operational setbacks during system operation that can reduce overall electrolyzer efficiency and hydrogen output [3]. In these setups, ion transport is heavily influenced by variables such as ionic conductivity, hydration levels, and membrane stability, where the AEM serves as the primary ion-conducting medium and electrical insulator [4].

The widespread application of AEMs is frequently hindered by low ionic conductivity, primarily attributed to slow hydroxide ion transport kinetics and low dissociation rates [4]. Consequently, structural and compositional modifications, such as the incorporation of inorganic fillers [5] and the optimization of membrane thickness, are essential to dictate the overall efficiency of the composite system [6-8].While not yet widely adopted as a standard industry material, polyvinyl alcohol (PVA)-based membranes have been explored as an affordable alternative for AEMs due to their cost-effectiveness, flexible polymer backbone modification, and chemical resistance. However, maintaining high operational efficiency remains a significant challenge; pristine PVA membranes often exhibit low ionic conductivity and excessive water uptake that compromises their structural integrity, leading to accelerated chemical degradation via Hofmann elimination or S_N2 pathways [9, 10].

To counteract these limitations, the introduction of quaternary ammonium (QA) groups into PVA via modification with glycidyltrimethylammonium chloride (GTMAC) yields quaternized polyvinyl alcohol (QPVA), which significantly enhances both ionic conductivity and mechanical stability [11].The electrochemical performance of these matrices can be further enhanced through the incorporation of inorganic fillers like graphene oxide (GO), where the interactions between QA groups and the oxygen-containing functional groups of GO improve the chemical, thermal, and mechanical stability of the composite membrane while creating hydrophilic domains that facilitate efficient ion transport [12]. Although GO-based membranes have shown improved ionic conductivity. Hence, in previous study Z, Zakaria et al. [11] only mentioned using QPVA/GO for ethanol-based fuel cell. Thus, functionalizing GO with quaternary ammonium groups using a dimethyloctadecyl [3-(trimethoxysilyl)propyl] ammonium chloride (DMAOP) precursor to produce quaternized graphene oxide (QGO) can enhance cationic region on QGO surface, in which increases as anion exchange capability and able to tune QPVA/QGO for AEM fuel cell and water electrolyser. [11, 13]. Beyond chemical composition, the fabrication technique is important, conventional solution casting shows moderate thickness control with uniformity at larger scale. In contrast, the doctor blade technique offers a robust, scalable alternative with superior thickness control and film consistency with even disperse on polymer solution and nanofillers throughout membrane surfaces [14].

Currently, a significant research gap exists regarding how the concurrent utilization of doctor blade casting as alternative casting method, PVA quaternization, and QGO filler incorporation that enhance anion exchange capability on membrane surfaces in which can be tailored to simultaneously optimize film uniformity, hydrolytic stability, and ionic conductivity. To address this gap, the objective of this study is to systematically synthesize and characterize QPVA/QGO composite membranes fabricated via the doctor blade technique at a targeted 50 µm baseline thickness across varying QGO loadings (0.5, 1.0, and 2.0 wt.%). The rheological and physicochemical properties of the QPVA/QGO solutions such as viscosity, surface tension, and contact angle are evaluated alongside membrane structural

characterizations (FESEM-EDX, FTIR, and XRD) to observe the resulting improvements in membrane homogeneity and electrochemical performance.

2.0 Experimental

2.1 Preparation of QPVA solution

Polyvinyl alcohol (PVA) was obtained from Sigma-Aldrich (molecular weight, M_w: 85,000–124,000 g/mol, 99+% hydrolysed). To prepare the base solution, PVA crystals (7 wt.%) were dissolved in deionized (DI) water and stirred under heating until dissolved. The temperature was subsequently reduced to 65 °C, and stirring was continued until the solution became completely transparent. To perform the quaternization at a targeted 2:2:1 molar ratio (GTMAC:KOH:PVA), glycidyltrimethylammonium chloride (GTMAC, Sigma–Aldrich, ≥90% technical grade, calculated based on dry substance) and a 2 M potassium hydroxide (KOH) solution were added to the PVA solution. The resulting mixture was stirred for 4 h at 75 °C. Subsequently, absolute ethanol (Merck, 99.9%) was slowly added to the mixture to precipitate the quaternized PVA (QPVA). The collected precipitate was isolated and dried in a vacuum oven overnight at 60 °C. Finally, the dried QPVA precipitate was redissolved in DI water under continuous stirring to yield the final QPVA solution [15].

2.2 Preparation of cross-linked QPVA/QGO composite membrane

To prepare the 0.5 wt.% quaternized graphene oxide (QGO) filler solution, QGO powder was sonicated in small quantity of DI water until fully dispersed. This step was replicated using to produce the 1.0 wt.% and 2.0 wt.% QGO solutions, respectively. The 0.5 wt.% QGO solution was subsequently mixed with 90 mL of the QPVA solution and sonicated until a completely homogeneous QPVA/QGO casting solution was obtained; this blending procedure was repeated identically for the 1.0 wt.% and 2.0 wt.% QGO variants.

For membrane fabrication, 30 mL of each QPVA/QGO mixture was cast using a doctor blade at a controlled thickness of 50 µm. The cast films were allowed to air-dry on the apparatus until they could be safely peeled off, followed by overnight drying in a vacuum oven at 60 °C. The membranes were then thermally cured in a vacuum oven for 3 h at 80 °C and an additional 1 h at 100 °C. Afterward, the membranes were cut into standardized 2.7 cm × 2.7 cm samples for testing. Chemical cross-linking was carried out by immersing the membranes in a 10 vol.% glutaraldehyde solution (Grade II, 25% in H_2O) prepared in acetone (Merck) for 2 h at room temperature (RT). Finally, the membranes were activated in a 5 M KOH solution for 24 h at 60 °C, followed by equilibration in a 1 M KOH solution for 24 h at room temperature.

2.3 Characterization of QPVA/QGO membranes

2.3.1 Physicochemical Characterizations

Fourier transform infrared (FTIR) spectra of the membrane samples were recorded using a Spectrum 400 FT-IR/NIR Imaging System (PerkinElmer). The spectra of the dried membrane samples were acquired in the wavenumber range of 4000 to 400 cm^{-1} at a resolution of 4 cm^{-1} over 32 scans. X-ray diffraction (XRD) patterns of the samples were obtained using a D8

Advance diffractometer (Bruker) equipped with Cu Kα radiation (1.5406 Å) operated at 40 kV and 40 mA. The scanning 2θ range was set from 5° to 80°, and the collected data were analysed using HighScore Plus software. The surface morphology of the membrane samples was observed via field emission scanning electron microscopy (FESEM) using a MERLIN microscope (ZEISS). All samples were completely dried and sputter-coated with gold prior to measurement. The surface elemental composition of the samples was evaluated using energy-dispersive X-ray spectroscopy (EDX). The dynamic viscosity of the prepared QPVA and QPVA/QGO polymer casting solutions was evaluated at room temperature using a Brookfield DV2T digital rotational viscometer. Measurements were recorded across a range of rotational speeds (5, 10, and 25 rpm) to analyse the rheological behaviour and shear-thinning characteristics of the solutions prior to membrane casting.

2.3.2 Swelling ratio and ionic conductivity

The dry thickness of the QPVA/QGO membranes (t_{dry}) was measured using a micrometer gauge after cross-linking. The corresponding hydrated thickness (t_{wet}) was recorded after the membranes were activated in the KOH solution. The thickness swelling ratio (SR) was then calculated using equation (1):

$$Swelling\ ratio = \frac{t_{wet-} - t_{dry}}{t_{dry}} \quad (1)$$

The ionic conductivity of the QPVA and QPVA/QGO composite membranes was evaluated at room temperature using a standard two-electrode cell configuration connected to an electrochemical workstation (Autolab PGSTAT M204). The membranes were evaluated after immersion in 5 M and 1 M KOH solutions. The bulk membrane resistance (R_s) was determined from the intercept on the real axis of the Nyquist plot, analysed using Nova software. The ionic conductivity (λ) was calculated using equation (2):

$$\lambda = \frac{t}{A \times R_S} \quad (2)$$

where t is membrane thickness (cm), A is the active area of the membrane (cm^2) and R_S is the measured membrane resistance (Ω).

3. Results and discussion

3.1 Chemical and Structural Characterization

Fourier transform infrared (FTIR) analysis was conducted to identify the functional groups present within the QPVA/QGO composite membrane samples. Figure 1 displays the FTIR spectra of the fabricated QPVA/QGO composite membranes. Spectral analysis reveals a noticeable reduction in the intensity of aliphatic C–H bending vibrations following the quaternization and cross-linking of the QPVA/QGO membranes. Compared to pristine QPVA, several new characteristic peaks emerged. Specifically, the peak at 1330 cm^{-1} is attributed to aliphatic C–N stretching, signifying the successful integration of quaternary ammonium groups into the polymer backbone [11]. Furthermore, the prominent absorption band at approximately 1093 cm^{-1} corresponds to C–O–C stretching, which confirms the cross-linking network facilitated by glutaraldehyde (GA) [16]. The presence of peaks at 918 cm^{-1} (epoxy C–O symmetric stretching) and 1413 cm^{-1} (carboxylic O=C–O stretching) further validates the successful incorporation of the QGO component [13]. The appearance of a peak at 1656 cm^{-1} is attributed to C=C stretching within the aromatic structure of QGO, reflecting its hydrophobic domains and their interaction with the QPVA matrix backbone [13, 16]. Additionally, the broad and intense absorption band at 3288 cm^{-1} corresponds to hydroxyl (–OH) stretching vibrations.

Overall, these spectra confirm the existence of functional groups consistent with literature reports, thereby validating the successful synthesis of cross-linked QPVA/QGO composite membranes.

To evaluate how these chemical modifications altered the internal physical architecture of the polymer matrix, X-ray diffraction (XRD) analysis was performed. Figure 2 illustrates the XRD patterns of the QPVA and QPVA/QGO composite membranes across the scanning 2θ range of 5° to 80°. The pristine QPVA membrane exhibits a characteristic prominent crystalline reflection peak at 2θ around 19.5°, corresponding to the semi-crystalline backbone structure of PVA. Upon the incorporation of QGO fillers (0.5, 1.0, and 2.0 wt.%), a slight decrease in the intensity of this primary PVA reflection peak is observed, indicating that the introduction of functionalized QGO nanosheets disrupts the intermolecular hydrogen bonding and close chain packing within the matrix. Furthermore, the peak identified at 2θ = 28.06° is attributed to QGO, reflecting the presence of partially stacked or restacked graphene layers [17]. The low intensity of this peak indicates a highly homogeneous dispersion of QGO within the QPVA matrix, confirming the successful integration of the nanofiller across all composite membranes [11]. The corresponding crystallinity percentages calculated from these diffraction profiles are detailed in Table 1.

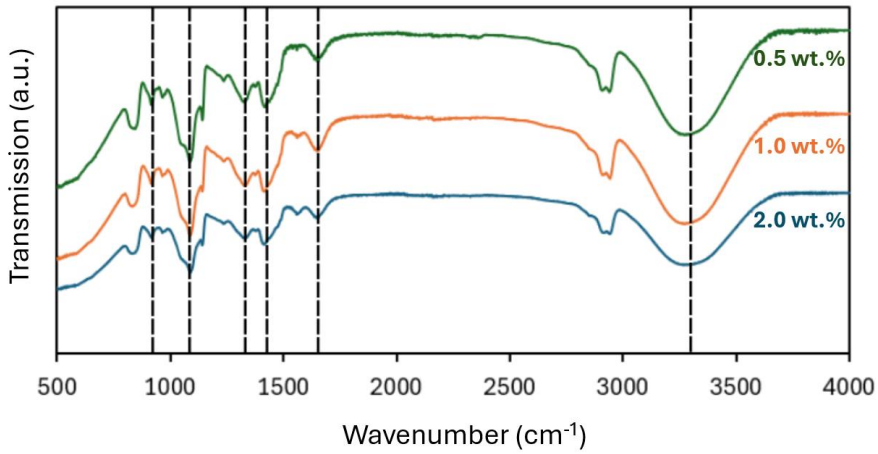

Figure 1: FTIR spectra of QPVA/QGO composite membranes at various QGO filler loadings (0.5 wt.%, 1.0 wt.%, and 2.0 wt.%).

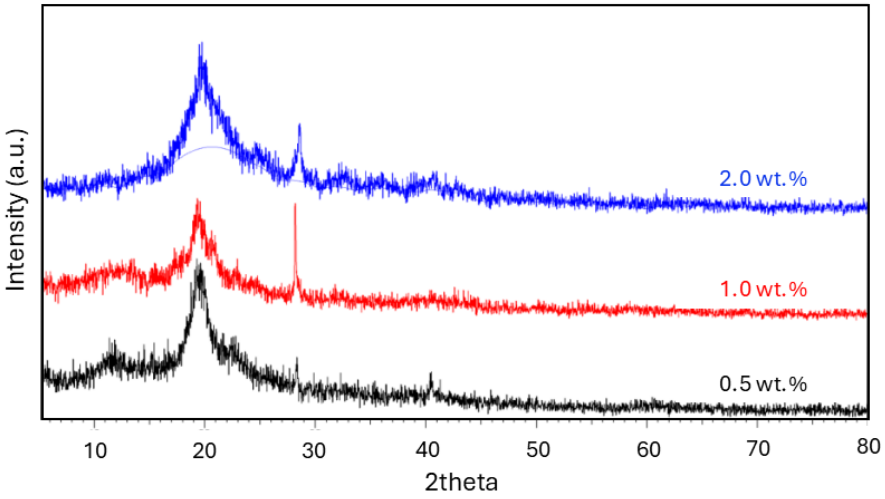

Figure 2: XRD spectra of QPVA/QGO composite membranes at various QGO filler loadings (0.5 wt.%, 1.0 wt.%, and 2.0 wt.%).

Table 1: Calculated crystallinity percentages for QPVA/QGO composite membranes as a function of QGO content.

Membranes	Crystallinity percentage (%)
QPVA/QGO$_{0.5\ wt.\%}$	45.3
QPVA/QGO$_{1.0\ wt.\%}$	31.9
QPVA/QGO$_{2.0\ wt.\%}$	25.8

3.2 Rheological Properties and Surface Properties of the Casting Solutions

The rheological properties of pristine QPVA and QPVA/QGO solutions were evaluated at QGO concentrations of 0.5, 1.0, and 2.0 wt.%. Figure 3 illustrates the dynamic viscosity profiles and rheological behaviour of the QPVA/QGO casting solutions under varying rotational speeds (5, 10, and 25 rpm) as a function of QGO content.

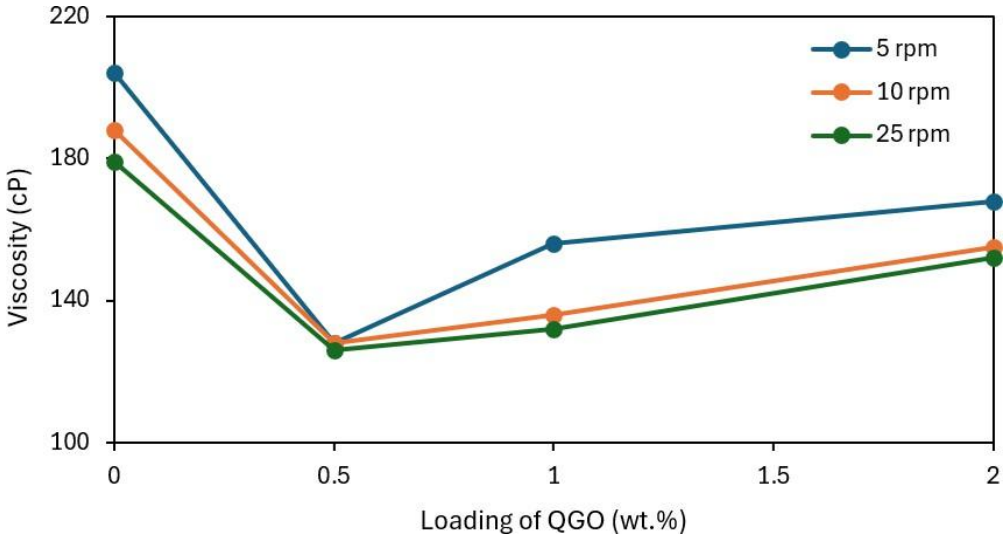

Figure 3: Dynamic viscosity profiles of pristine QPVA and QPVA/QGO composite casting solutions as a function of QGO filler loading under varying rotational speeds (5, 10, and 25 rpm).

Because both the pristine QPVA matrix and the QGO fillers carry positive charges, they exhibit strong electrostatic repulsion at the molecular level. At a low filler concentration of 0.5 wt.%, the highly dispersed QGO nanosheets act as physical barriers that restrict polymer chain entanglement. Consequently, the QPVA chains minimize their interaction with the charged fillers, leading to a reduction in hydrodynamic volume and a subsequent decrease in fluid resistance [18]. This phenomenon induces the formation of highly localized, low-friction shearing planes, resulting in a precipitous reduction in macro-viscosity compared to pristine QPVA. However, increasing the QGO concentration to 1.0 wt.% and 2.0 wt.% occupies the available free volume within the polymer matrix, driving the composite solution into a critical crowding threshold. Despite the persistent electrostatic repulsion between the QPVA chains and QGO fillers, the high packing density significantly restricts molecular mobility, which shifts the viscosity upward [19, 20]. Across all samples, the viscosity decreases as the rotational speed increases from 5 to 25 rpm, demonstrating characteristic non-Newtonian, shear-thinning (pseudoplastic) behaviour. Controlling this solution viscosity is crucial for the doctor blade casting method, as the shear forces applied during the sliding motion of the blade dictate the uniformity of the film and prevent uneven dispersion.

To complement the rheological evaluation, an analysis of the surface tension and contact angle was conducted for the QPVA/QGO solutions with varying QGO loadings. The resulting data are summarized in Table 3, while Figure 4 illustrates the droplet morphology and corresponding contact angles for each loading condition.

Table 3: Surface tension and water contact angle of QPVA/QGO composite casting solutions

QGO loading(wt.%)	Surface tension (mN/m)	Contact angle (°)
0.5	72.33±1.33	40.51±0.32
1.0	66.84±0.93	52.66±1.27
2.0	65.90±0.34	32.69±0.37

As shown by the contact angle trends in Figure 4, the 1.0 wt.% QGO loading yielded the highest contact angle 52.66° compared to the 0.5 wt.% and 2.0 wt.% concentrations, indicating a localized minimum in surface hydrophilicity [21]. Generally, increased QGO loading introduces a higher surface concentration of mobile quaternary ammonium groups, which typically enhances hydrophilicity and drives down the contact angle, as observed in the sharp decrease to32.69° at 2.0 wt.%. However, the 1.0 wt.% threshold represents an anomalous optimal loading point where the QGO is perfectly and uniformly dispersed within the polymer matrix, as corroborated by subsequent FESEM observations. In contrast, the 0.5 wt.% loading exhibited a lower contact angle (40.51°) despite possessing a higher surface tension (72.33 mN/m), which is likely due to insufficient filler coverage that leaves patches of the base QPVA matrix exposed [22]. These findings suggest that surface roughness, interfacial energy, and filler dispersion quality are the primary determinants of the membrane's wetting behaviour. Ultimately, the surface tension, contact angle, and viscosity play a collective role during doctor blade casting, as they govern the cohesion of the polymer solution and its wetting interactions with the casting substrate (such as glass or PET) to ensure defect-free membranes.

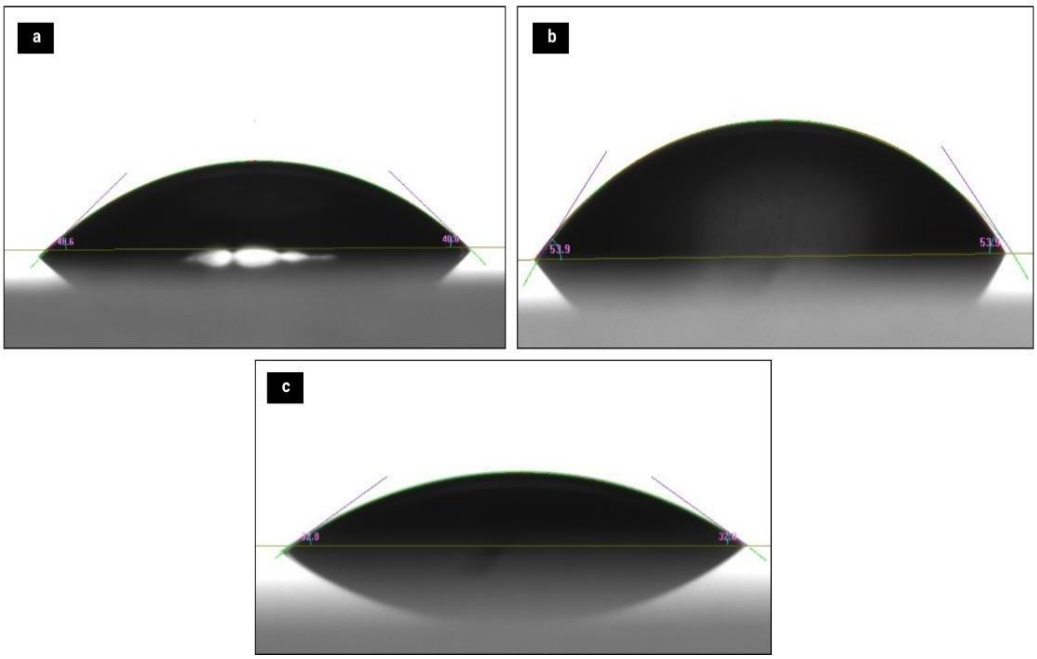

Figure 4: Water contact angle profiles and droplet shapes of QPVA/QGO composite membranes with 0.5 wt.%, 1.0 wt.%, and 2.0 wt.% QGO loadings.

3.3 Morphological and Elemental Analysis

The surface morphology and elemental composition of the QPVA/QGO membranes were characterized using field emission scanning electron microscopy (FESEM) coupled with energy-dispersive X-ray spectroscopy (EDX). This analysis provided a comprehensive assessment of the surface topology and elemental distribution across the designated membrane areas. FESEM micrographs captured at 1000× magnification, alongside the corresponding EDX mappings for all samples, are presented in Figure 5.

Based on Figures 5a–c (most right panels), the membrane surface contrast darkens as the filler loading within the polymer matrix increases. Furthermore, based on table 5 shows QPVA/QGO composite membranes yield controlled thickness between 47 – 49 µm. The QPVA/QGO membrane integrated with 1.0 wt.% QGO displays a highly uniform morphology, indicating a homogeneous dispersion of the nanofiller within the polymer matrix (Figure 5e). In contrast, increasing the QGO loading to 2.0 wt.% results in observable filler agglomeration (Figure 5f). This high weight percentage compromises dispersion quality, leading to an excessive filler density that obstructs the ion transport pathways of the host QPVA polymer [11, 23].

EDX mapping of the QPVA/QGO composite membranes identifies the constituent elements as carbon (C), oxygen (O), potassium (K), and chlorine (Cl). Visual analysis confirms a uniform elemental distribution throughout the composite matrix, with carbon emerging as the dominant element. Notably, the relative oxygen content within the matrix increases in direct correlation with the higher wt.% filler loading due to the oxygen-rich functional groups on the QGO. Concurrently, a substantial reduction in the relative chlorine elemental composition is observed, dropping from 15.7% to 0.6%. This reduction is primarily attributed to the increased concentration of QGO per unit area, suggesting that the dense network and structural interactions within the QPVA/QGO matrix effectively displace or dilute the chlorine content within the scanned framework. Ultimately, FESEM and EDX mapping provide a comprehensive characterization of the morphology, packing density, and elemental distribution within the composite structure, with detailed values summarized in Table 4.

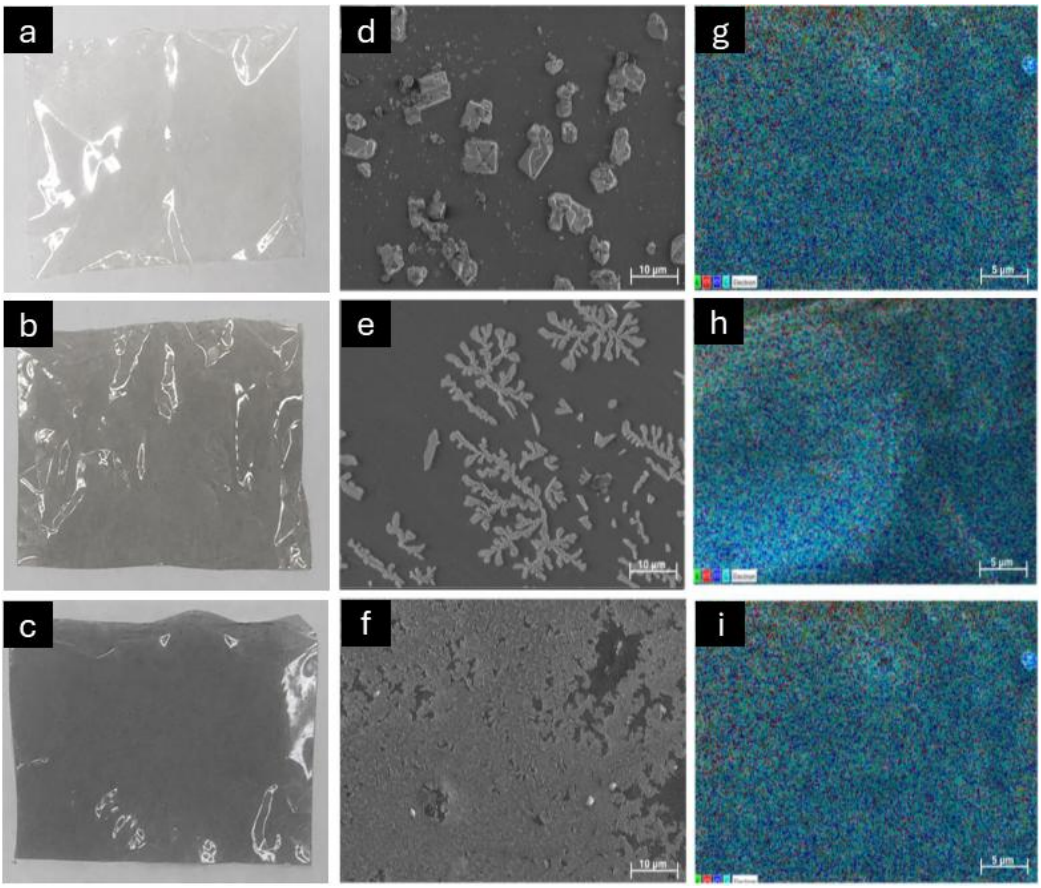

Figure 5: (a – c) Raw image of QPVA/QGO membranes, (d – f) FESEM morphology and (g – i) EDX mapping of the membranes with QGO wt.% loading of 0.5 wt.%, 1.0 wt.% & 2.0 wt.% respectively

Table 4: Elemental compositions of QPVA/QGO membrane

	Composition of Elements (%)		
Elements	**QPVA/QGO$_{0.5\ wt.\%}$**	**QPVA/QGO$_{1.0\ wt.\%}$**	**QPVA/QGO$_{2.0\ wt.\%}$**
Carbon	55.3	67.7	68.4
Oxygen	12.7	28.4	29.6
Potassium	16.3	2.4	1.4
Chlorine	15.7	1.5	0.6

3.4 Swelling Ratio and Ion Conductivity

Table 5 demonstrates that the incorporation of QGO fillers and subsequent alkaline treatment conditions exert a profound dual influence on the dimensional stability and electrochemical properties of the fabricated AEMs. A distinct and contrasting trend in both thickness swelling and ionic conductivity is observed when comparing the membranes immediately after activation in a highly concentrated 5.0 M KOH solution versus after equilibration in a lower-concentration 1.0 M KOH solution.

Table 5: Swelling ratio and ion conductivity

Membranes	Dry thickness(μm)	Activation of membranes in 5M KOH		Equilibration of membranes in 1M KOH	
		Thickness swelling (%)	Ion conductivity (mS/cm)	Thickness swelling (%)	Ion conductivity (mS/cm)
QPVA	49.22± 3.60	23.75±4.96	4.09±0.30	11.25±1.40	4.69 ±0.56
QPVA/QGO$_{0.5}$ wt.%	48.56 ± 7.27	11.50 ± 4.42	5.45 ± 0.99	8.19 ± 4.14	5.60 ± 0.55
QPVA/QGO$_{1.0}$ wt.%	48.33 ± 2.52	41.46 ± 4.29	7.74 ± 1.65	4.88 ± 3.82	10.79 ± 3.32
QPVA/QGO$_{2.0}$ wt.%	47.11 ± 1.92	8.29 ± 2.25	2.95 ± 0.60	8.92± 6.44	4.47±0.46

During the initial activation phase in 5.0 M KOH, the QPVA/QGO 1.0 wt.% membrane exhibits an exceptionally high thickness swelling ratio of 41.46%, which is accompanied by an ionic conductivity of 7.74 mS/cm. This significant spike in swelling is dictated by thermodynamic and osmotic phenomena. Because the 1.0 wt.% loading provides an optimal and highly uniform distribution of quaternary ammonium functional groups across both the QPVA matrix and the QGO nanosheets, it creates a high density of accessible hydrophilic ionic domains. When immersed in a highly concentrated 5.0 M KOH solution, an immense osmotic pressure gradient is generated between the external electrolyte and the membrane interior, drawing a massive influx of OH^- and K^+ ions into these domains. This intense ion crowding triggers severe electrostatic repulsion among the closely packed ions within the hydrophilic channels, forcing the polymer chains to stretch extensively and resulting in a severe swelling profile. In sharp contrast, when the 1.0 wt.% membrane is subsequently transferred and allowed to equilibrate in a milder 1.0 M KOH environment, a dramatic structural recovery occurs. The thickness swelling ratio plummets to a minimum of 4.88%, while its ionic conductivity simultaneously surges to a peak value of 10.79 mS/cm. This behavioural shift aligns with the principles established by Zakaria et al. [11], demonstrating that optimal filler loading can successfully modulate swelling and maximize conductivity under standardized operational conditions. The mechanism behind this improvement during 1.0 M KOH equilibration can be explained by structural deswelling and channel optimization, as illustrated by the structural relationship between hydration and ion hopping.

When the external alkaline concentration drops from 5.0 M to 1.0 M, the severe internal osmotic pressure is relieved, causing excess unbound free-alkali ions to diffuse out of the membrane. This concentration reduction allows the elastic contractile forces of the glutaraldehyde (GA) cross-linked polymer network to reassert control, pulling the expanded matrix back into a structurally stabilized, low-swelling state (4.88%). Crucially, this moderate hydration state works in perfect synergy with the membrane's microstructural architecture. As established in the FESEM analysis (Section 3.3), the 1.0 wt.% QGO composite exhibits a highly homogeneous morphology, characterized by a uniform distribution of the functionalized nanofiller throughout the host polymer matrix. This structural consistency ensures that during matrix contraction upon equilibration, the continuous network of interconnected hydrophilic pathways remains intact without collapsing or fragmenting. Free from the severe

macrostructural tortuosity and phase separation that typically hinders ion migration, the localized quaternary ammonium sites achieve an optimized spatial arrangement. Instead, the well-dispersed QGO nanosheets remain perfectly aligned to form continuous, uninterrupted ionic highways across the membrane profile. This allows the hydroxide (OH^-) ions to migrate with improved efficiency, driving the conductivity up to its peak value of 10.79 mS/cm.

A highly intriguing and reversed trend is observed for the over-loaded 2.0 wt.% QGO composite membrane, where both thickness swelling and ionic conductivity increase when moving from 5.0 M KOH to 1.0 M KOH. In the highly concentrated 5.0 M KOH activation solution, the extreme ionic strength of the external environment creates a hypertonic osmotic effect that essentially dehydrates the membrane. Because the 2.0 wt.% sample suffers from severe nanoparticle agglomeration, its polymer network is highly phase-separated and rigid, restricting water uptake to just 8.29%. This lack of internal water molecules deprives the system of the hydration required for ion transport, resulting in a severely restricted baseline conductivity of 2.95 mS/cm. However, when transferred to the lower-concentration 1.0 M KOH solution, the external osmotic pressure drops significantly, allowing water to readily penetrate the membrane matrix. For this over-loaded sample, the accumulated water molecules pool inside the loose interfacial micro voids and cracks caused by the QGO agglomerates [24, 25]. This hydration influx causes the thickness swelling to rise from 8.29% to 8.92%. Crucially, this additional water presence helps re-hydrate the remaining functional pathways and facilitates greater liquid-phase ion mobility, which explains the corresponding rise in ionic conductivity from 2.95 mS/cm to 4.47 mS/cm.

Despite this localized improvement, the conductivity of the 2.0 wt.% membrane remains drastically lower than that of the optimized 1.0 wt.% sample (10.79 mS/cm) because the agglomerated clusters permanently block continuous, long-range anion transport channels. Ultimately, a comparative analysis across both chemical environments confirms that the 1.0 wt.% QGO loading represents a definitive performance threshold. This configuration leverages the transition between activation and equilibration to yield improved dimensional stability and peak electrochemical performance, as visually summarized by the direct correlation plotted in Figure 6.

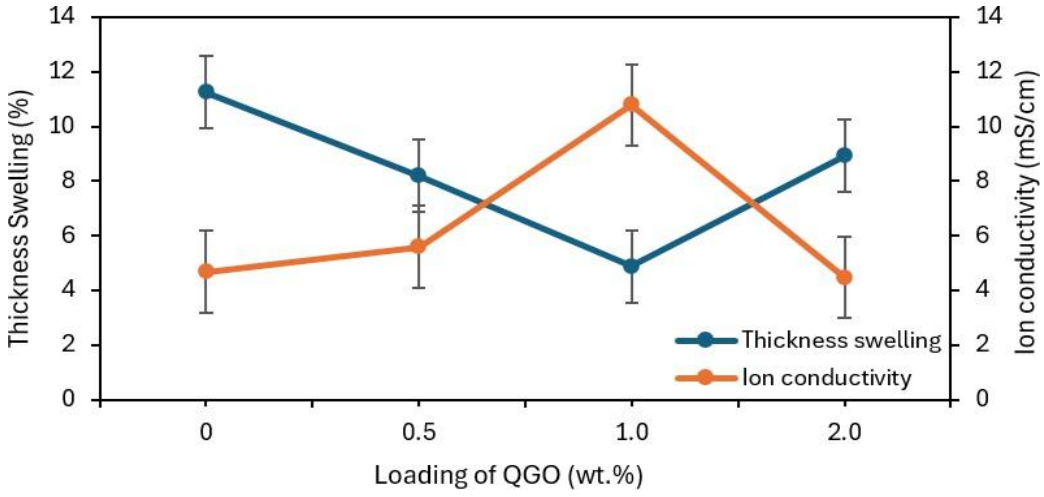

Figure 6: Graph of swelling ratio and ion conductivity at 1 M KOH against QGO loading

Conclusion

In conclusion, this study successfully fabricated uniform quaternized polyvinyl alcohol and quaternized graphene oxide (QPVA/QGO) composite membranes utilizing the doctor blade casting technique for anion exchange membrane water electrolysis. Characterization via FTIR, XRD, and FESEM-EDX confirmed successful chemical functionalization and revealed that a 1.0 wt.% QGO loading yields a homogeneous filler dispersion, whereas a higher loading of 2.0 wt.% induces particle agglomeration. Dimensional and electrochemical evaluations proved that the 1.0 wt.% QGO concentration represents the optimal loading point, achieving a minimized thickness swelling of 4.88% and a peak ionic conductivity of 10.79 mS/cm after equilibration in 1.0 M KOH. Overall, this work demonstrates that the combination of polymer quaternization, optimized nanofiller loading, and controlled doctor blade casting offers a viable approach to producing structurally stable composite membranes for efficient green hydrogen production.

Acknowledgment

The authors gratefully acknowledge the financial support provided by the Ministry of Higher Education Malaysia through the Higher Education Centre of Excellence (HICoE) Program awarded to the Fuel Cell Institute, Universiti Kebangsaan Malaysia (Grant No. HICOE-2023-004).

Author Contributions

The authors declare that they contributed equally to all stages of this manuscript and research.

Declaration of Competing Interest

The authors declare that they have no known competing financial interests or personal relationships that could have appeared to influence the work reported in this paper.

Declaration of Generative AI and AI-Assisted Technologies in the Writing Process

During the preparation of this manuscript, the authors utilized Gemini Pro AI strictly for grammatical editing, proofreading, and language enhancement to improve text readability. The AI assistance was limited to refining sentence structures and phrasing, with no role in experimental data generation, data analysis, or the formulation of scientific conclusions. The authors have thoroughly reviewed and verified the final text and accept full responsibility for the accuracy, integrity, and authenticity of the content presented in this work.

References

1. Vincent, I., E.-C. Lee, and H.-M. Kim, *Comprehensive impedance investigation of low-cost anion exchange membrane electrolysis for large-scale hydrogen production.* Scientific Reports, 2021. **11**(1): p. 293.

2. Liu, L., et al., *Recent Advances and Challenges in Anion Exchange Membranes Development/Application for Water Electrolysis: A Review.* Membranes (Basel), 2024. **14**(4).
3. Noor Azam, A.M.I., et al., *Investigation of Performance of Anion Exchange Membrane (AEM) Electrolysis with Different Operating Conditions.* Polymers (Basel), 2023. **15**(5).
4. Samsudin, A.M., M. Bodner, and V. Hacker, *A Brief Review of Poly(Vinyl Alcohol)-Based Anion Exchange Membranes for Alkaline Fuel Cells.* Polymers (Basel), 2022. **14**(17).
5. Zakaria, Z. and S.K. Kamarudin, *A review of quaternized polyvinyl alcohol as an alternative polymeric membrane in DMFCs and DEFCs.* International Journal of Energy Research, 2020. **44**: p. 6223 - 6239.
6. Samsudin, A.M., et al., *Preparation and Characterization of QPVA/PDDA Electrospun Nanofiber Anion Exchange Membranes for Alkaline Fuel Cells.* Nanomaterials (Basel), 2022. **12**(22).
7. Zakaria, Z. and S.K. Kamarudin, *Evaluation of Quaternized polyvinyl alcohol/graphene oxide-based membrane towards improving the performance of air-breathing passive direct methanol fuel cells.* International Journal of Energy Research, 2020. **44**(11): p. 8988-9000.
8. Samsudin, A.M. and V. Hacker, *Effect of Crosslinking on the Properties of QPVA/PDDA Anion Exchange Membranes for Fuel Cells Application.* Journal of The Electrochemical Society, 2021. **168**(4).
9. Dennis, J.O., et al., *A Review of Current Trends on Polyvinyl Alcohol (PVA)-Based Solid Polymer Electrolytes.* Molecules, 2023. **28**(4).
10. Choudhury, R.R., J.M. Gohil, and K. Dutta, *Poly(vinyl alcohol)-based membranes for fuel cell and water treatment applications: A review on recent advancements.* Polymers for Advanced Technologies, 2021. **32**(11): p. 4175-4203.
11. Zakaria, Z., S.K. Kamarudin, and S.N. Timmiati, *Influence of Graphene Oxide on the Ethanol Permeability and Ionic Conductivity of QPVA-Based Membrane in Passive Alkaline Direct Ethanol Fuel Cells.* Nanoscale Res Lett, 2019. **14**(1): p. 28.
12. Kleut, D. and J. Prekodravac Filipovic, *Advances in Graphene Oxide-Based Composites and Membranes: Structural Engineering, Multifunctional Performance, and Emerging Applications.* Processes, 2025. **14**(1).
13. Zarrin, H., et al., *Quaternized Graphene Oxide Nanocomposites as Fast Hydroxide Conductors.* ACS Nano, 2015. **9**(2): p. 2028-2037.
14. Dyartanti, E.R., et al., *Recent Development of Polyvinylidene Fluoride/Cellulose Membranes Electrolyte Separator for Lithium Ion Batteries.* IOP Conference Series: Materials Science and Engineering, 2021. **1096**(1): p. 012144.
15. Ng, W.K., et al., *The impact of double crosslinking and alkaline activation strategies on the multifaceted characteristics of quaternized poly(vinyl alcohol) anion exchange membranes.* Energy Advances, 2025. **4**(3): p. 400-413.
16. Shaari, N., S.K. Kamarudin, and Z. Zakaria, *Enhanced alkaline stability and performance of alkali-doped quaternized poly(vinyl alcohol) membranes for passive direct ethanol fuel cell.* International Journal of Energy Research, 2019. **43**(10): p. 5252-5265.
17. Gupta, B., et al., *Role of oxygen functional groups in reduced graphene oxide for lubrication.* Sci Rep, 2017. **7**: p. 45030.
18. Kopac, T., A. Rucigaj, and M. Krajnc, *Effect of polymer-polymer interactions on the flow behavior of some polysaccharide-based hydrogel blends.* Carbohydr Polym, 2022. **287**: p. 119352.
19. Ghannam, M.T., et al., *Viscosity Characteristics of Cationic Polyacrylamide Aqueous Solutions.* Polymers (Basel), 2026. **18**(3).

20. Hu, J., et al., *Main Controlling Factors Affecting the Viscosity of Polymer Solution due to the Influence of Polymerized Cations in High-Salt Oilfield Wastewater.* Processes, 2024. **12**(4).
21. Brack, H., *A contact angle investigation of the surface properties of selected proton-conducting radiation-grafted membranes.* Journal of Membrane Science, 2003. **214**(1): p. 1-19.
22. Zhang, Q., et al., *Structural and Transport Properties of Hydrophilic and Hydrophobic Modified Ionomers in Proton Exchange Membrane Fuel Cells.* Polymers (Basel), 2024. **16**(5).
23. Kumar, S.R., et al., *Synergistic role of graphene oxide-magnetite nanofillers contribution on ionic conductivity and permeability for polybenzimidazole membrane electrolytes.* Journal of Power Sources, 2020. **445**.
24. Hasan, M.R. and J. Coronas, *How Can the Filler-Polymer Interaction in Mixed Matrix Membranes Be Enhanced?* Chempluschem, 2024. **89**(12): p. e202400456.
25. Sardarabadi, H., et al., *Effect of Nanofillers on Properties and Pervaporation Performance of Nanocomposite Membranes: A Review.* Membranes (Basel), 2022. **12**(12).

Malaysian Journal of Energy and Applications 1(2026): 71-83
https://doi.org/10.17576/myjea.2026.01.71

DYNAMIC TEMPERATURE-DEPENDENT SIMULATION OF A 400-CELL PROTON EXCHANGE MEMBRANE FUEL CELL STACK USING MATLAB-SIMSCAPE

Wan Ahmad Saffuan bin Wan Mohamed Salleh[1] & Sahriah Basri[1]*

[1]*Fuel Cell Institute, Universiti Kebangsaan Malaysia, 43600 Bangi, Selangor, Malaysia*

**Corresponding author: sahriah@ukm.edu.my*

Received 2/7/2026; Received in Revised Form 16/7/2026;
Accepted 16/7/2026; Available Online 20/07/2026.

Abstract

Proton exchange membrane fuel cells (PEMFCs) are promising clean energy converters for stationary and mobility applications, but their performance is strongly governed by thermal and water balance under dynamic load operation. This study extends a previously developed thesis model into a journal-level dynamic assessment by introducing four clearly defined inlet-temperature cases (40, 50, 60 and 70 °C), applying an identical transient load profile to every case, consolidating electrochemical and balance-of-plant outputs, and evaluating the resulting operating window using coupled performance, thermal, water-production and hydrogen-consumption criteria. The model represents a 400-cell PEMFC stack with an active area of 280 cm2 per cell and a constant hydrogen supply pressure of 70 MPa. Model credibility was examined through physical-consistency checks and comparison of the predicted trends with established PEMFC behaviour reported in the literature. Increasing inlet temperature improved high-current polarization response and power stability, with 70 °C producing the strongest high-current tolerance. However, this benefit was accompanied by greater thermal stress: although all cases approached a quasi-steady stack temperature of approximately 353 K, the peak stack temperature increased from 353 K at 40 °C to 364 K at 70 °C. Dynamic current density reached approximately 0.95 A cm-2, heat generation peaked at about 37-40 kW, water production reached about 10 g s-1 and hydrogen consumption reached about 1.1 g s-1 during peak demand. The results identify 60-70 °C as the most practical operating range, with 60 °C providing the more conservative balance between performance and thermal margin. Experimental validation remains necessary before the model is used for quantitative design or control-system certification.

Keywords: PEMFC; MATLAB-Simscape; dynamic load; operating temperature; hydrogen consumption; thermal management; water management

1. Introduction

Proton exchange membrane fuel cells (PEMFCs) are among the most mature electrochemical energy conversion technologies for hydrogen-based power generation. Their low operating temperature, fast start-up, relatively high power density and zero local emission profile make them attractive for clean transport, backup power, distributed generation and renewable energy integration [1,2]. Despite these advantages, reliable PEMFC deployment is still constrained by coupled electrochemical, thermal and mass-transport limitations. Temperature is one of the most influential operating variables because it affects electrode kinetics, proton conductivity, membrane hydration, reactant transport, water removal and component degradation.

In a PEMFC, hydrogen oxidation occurs at the anode and oxygen reduction occurs at the cathode. The membrane must remain sufficiently hydrated to transport protons effectively, while gas diffusion layers and flow channels must remove product water without starving the

catalyst layer of reactants. Under low-temperature operation, reaction kinetics can be slower and water accumulation may lead to flooding. At excessively high temperature, improved kinetics may be offset by membrane dehydration, increased ohmic resistance and accelerated material degradation [3-5]. Therefore, the optimum temperature cannot be defined only by the highest power output; it must also consider thermal stability, water balance and fuel utilisation.

Many PEMFC studies use steady-state polarization curves to compare performance. However, practical fuel-cell systems rarely operate at a constant load. Applications such as vehicles, portable power systems and grid-support devices experience repeated load fluctuations, which cause transient changes in current density, voltage, heat generation, hydrogen consumption and water production. These dynamic effects are important for sizing the cooling system, humidifier, hydrogen supply and control strategy. Simulation platforms such as MATLAB-Simscape are useful because they allow rapid evaluation of the system-level response before experimental prototyping, reducing cost and enabling safer operating-window exploration [6-8].

The present paper extends the earlier thesis model in four specific ways. First, it replaces the broad thesis-level reporting of numerous individual outputs with a controlled four-temperature comparison under one identical dynamic load cycle. Second, it integrates polarization, voltage, current density, stack temperature, heat generation, water production and hydrogen consumption in a single coupled assessment rather than interpreting these outputs separately. Third, it evaluates the temperature range against a practical operating-window criterion that considers both power response and balance-of-plant requirements. Fourth, it adds an explicit model-credibility assessment based on governing physical relationships, internal consistency and comparison with published PEMFC trends. The objective is to determine the most suitable inlet-temperature range for a 400-cell PEMFC stack under dynamic load and to clarify the implications for cooling, humidification, reactant supply and future experimental validation.

2. Model Configuration and Simulation Method

A system-level PEMFC stack model was implemented in MATLAB-Simscape. The model included the hydrogen source, oxygen source, anode and cathode gas channels, anode and cathode humidifiers, exhaust subsystems, recirculation path, cooling system, membrane electrode assembly and electrical load. The membrane electrode assembly block represented a 400-cell stack with an active area of 280 cm2 per cell. The principal independent variable was the inlet temperature, set at 40, 50, 60 and 70 °C. Although conventional low-temperature PEMFC stacks are commonly operated within approximately 60-80 °C, the lower 40 and 50 °C cases were retained as diagnostic boundary conditions. They allow the model to quantify the penalty associated with sub-optimal cold operation and to distinguish kinetic and water-management effects before the stack reaches its normal operating range. The hydrogen supply pressure was kept constant at 70 MPa to isolate the effect of temperature within the configured system.

The same dynamic load profile, simulation duration, initial conditions and balance-of-plant settings were applied to all four temperature cases. Recorded variables were stack voltage, stack temperature, current density, heat generated or dissipated, electrical power, water production and hydrogen consumption. Polarization and power-density curves were used to assess electrochemical response, while time-domain outputs were used to evaluate transient stability and the severity of thermal, water and reactant-supply requirements. Unlike the thesis, which presented a wider collection of model outputs, the present analysis uses a common

comparison framework and focuses only on variables that directly support operating-window selection.

2.1 Improvements relative to the thesis model

The underlying stack architecture remains based on the thesis model, but the journal version improves the analysis and interpretation rather than claiming a completely new electrochemical formulation. The principal improvements are: (i) a controlled temperature-sweep design using identical dynamic inputs; (ii) simultaneous interpretation of electrochemical, thermal and mass-balance outputs; (iii) direct comparison of 40-70 °C to identify the transition from cold, kinetically limited operation to the conventional PEMFC operating range; and (iv) an engineering decision framework that distinguishes a high-performance set point from a conservative durability-oriented set point. These additions convert the thesis model from a general simulation platform into a focused operating-window study.

2.2 Model verification and validation approach

Model verification was performed through three levels of consistency checking. First, the predicted polarization response was examined for the expected sequence of activation, ohmic and mass-transport losses. Second, the dynamic outputs were checked for physical coupling: increases in current demand had to coincide with lower voltage, higher heat generation, greater hydrogen consumption and greater product-water formation. Third, the temperature trends were compared qualitatively with established PEMFC theory and published studies, which generally report improved reaction kinetics and voltage retention as temperature rises toward the normal 60-80 °C operating range, subject to adequate membrane hydration [4,12-15]. The simulated peak current density of approximately 0.95 A cm^{-2} and the observed improvement from 40 to 70 °C are therefore physically plausible. However, these checks constitute trend-level validation only. Because matched experimental data for the same 400-cell stack and dynamic load cycle were not available, the model should not yet be treated as quantitatively validated as shown in Table 1. This distinction is retained throughout the discussion and defines the present limits of model use.

Table 1. Summary of PEMFC stack model and simulation variables.

Parameter	Value used in simulation	Purpose in analysis
Number of cells	400	Stack-level voltage and power evaluation
Active area per cell	280 cm2	Current-density and power-density assessment
Hydrogen supply pressure	70 MPa	Kept constant to isolate temperature effect
Inlet temperature	40, 50, 60 and 70 °C	Main independent variable
Recorded outputs	Voltage, current density, power, heat, water and H2 use	Dynamic performance and system sizing
Software platform	MATLAB-Simscape	Physics-based system simulation

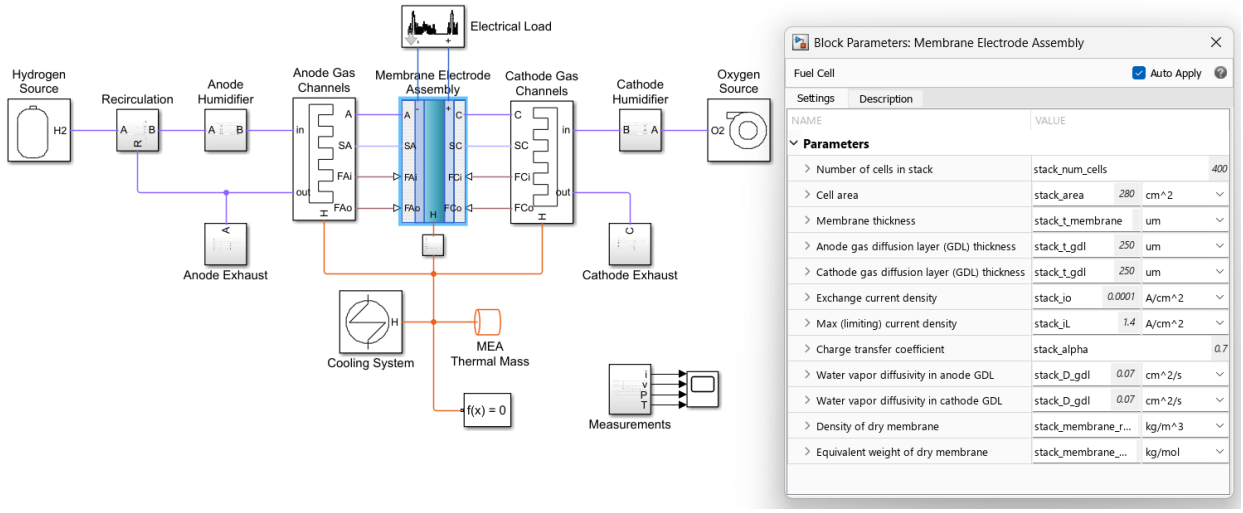

Figure 1. MATLAB-Simscape PEMFC stack configuration used in the simulation, showing the hydrogen and oxygen supply paths, gas channels, humidifiers, MEA, cooling system and measurement ports.

The polarization curves show the expected PEMFC behaviour: cell voltage decreased as current density increased, reflecting activation losses at low current density, ohmic losses at intermediate current density and mass-transport limitations at high current density. The 40 and 50 °C cases represent sub-optimal cold-operation conditions relative to the commonly used 60-80 °C PEMFC range. Their inclusion is useful because it demonstrates the performance penalty before the stack reaches its normal thermal window. The 40 °C case gave the weakest high-current response because lower temperature reduces electrode-reaction rates and membrane proton conductivity. Increasing the inlet temperature improved the high-current region as oxygen-reduction kinetics and proton transport became more favourable.

The 70 °C case provided the best high-current tolerance, with a more gradual voltage decline and the broadest power-density region. This result is consistent with improved catalyst-layer reaction kinetics and lower effective electrochemical losses at 70 °C compared with the lower-temperature cases; it should not be interpreted as evidence that catalyst activity alone determines the optimum. The 60 °C case also showed substantially better behaviour than 40 and 50 °C and remained within the conventional PEMFC operating range. Thus, the useful range is 60-70 °C rather than a single optimum point. The upper end provides stronger power response, whereas the lower end offers a larger thermal and hydration safety margin.

3. Results and Discussion

3.1 Polarization and power-density response

The polarization curves show the expected PEMFC behaviour: cell voltage decreased as current density increased. This trend reflects the transition from activation losses at low current density to ohmic losses at intermediate current density and mass-transport limitations at high current density. The 40 °C case gave the weakest high-current response because lower temperature reduces reaction kinetics and increases the effective resistance associated with proton transport. Increasing the inlet temperature improved the high-current region because the electrochemical reactions became more favourable and membrane conductivity was enhanced.

The 70 °C case provided the best high-current tolerance, with a more gradual voltage decline and the broadest power-density region. The 60 °C case also showed improved

behaviour compared with 40 and 50 °C, suggesting that the useful temperature window is not a single point but a range. The important engineering implication is that operating at 60-70 °C can improve the available current and power under dynamic demand, but the upper part of this range requires strict humidification and cooling control to avoid dehydration.

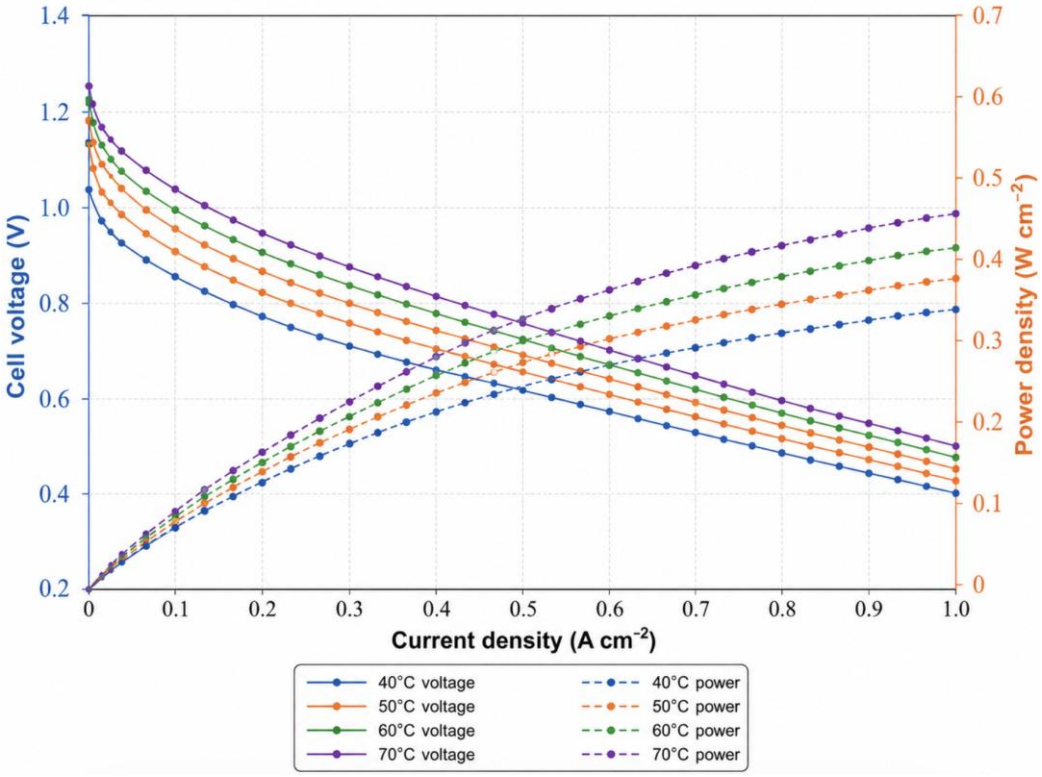

Figure 2. Comparative I-V and power-density behaviour for inlet temperatures of 40, 50, 60 and 70 °C.

A limitation of this temperature comparison is that the model uses lumped stack temperature and prescribed component parameters. It therefore cannot resolve local hot spots, cell-to-cell temperature variation, membrane dry-out fronts or spatial water accumulation. Consequently, the predicted 364 K peak should be interpreted as a system-level warning indicator rather than a local maximum temperature for every cell.

Table 2. Condensed comparison of key performance indicators from the dynamic PEMFC simulations.

Metric	40 °C	50 °C	60 °C	70 °C
Polarization response	Lowest high-current tolerance	Moderate improvement	Better voltage retention	Best high-current response
Steady stack temperature	353 K	353 K	353 K	353 K
Peak stack temperature	353 K	355 K	357 K	364 K
Dynamic current-density peak	~0.95 A cm-2	~0.95 A cm-2	~0.95 A cm-2	~0.95 A cm-2
Heat-generation peak	37-40 kW range	37-40 kW range	37-40 kW range	37-40 kW range
Water-production peak	Up to ~10 g s-1	Up to ~10 g s-1	Up to ~10 g s-1	Up to ~10 g s-1

Hydrogen-consumption peak	Up to ~1.1 g s-1	Up to ~1.1 g s-1	Up to ~1.1 g s-1	Up to ~1.1 g s-1
Overall interpretation	Stable but lower performance	Intermediate	Recommended balance	Highest output but highest thermal risk

3.2 Dynamic temperature behaviour

The stack temperature increased rapidly from the inlet value during the early transient period because PEMFC reactions are exothermic and internal losses produce heat. The temperature response generally reached a quasi-steady level after approximately 300-500 s, followed by small oscillations associated with load variation and thermal dynamics. The important finding is that all inlet-temperature cases converged to a steady stack temperature of approximately 353 K, equivalent to about 80 °C. This indicates that the cooling system and stack thermal mass drove the system toward a similar nominal operating temperature.

However, the peak temperature increased systematically with inlet temperature. The 40 °C case peaked at 353 K, whereas the 70 °C case reached 364 K. This 11 K increase is important because PEMFC membranes and catalyst layers are sensitive to hydration loss and thermal degradation. While higher temperature improves kinetics, the observed peak at 70 °C indicates that cooling-system capacity and humidifier control must be designed for transient peaks rather than only steady-state temperature.

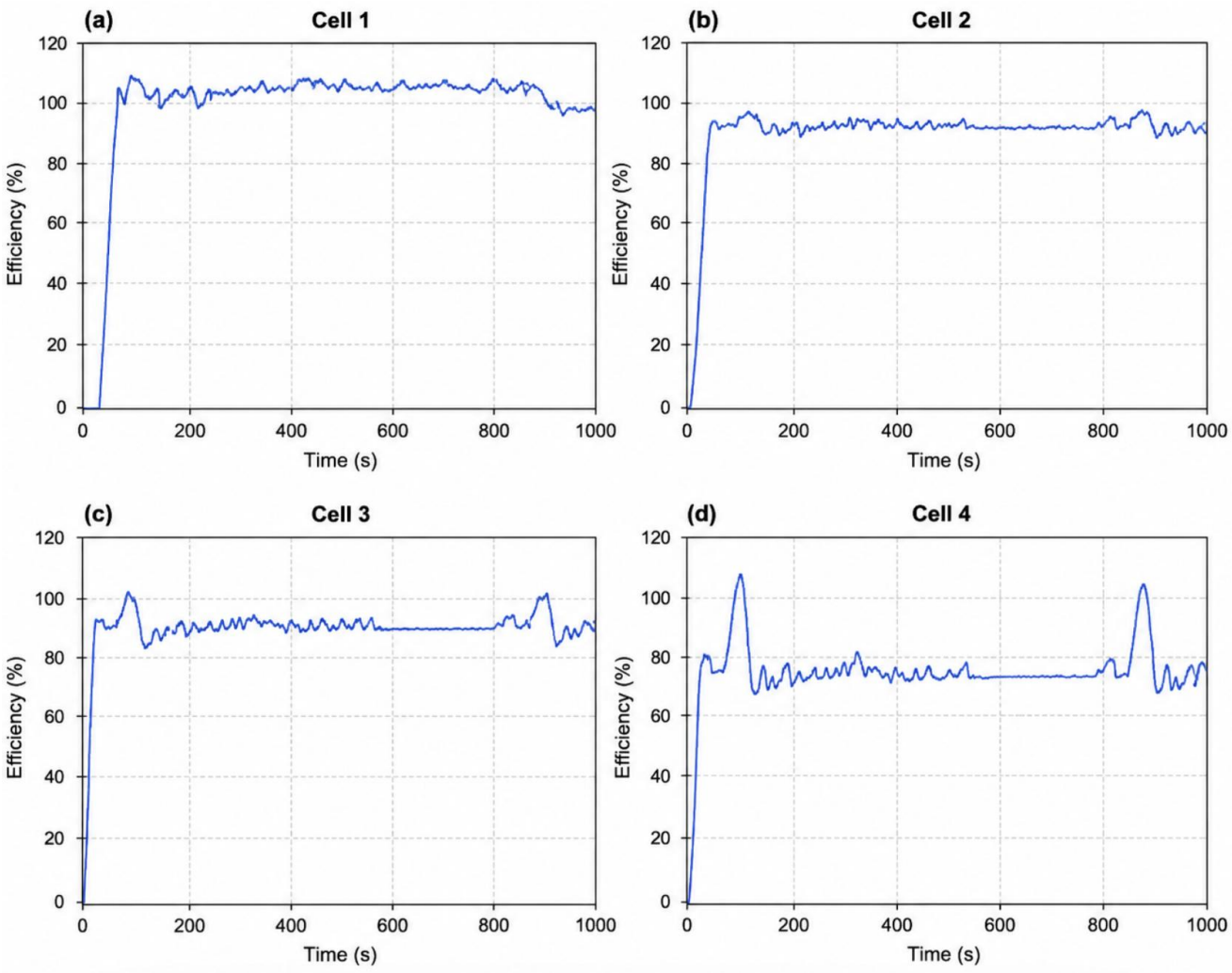

Figure 3. Dynamic stack-temperature response for all inlet-temperature cases. The stack approaches approximately 353 K, but peak temperature increases with inlet temperature.

3.3 Current density, voltage stability and load-following capability

The dynamic current-density response was strongly shaped by the imposed load profile. All temperature cases showed transient peaks and oscillations, with current density reaching approximately 0.95 A cm-2 during high-demand periods. The similarity of current-density peaks across the temperature range indicates that the load profile, rather than inlet temperature alone, dominated the instantaneous current demand. Nevertheless, the associated voltage response improved slightly at higher temperature, especially under high-current conditions, because activation and ohmic losses were reduced.

Stack voltage oscillated with the dynamic load. It started at higher values during low-current operation and decreased when the current demand increased. This behaviour is consistent with PEMFC loss mechanisms. The higher-temperature cases showed better average voltage stability, indicating that elevated temperature can improve load-following capability. For practical systems, this result supports the use of temperature-informed control strategies that coordinate stack temperature, humidification and cooling to reduce voltage drops during load transients.

3.4 Heat generation and electrical power output

Heat generation is a critical design parameter because it determines the required cooling capacity and influences membrane hydration. In the simulations, heat generation varied dynamically with current and voltage. Heat peaks occurred during high-current periods, when activation, ohmic and concentration losses were most severe. Across the four inlet-temperature cases, the peak heat generation was approximately 37-40 kW, whereas the heat value approached a low level during low-load or resting intervals. This confirms that the cooling system must be sized for peak transient heat removal, not merely average operating heat.

The electrical power output followed the same dynamic pattern as the current and voltage response. The higher-temperature cases, particularly 60 and 70 °C, showed slightly more stable power delivery. The 70 °C case provided the strongest output tendency because improved kinetics reduced internal losses. However, the higher peak stack temperature at 70 °C also introduces greater risk of membrane dehydration. Therefore, the 70 °C case is best interpreted as a high-performance operating point that requires robust thermal and water control, while 60 °C may represent a safer compromise between performance and durability.

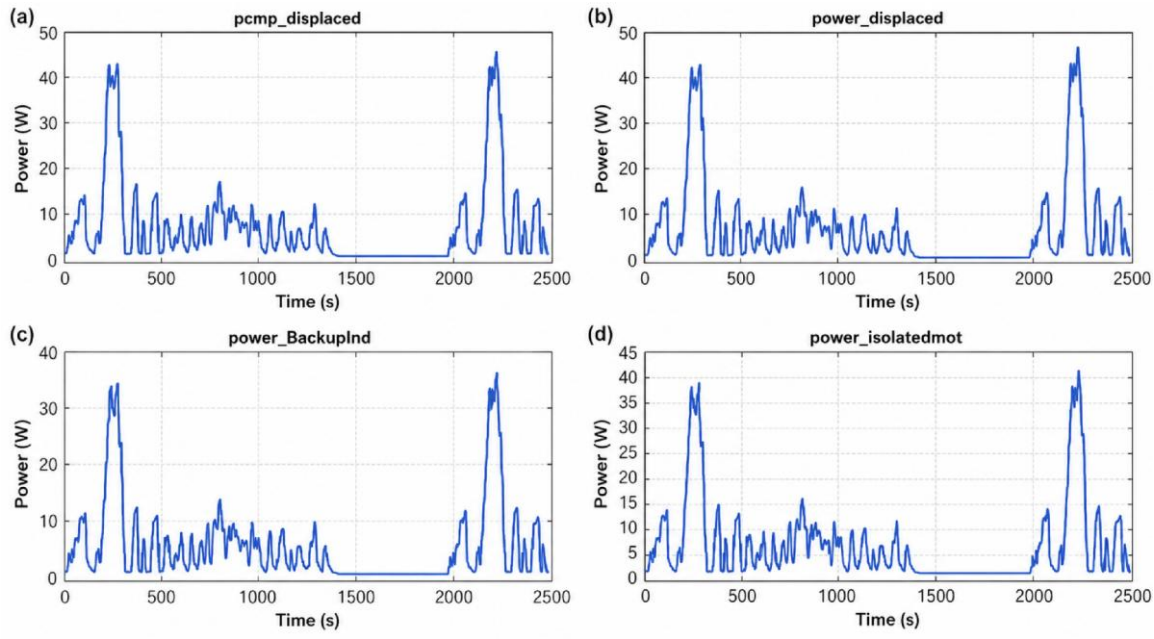

Figure 4. Dynamic heat-generation response for all inlet-temperature cases. Peak heat generation of approximately 37-40 kW indicates the cooling requirement during load transients.

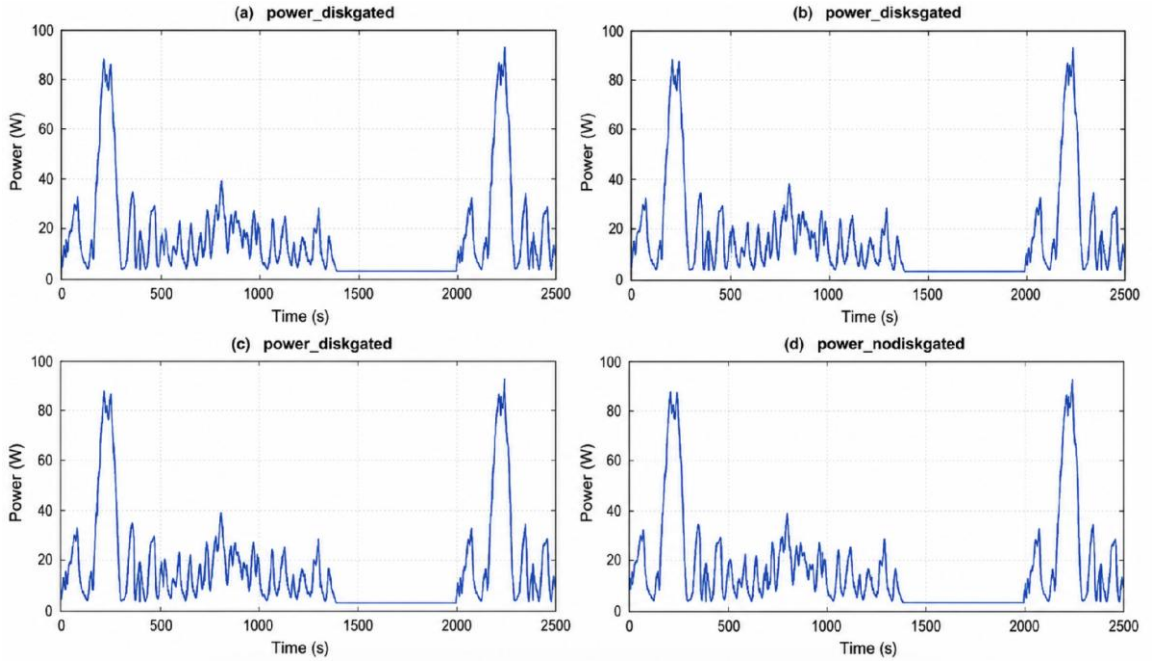

Figure 5. Dynamic PEMFC stack power output under the same load profile. Higher-temperature cases show slightly improved stability and output response.

3.5 Water production and hydrogen consumption

Water production is both a useful indicator of electrochemical activity and a potential source of performance loss. In the simulations, water production followed the load profile and increased during high-current operation. Peak water production reached approximately 10 g s-1, while low-load periods approached 0-4 g s-1. This confirms correct coupling between electrochemical reaction rate, current generation and product-water formation. From a design

perspective, the result emphasises that water management must be dynamic. Excessive water accumulation can flood electrodes and reduce oxygen access, while insufficient water leads to membrane dehydration and higher ohmic losses.

Hydrogen consumption also followed the current and power demand. The average consumption reached up to approximately 0.4 g s-1 during nominal operation, while peak consumption reached approximately 1.1 g s-1. This value is important for hydrogen supply sizing, pressure regulation and purge strategy. A supply system designed only around average consumption could experience pressure drop during peak demand. Higher temperature may reduce some voltage losses and improve reaction kinetics, but it does not remove the need for adequate fuel delivery during transients. Therefore, stack control should coordinate temperature, reactant flow and water management rather than optimising temperature alone.

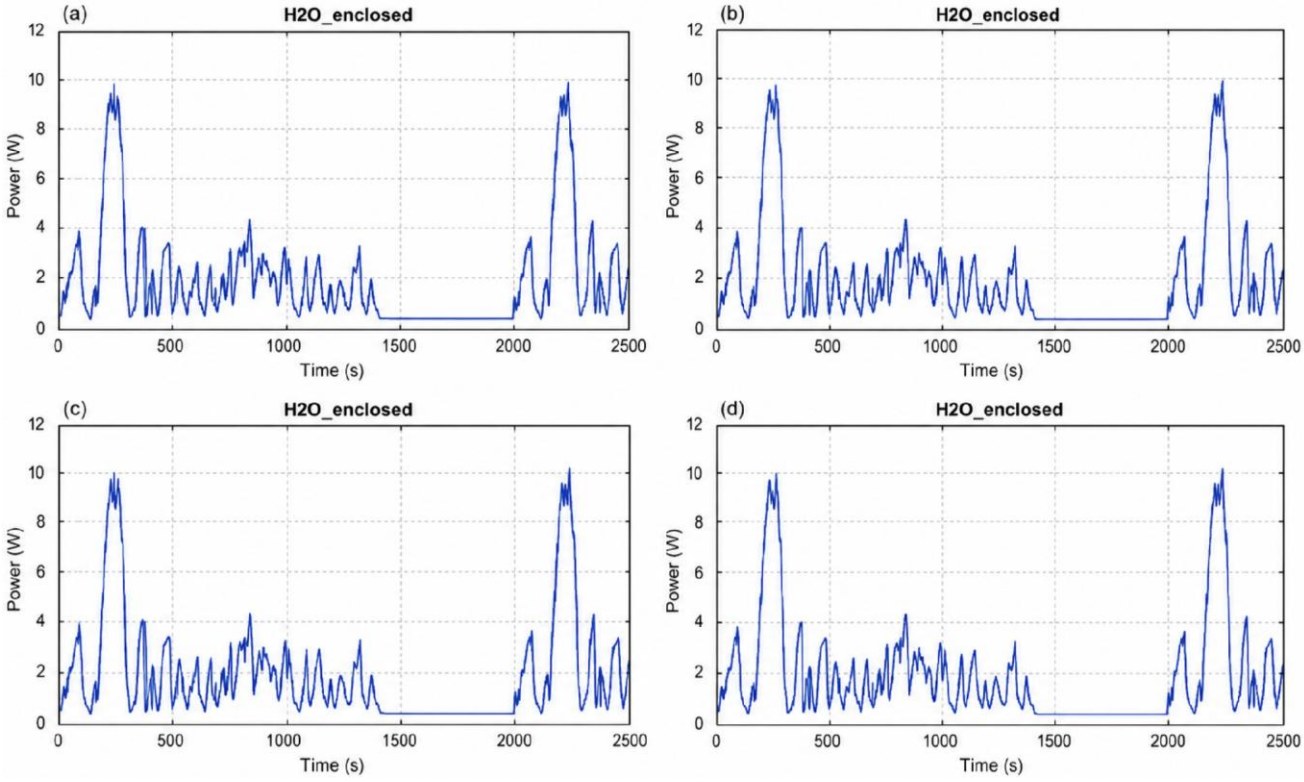

Figure 6. Water-production response under dynamic load. Product-water formation follows the current and power profile, with peaks of about 10 g s^{-1}.

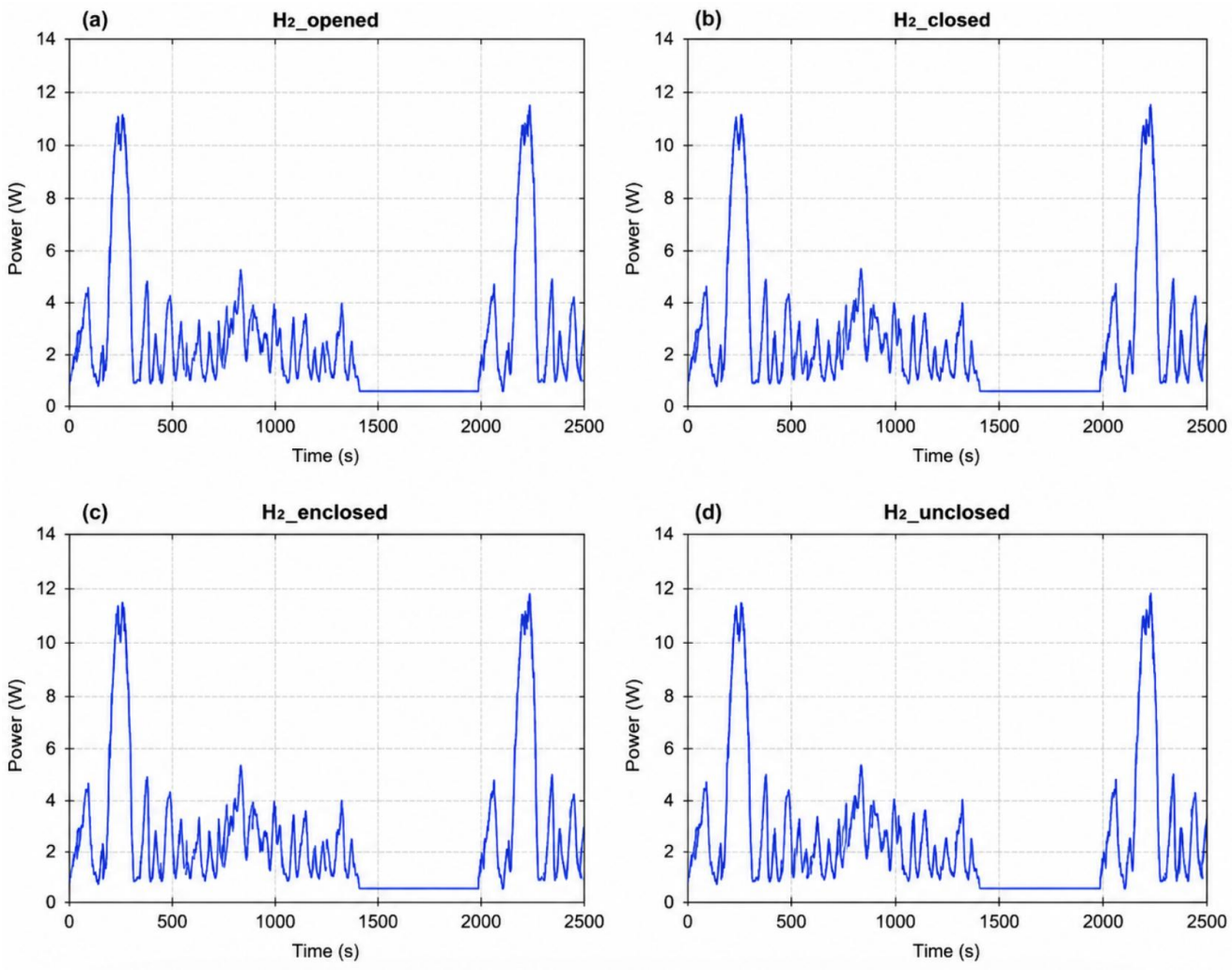

Figure 7. Hydrogen-consumption response under dynamic load. Peak hydrogen demand of about 1.1 g s-1 should be considered in fuel-supply sizing.

4. Practical Operating-Window Assessment

The combined results indicate that the PEMFC stack benefits from elevated inlet temperature, especially when high-current operation is required. The 40 °C case is thermally safer but provides weaker polarization behaviour. The 50 °C case improves performance but remains intermediate. The 60 °C case gives a favourable balance between improved kinetics, acceptable peak temperature and manageable water/thermal loads. The 70 °C case provides the strongest high-current and power response, but also produces the highest peak stack temperature and therefore the highest dehydration risk.

The operating-window recommendation is subject to several model limitations. Long-term catalyst ageing, membrane chemical degradation, mechanical stress, manufacturing variability, sensor uncertainty and cell-to-cell maldistribution are not represented explicitly. In addition, the hydrogen pressure and balance-of-plant parameters are model inputs rather than experimentally calibrated values for a specific physical stack. These omissions do not invalidate the comparative temperature trend, but they limit the use of the present results for absolute component sizing or lifetime prediction.

For an energy-system application, the recommended operating window is therefore 60-70 °C, with 60 °C as the more conservative set point and 70 °C as a high-performance set point requiring stronger cooling and humidification. The exact choice should depend on the application priority. If maximum transient power is required and the balance-of-plant can remove heat effectively, 70 °C is attractive. If durability and control margin are more important, 60 °C is preferable. In both cases, water and thermal management must be designed as active control functions rather than passive supporting components.

5. Conclusions

A MATLAB-Simscape PEMFC model was used to evaluate the effect of inlet temperature on a 400-cell stack under dynamic load. Relative to the thesis, the journal study applies a controlled four-temperature comparison, integrates electrochemical and balance-of-plant outputs, and introduces an operating-window interpretation supported by physical-consistency and literature-based trend checks. Increasing inlet temperature from 40 to 70 °C improved high-current polarization behaviour and power stability. All cases approached a quasi-steady stack temperature of approximately 353 K, but peak stack temperature increased from 353 K at 40 °C to 364 K at 70 °C. Current density reached approximately 0.95 A cm-2, heat generation peaked at about 37-40 kW, water production reached about 10 g s-1 and hydrogen consumption reached about 1.1 g s-1 during peak demand.

The main conclusion is that 60-70 °C is the most useful inlet-temperature range for the simulated system. The 70 °C case gives the strongest high-current response because electrochemical kinetics are more favourable, whereas 60 °C provides a more conservative compromise with greater thermal and hydration margin. The recommendation remains conditional because the model has not yet been validated against matched experimental data. Future work should therefore compare the simulation with polarization curves, electrochemical impedance spectra, distributed stack-temperature measurements, hydrogen-flow data and water-balance measurements obtained under the same transient load cycle. Subsequent model development should incorporate spatial temperature and hydration effects, degradation submodels and closed-loop control of cooling, humidification and hydrogen delivery. Until such validation is completed, the present model is most appropriate for comparative trend analysis and preliminary operating-window screening rather than absolute performance certification.

Acknowledgements

The authors gratefully acknowledge the financial support from Ministry of Higher Education under HiCoE (SELFUEL): HiCoE-2023-001 and Universiti Kebangsaan Malaysia, UKM – TR 2024 - 17.

Author Contributions

The authors declare that they contributed equally to all stages of this manuscript and research.

Declaration of Competing Interest

The authors declare no conflict of interest.

Data availability

The simulation data were generated from the MATLAB-Simscape model described in this manuscript and can be made available upon reasonable request.

References

[1] Barbir F. PEM Fuel Cells: Theory and Practice. Academic Press; 2013.
[2] Miri M, Tolj I, Barbir F. Review of proton exchange membrane fuel cell-powered systems for stationary applications using renewable energy sources. Energies 2024;17:3814.
[3] Zhang J, Zhang H, Wu J, Zhang J. PEM Fuel Cell Fundamentals. PEM Fuel Cell Testing and Diagnosis. Elsevier; 2013. p. 1-42.
[4] Zhang J, Zhang H, Wu J, Zhang J. The effects of temperature on PEM fuel cell kinetics and performance. PEM Fuel Cell Testing and Diagnosis. Elsevier; 2013. p. 121-141.
[5] Williamson ZR, Kim D, Chun DK, Squibb CW, Lee T. Experimental evaluation of cell temperature effects on miniature, air-breathing PEM fuel cells. ASME Fuel Cell Science, Engineering and Technology Conference; 2011. p. 875-882.
[6] Hamzah SNM. Simulation and analysis of PEM fuel cell system using MATLAB. Research Progress in Mechanical and Manufacturing Engineering 2023;4:389-397.
[7] Ioannis N, Andreas M, Stavros N, Eleftheria P, Milias-Argitis I. PEM fuel cell system evaluation using operational data and updated Matlab/Simulink simulation tools. IET Conference Publications; 2010.
[8] M S, V A, G K. Modelling of PEM fuel cell using MATLAB Simulink. International Journal for Research in Applied Science and Engineering Technology 2023;11:2111-2113.
[9] Faghri A, Guo Z. Challenges and opportunities of thermal management issues related to fuel cell technology and modelling. International Journal of Heat and Mass Transfer 2005;48:3891-3920.
[10] Farsi A, Rosen MA. Thermal management of polymer electrolyte membrane fuel cells: comparative assessment of cooling systems. e-Prime 2023;4:100174.
[11] Choi J, Sim J, Oh H, Min K. Resistance separation of polymer electrolyte membrane fuel cell by polarization curve and electrochemical impedance spectroscopy. Energies 2021;14:1491.
[12] Ustinov A, Khayrullina A, Sveshnikova A, Abrosimov K. Effect of inlet air temperature and relative humidity on performance of PEM fuel cell. HEFAT; 2016.
[13] Mohammedi A, Sahli Y, Moussa HB. Three-dimensional numerical study of the inlet temperature effects on the performance of planar PEMFCs. Algerian Journal of Renewable Energy and Sustainable Development 2022;4:16-23.
[14] Atak NN, Dogan B, Yesilyurt MK. Theoretical analyses of the performance parameters of PEM fuel cells at various operating temperatures and pressures. Proceedings of the Institution of Mechanical Engineers, Part A: Journal of Power and Energy; 2024.
[15] Pei Y, Chen F, Jiao J, Mo T, Li Y. Inlet gas temperature control technology for PEMFC stack test benches. SAE Technical Papers; 2023.
[16] Ying J, Liu T, Wang Y, Guo M, Shen Q, Lin Y, Yu J, Yu Z. Perspectives on membrane development for high temperature proton exchange membrane fuel cells. Energy & Fuels 2024;38:6613-6643.

Malaysian Journal of Energy and Applications 1 (2026): 84-98
https://doi.org/10.17576/myjea.2026.01.84

PLATINUM CATALYSIS IN FUEL CELL: AN OVERVIEW

Omar Syah Jehan Elham[1]*, Siti Kartom Kamarudin[2], Zulfirdaus Zakaria[3], Nur Hidayah Ahmad Zaidi[4], Abul K Azad[5], Siti Hasanah Osman[2]

[1]*Faculty of Chemical Engineering, Universiti Teknologi MARA (UiTM), Johor Branch, Pasir Gudang Campus, Johor, Malaysia*
[2]*Fuel Cell Institute, Universiti Kebangsaan Malaysia, 43600 UKM Bangi, Selangor, Malaysia.*
[3]*Institute for Advanced Studies, Universiti Malaya, 50603 Kuala Lumpur, Malaysia*
[4]*Fakulti Kejuruteraan & Teknologi Kimia, 02600 Arau, Perlis, Universiti Malaysia Perlis, Malaysia.*
[5]*Faculty of Integrated Technologies, Integrated Sciences Building, Universiti Brunei Darussalam, Brunei.*

**Corresponding author: omar7175@uitm.edu.my*

Received 7/7/2026; Received in Revised Form 18/7/2026;
Accepted 20/7/2026; Available Online 20/07/2026.

Abstract

Fuel cells are emerging as a promising clean energy technology in the global transition to sustainable power generation and can contribute to Sustainable Development Goal 7 (Affordable and Clean Energy). Platinum is the most frequently used electrocatalyst for fuel cells, as it is a highly efficient catalyst with excellent corrosion resistance and long-term stability in electrochemical processes. Platinum is widely used at both the anode and cathode in fuel cells and underpins fuel cell electrocatalysis, but this platinum-based catalyst layer typically accounts for around 15–20% of the total fuel cell stack cost, making it one of the main barriers to commercialization. This review provides a detailed examination of the use of platinum in fuel cells and discusses its geological history, physicochemical properties, industrial importance, and catalytic roles in proton exchange membrane fuel cells (PEMFCs), direct methanol fuel cells (DMFCs), direct ethanol fuel cells (DEFCs), and microbial fuel cells (MFCs). It integrates a geological perspective with catalytic applications and emerging catalyst development strategies to demonstrate the continued relevance of platinum for future fuel cell technology and to provide a comprehensive outlook on the future development of efficient, durable, and economically viable fuel cell technologies.

Keywords: Platinum, Fuel cell electrocatalysts, Proton exchange membrane fuel cells (PEMFCs), Direct methanol fuel cells (DMFCs), Clean energy technologies

1. Introduction

Fuel cells are seen by many people as a key solution for the 21st century [1], enabling clean, efficient production of power and heat from a range of primary energy sources. Fuel cells can vary from tiny devices producing only a few watts of electricity to large power plants producing megawatts. All fuel cells are based on a central design using two electrodes separated by a solid or liquid electrolyte that carries electrically charged particles between them. A catalyst is often used to speed up the reactions at the electrodes. Fuel cell types are generally classified according to the nature of the electrolyte they use. Each type requires particular materials and fuels and is suitable for different applications [2][3]. The origins of fuel cell technology can be traced back to the early nineteenth century, when the underlying concept was first effectively demonstrated by Humphry Davy. This early work was subsequently advanced in 1832 by Christian Friedrich Schönbein, whose investigations laid further groundwork for the field. William Grove, a chemist, physicist and lawyer, is generally credited with inventing the first fuel cell in 1839. Central to the performance of many fuel cell systems is platinum, a metal

noted for its superior resistance to corrosion, its stability in air without oxidising and its overall chemical inertness. Platinum belongs to a broader family of platinum-group metals (PGMs) that also includes palladium, osmium, ruthenium, rhodium and iridium [3].

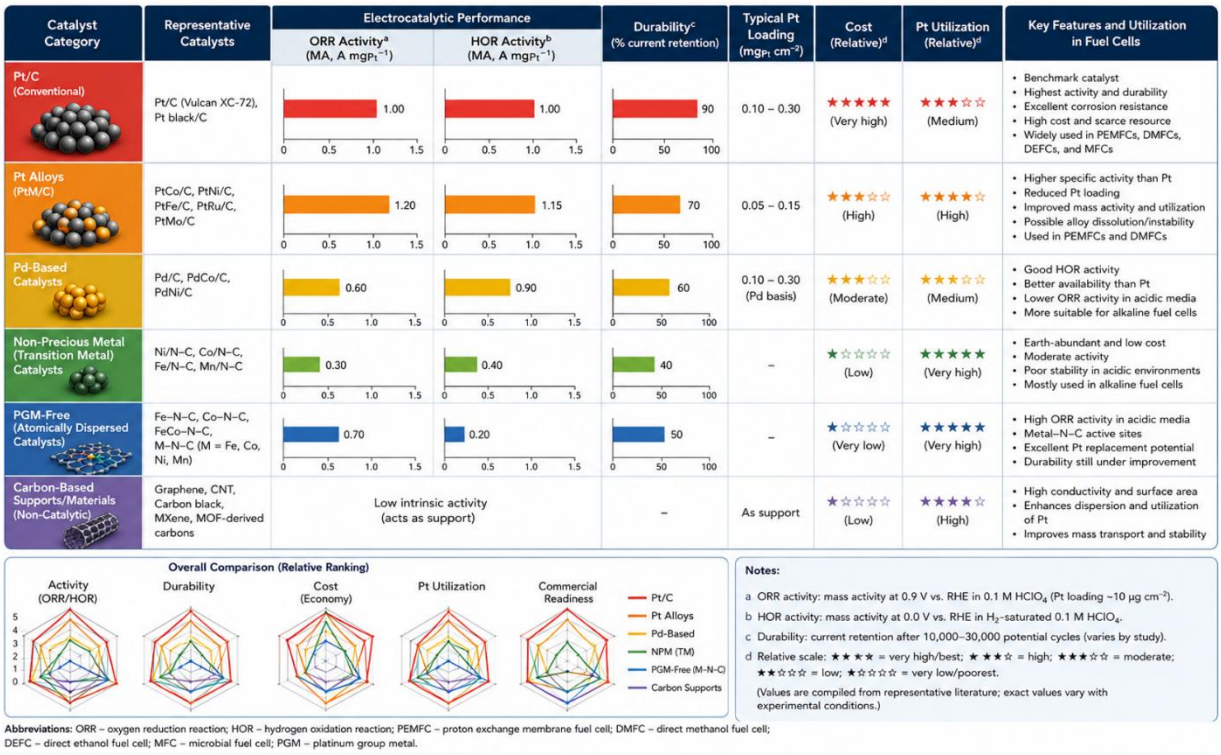

Figure 1: Comparison of platinum and alternative catalyst in fuel cells: performance and utilization

Within the fuel cell itself, these properties translate directly into catalytic function: platinum is highly effective at facilitating the oxygen reduction reaction (ORR) at the cathode and the hydrogen oxidation reaction (HOR) at the anode, the two electrochemical processes that together generate electrical current [4]. Its resistance to corrosion and chemical stability allow it to sustain this catalytic activity even under the highly acidic and oxidising conditions present within the cell, a demand that few other metals are able to withstand over extended operating periods. It is this combination of high intrinsic activity and long-term stability that has established platinum as the benchmark catalyst for fuel cell applications, even as its scarcity and cost continue to drive research towards more efficient and economical alternatives [5]. Beyond its role in fuel cells, platinum's most significant industrial application lies in the automotive sector, where it serves catalytic converters that facilitate the complete combustion of unburned hydrocarbons in vehicle exhaust systems. It is also used in jewellery, decorative items and dental work, reflecting its broader value as a precious and functionally versatile metal. Against this backdrop, this review examines the geological origin of platinum and its catalytic application in fuel cells, with particular attention to the functional properties of platinum in relation to its morphology, as well as the opportunities and challenges surrounding its industrial use. Figure 1 shows the comparison of platinum and alternative catalysts in fuel cells: performance and utilisation.

2. Platinum

Independently discovered in 1735 by Julius Scaliger and in 1741 by Charles Wood, platinum is named from the Spanish platina, meaning “little silver”. The metal is classified as precious owing to its scarcity and commercial demand [6]. It has a coefficient of expansion almost equal to that of soda-lime-silica glass and is therefore used to make sealed electrodes in glass systems. The presence of platinum wire can cause hydrogen and oxygen gas mixtures to explode. There are six naturally occurring isotopes, of which the most abundant are platinum-194, accounting for 33%, platinum-195 (34%), and platinum-196 (25%). The others are platinum-198 (7%), platinum-192 (1%), and platinum-190 (0.01%). The latter is weakly radioactive, witha half-life of 700 billion years, while the other five are non-radioactive [7]. Physically, platinum is heavy, soft, malleable (easy to work – only silver and gold are easier to shape), and ductile (easy to draw into wires), and has a fairly high melting point (~1770 °C or 3220 °F). Chemically, it is often described as a noble metal because it is so unreactive. It does not react with oxygen in air, so it does not rust or tarnish. It is also reasonably resistant to attack from acids [8].

In the early 1800s, platinum was used in fuel cells to promote the chemical reaction of hydrogen with oxygen. It is generally a good inert electrode because it is chemically unreactive. This makes it very useful in fuel cells. It can easily adsorb hydrogen and, being an inert metal, does not participate in redox reactions during the operation of the cell [9]. In hydrogen fuel cells, platinum is the best catalyst, but it comes with a high price tag [10]. In December 2018, platinum was a precious metal more rare than silver or gold [11]. Platinum is more expensive because it is rarer and mined much less than gold. Only 160 tonnes of platinum are mined annually, as opposed to 1,500 tonnes of gold. Also, platinum is denser than gold, so the same ring will weigh significantly more in platinum than in gold (and precious metals are priced by weight) [12]. Recently, scientists have been looking to create practical fuel cell catalysts that use far less of this costly precious metal. In new research from the U.S. Department of Energy's (DOE) Argonne National Laboratory, published in Science, scientists have identified a new catalyst with the effectiveness of the available platinum but using only about a quarter as much platinum as current technology [13]. Annual platinum demand was down slightly in 2017 at 7.8 million ounces, with supply at about eight million. Current projections from the World Platinum Council for 2018 are that supply will fall a little, and demand will rise, with the two remaining more or less in equilibrium. Roughly 75% of supply comes from mining and 25% from recycling. Of that mined supply, a good two-thirds comes from South Africa. Platinum’s fate is determined by one country in a way that no other commodity, except perhaps cobalt, is [14]. Figure 2 shows the platinum supply versus demand. The demand for 2018 can be cover by production. It shows that platinum is very important in industry, particularly for applications related to direct methanol fuel cells. Fluctuations of total supply in the range 7,265–8,080 koz can be recovered within the total demand. It shows that platinum production needs to increase so that industrial demand can be fully met [15].

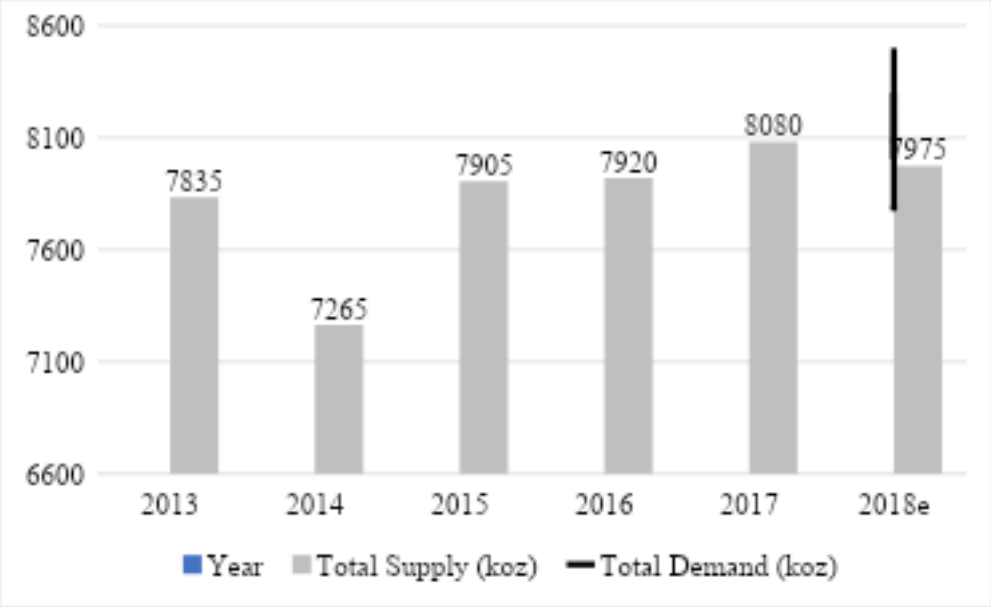

Figure 2: Platinum Supply vs. Demand (2013-2018) [16]

3. Geology

The majority of the world's platinum comes from South Africa, with Russia supplying the second highest yields and Colombia the third [17]. The gold-bearing sands of these three countries provide ideal geological conditions for recovering this very rare metal. The Bushveld Complex, located in South Africa, contains some of the richest ore deposits on Earth. The complex holds the world's largest reserves of platinum group elements (PGEs), which include platinum, palladium, rhodium, ruthenium, osmium and iridium, all of which are extremely rare in the Earth's crust. Platinum, the most abundant of these, is 30 times rarer than gold. Mined only in a few places worldwide, these elements are becoming increasingly important in applications such as pollution control [18]. The major geological feature associated with this wealth of mineral deposits is the Bushveld Complex (Figure 3), where its mineralised and non-mineralised layers extend, with little variation, for tens of kilometres along strike [19]. The Bushveld Complex, found in the northern part of South Africa, is the world's largest layered intrusion, is approximately 2 billion years old, and is divided into four different limbs: the northern, southern, eastern and western limbs [16,17]. In 1897, Gustaaf Molengraaff was the first to discover the Bushveld Complex [22]. The Bushveld Complex is a layered mafic intrusion with well-defined ore bodies consisting of stratiform chromitite layers concentrated within the critical zone; these are referred to as reefs. The Merensky Reef, UG2 Reef and Platreef are the main reef deposits, consisting mostly of continuous to discontinuous chromite layers with varying amounts of PGE mineralisation [23].

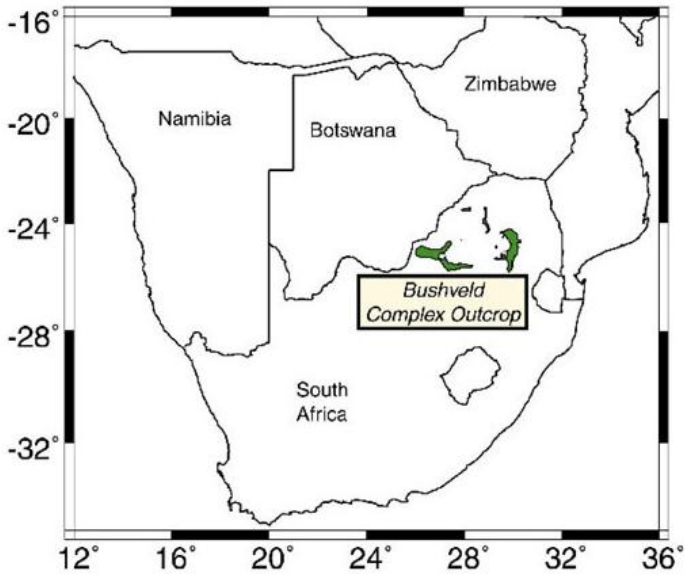

Figure 3: Map showing the position of the Bushveld Complex in South Africa [24]

Platinum is an extremely rare metal, occurring at a concentration of only 0.005 ppm in Earth's crust. It is sometimes mistaken for silver (Ag). Platinum is often found as native platinum and as an alloy with other platinum-group metals and iron, mostly as tabulated in Table 1. Native platinum is most often found in secondary deposits in alluvial sediments. The alluvial deposits used by pre-Columbian people in the Chocó Department, Colombia, are still a source of platinum-group metals. Another large alluvial deposit is in the Ural Mountains, Russia, and it is still mined [25]. Although platinum is rare, the methods for identifying where it is most likely located have become highly accurate, focusing on igneous deposits that show the tell-tale signs of prolonged heat and pressure [26]. By-product platinum is separated from the host metal during electrolytic refining. Placer platinum is concentrated by delicate gravity methods. Lode platinum is recovered by combined gravity and flotation methods. The individual metals of the platinum group are separated by complex refining processes. In addition to gold-bearing sands, deposits of platinum are often found in outcrops of plutonic rocks such as olivine and chromite. The formation of these rocks is a testament to platinum's pedigree, as all were exposed to extremely high temperature and pressure in order to produce this most valuable of metals [27]. Platinum is invariably associated with basic igneous rocks and with the ore minerals characteristic of those rocks. Most of the world's platinum is intimately associated either with chromite or nickel. Even platinum placers are derived from basic rocks rich in chromite. The platiniferous nickel ores also contain copper and appreciable quantities of gold and silver [28].

Table 1: Description critical zone, Bushveld Complex [29]

Merensky Reef	UG2 Reef	Platreef
~ Contains the base metal sulfide grains and associated platinum group minerals. ~ The Merensky Reef has been traced for 300 km around the entire outcrop of the eastern and western limbs of the Bushveld	~ The host rock of the UG2 chomitites is dominated by granular orthopyroxene. ~ The UG2 chromitites are underlain by pyroxenite footwall that is distinct from hanging wall pyroxenite.	~ The Lower Reef is composed of norites and feldspathic pyroxenites that have been recrystalled and overprinted. ~ The Central or Middle Reef is composed of igneous peridotite and recrystallized

Complex, and to depths of 5 km.	~ The Upper Reef is composed primarily of plagioclase-pyroxenite and norite

The chief uses for platinum are in the jewellery, electrical and dental industries. Its white colour and hardness make it a desirable setting for diamonds. In the electrical industry it is used for resistance and contacts in the more delicate instruments such as telephone and radios. Platinum finds wide uses in the chemical industry such as for containers, wire, electrodes, coils, acid making, x-ray equipment and as a catalyst. Large acid stills utilize considerable quantities. (Figure 4) show details platinum used.

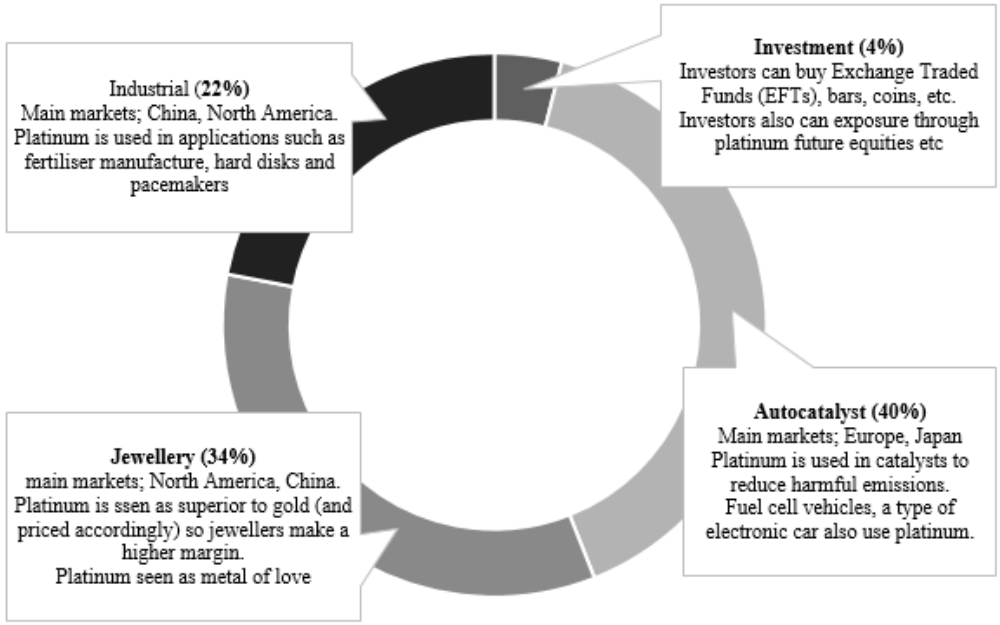

Figure 4: Major industrial application of platinum, including fuel cells, automotive catalytic converters, chemical processing, electronics, medical devices and jewelries [30].

In fuel cell application, platinum is considered the standard metal which breaking oxygen bonds apart to eventually form water in a process that requires a substantial amount of the catalyst [31]. The role of platinum in catalytic converters is to oxidise carbon monoxide (CO) and hydrocarbons. Platinum is particularly effective at this under oxygen-excessive conditions, so is often the metal of choice for diesel applications. Platinum works as a catalyst by collecting oxygen atoms (O), and letting them bind with the toxic carbon monoxide (CO), to create the less harmful carbon dioxide (CO_2). Platinum is most efficient catalysts for speeding up chemical reactions in hydrogen fuel cells. Oxygen molecules combine with electrons and hydrogen ions to form water at the cathode. At anode the, reaction is sluggish and speeding it up requires 10 times as much platinum as is used [32]. Platinum is an inert electrode, thus it do not participate in the cell reaction but provide a surface or platform for oxidation and reduction reaction.

4. Platinum as Catalyst

4.1 Direct Alcohol Fuel Cell

Bambagioni et al [33] explored on Pd and Pt–Ru anode electrocatalysts supported on multiwall carbon nanotubes and their use in passive and active direct alcohol fuel cells with an anion-exchange membrane (alcohol =methanol, ethanol, glycerol). The results obtained with Pt–Ru/MWCNT anodes in acid media are largely inferior to those provZided by Pd/MWCNT electrodes in alkaline media. Gupta et al. [34] applied polycrystalline deposits of platinum and platinum–ruthenium on a CuNi (70:30) alloy support. Novel CuNi alloy supported electrocatalyst synthesised from PTFE suspension of noble metal salts can be an alternative anode material for DAFC. DMFCs have many advantages, such as structural simplicity, instant refuelling [35] , high specific energy that is widely attained and safely stored [36], [37] high energy density of methanol, low operating temperature, and easy start up [35]. To maintain and improve all of these advantages, catalyst development is starting to attract developers' attention. Johanek et al. [38] reported vapor-feed low temperature direct methanol fuel cell with Pt and PtRu electrodes on chemistry insight. Energy efficiency of 30% and power density exceeding 70 mW cm^{-2} were achieved with Pt/C electrodes without any noticeable long-term degradation. Basri et al [39] study attempts to improve the performance of PtRu catalysts by adding nickel (Ni) and iron (Fe). The results, PtRuFeNi/MWCNT improves the reaction kinetics of anode catalysts for DMFCs and obtains a mass current of 31 A g^{-1} catalyst. Li et al [40] working on an enhanced activity of Pt/CNTs anode catalyst for direct methanol fuel cells using Ni_2P as co-catalyst. A novel Pt/Ni_2P/CNTs catalysts were prepared by the H_2 reduction method. The results the optimal Ni_2P loading amount for Pt/Ni_2P/CNTs catalyst was 6% with a MOR activity as high as 1400 mAmg^{-1} Pt.

In 2005, Mu et al [41] study on controllable Pt nanoparticle deposition on carbon nanotubes as an anode catalyst. The producer Pt/CNT composite shows higher electrocatalytic activities and catalyst tolerance that can be applied in DMFCs in comparison with the E-TEK catalyst. Prabhuram et al [42] explore on multi walled carbon nanotube supported PtRu for the anode of direct methanol fuel cells. Cyclic voltammetry results demonstrated that the MWCNT supported PtRu catalyst exhibited a higher mass activity (mA mg^{-1} of PtRu) for the methanol oxidation reaction than the carbon-supported. The direct methanol fuel cell performance test data showed that MWCNT-supported PtRu catalysts yielded about 35-39% higher power densities than the carbon-supported PtRu. In 2013, Zhou et al [43] studied on Pt based anode catalysts for direct ethanol fuel cells. Pt_1Ru_1/C further modified by Wand Mo showed improved ethanol electro-oxidation activity, but its DEFC performance was found to be inferior to that measured for Pt_1Sn_1/C. It was found that the single direct ethanol fuel cell having Pt_1Sn_1/C or Pt_3Sn_2/C or Pt_2Sn_1/C as anode catalyst showed better performances than those with Pt_3Sn_1/C or Pt_4Sn_1/C. Ishitobi et al [44] worked on Pt-Sn was supported on SiO_2 embedded carbon nanofiber as active anode catalyst for DEFC by expecting positive interactions between Pt-Sn-SiO_2. The composite catalyst, Pt_3Sn_1/SECNF, showed highest mass activity for the ethanol electrooxidation, which was 3.7 times higher than the activity of the commercial Pt/C (Pt/C_{com}) while maximum power density of DEFC single cell with the composite catalyst was 3.5 times higher than that with Pt/$C_{com.}$ Since 2003, the development of anode catalysts for a direct ethanol fuel cell being study by Vigier et al [45]. Ethanol electrooxidation was investigated at platinum-based electrodes: Pt, Pt–Sn, Pt–Re dispersed on a high surface area carbon powder. The results PtSn was the most active catalyst and PtSn electrocatalysts were the most selective towards the production of CO_2 compared to Pt and PtRe electrodes.

4.2 Proton Exchange Membrane Fuel Cell

Mohanta et al [46] prepared graphitized carbon by a promising stable cathode catalyst support material for long term PEMFC applications. The feasibility of a graphitized carbon (GC) as a cathode catalyst support for low temperature PEMFC is investigated. GC and CB supported Pt electrocatalysts were prepared via an already developed polyol process. Qu et al [47] worked on an effect of electrode Pt-loading and cathode flow-field plate type on the degradation of PEMFC. The decay of Pt/C catalyst in cathode is mainly caused by the corrosion of carbon support, and the degradation of anode Pt/C catalyst is a consequence of migra- tion and aggregation of Pt particles. Renzi et al [48] study low platinum loading cathode modified with $Cs_3H_2PMo_{10}V_2O_{40}$ for polymer electrolyte membrane fuel cells. The composite catalyst is prepared by mixing the POM salt with Pt/C by sonication. RRDE studies show better kinetics for ORR with low Pt loading at the electrode surface. A MEA is assembled by using a Pt/POM-based cathode, in order to assess performance in a working fuel cell.

Karthikeyan et al [49] work on highly durable platinum based cathode electrocatalysts for PEMFC application using oxygen and nitrogen functional groups attached nanocarbon supports. Compared to commercial Pt/C catalysts, durability show ~30% enhancement for the as prepared electrocatalysts due to the presence of large amount of pyrolic nitrogen and highly oriented graphitic nature of the catalyst supports. Roen et al [50] work on electrocatalytic corrosion of carbon support in PEMFC cathodes. The influence of platinum on the corrosion of carbon catalyst supports has been characterized by on-line mass spectroscopy during cyclic voltammetry, with varying Pt mass fraction, catalyst type, and temperature. The corrosion rate of carbon catalyst support is accelerated in the presence of Pt-containing catalysts. Yu et al [51] work on PtCo/C cathode catalyst for improved durability in PEMFCs. This work intends to evaluate the durability of PtCo/C cathode catalyst in a dynamic fuel cell environment with continuous water fluxing on the cathode. Cell performance enhancement by PtCo/C over Pt/C catalyst has been sustained over 2400 cycles and the overall performance loss of the PtCo/C membrane electrode assemblies (MEAs) was less than that of the Pt/C MEA.

4.3 Direct Methanol Fuel Cell

Bruno et al [52] platinum supported on mesoporous carbon as cathode catalyst for direct methanol fuel cells. Platinum nanoparticles supported on mesoporous carbon were obtained by an impregnation and reduction method with $NaBH_4$ as the reducing agent. The results obtained in this study show that the mesoporous carbon used as support improved the catalyst dispersion. Pt nanoparticles of 5.3 nm in size were obtained on MC, which is, on average, 25% smaller than those formed on Vulcan carbon under the same synthesis conditions. Makino et al [53] search an optimization of the sputter-deposited platinum cathode for a direct methanol fuel cell. Pt loading below 0.25 mg cm^{-2} achieved higher mass activities than that of 0.5 mg cm^{-2} prepared by the paste method, which was general conventional method. This result may suggest an increase in only electrochemically inactive Pt. Pt utilization efficiency can be found about ten times higher at Pt loading of 0.04 mg cm^{-2}. Moreover, addition of Nafion to sputter-deposited Pt cathodes is found possible to improve the catalyst activity for the ORR, but the excess Nafion over the optimum condition reduces the active sites.

Since 2003, Zhou et al [54] investigated on novel synthesis of highly active Pt/C cathode electrocatalyst for direct methanol fuel cell. The results this modified polyol process is simple and practical for the synthesis of highly dispersed Pt-based electrocatalysts with a narrow size distribution in the presence of high loading. The as-synthesized Pt/C electrocatalyst shows better electrocatalytic activity for oxygen reduction reaction in DMFC than that of the

commercial catalyst. Li et al [55] learned the nano-stuctured Pt–Fe/C as cathode catalyst in direct methanol fuel cell. Pt–Fe/C catalysts were prepared by a modified polyol synthesis method in an ethylene glycol (EG) solution, and then were heat-treated under H_2/Ar (10 vol. %) at moderate temperature (300 °C, Pt–Fe/C300) or high temperature (900 °C, Pt–Fe/C900). Further, Pt–Fe/C300 exhibits the higher ORR activity and better performance than other Pt/C or Pt–Fe/C catalysts in direct methanol single cell test, the increasing of cell performance may be attributed to more Pt^0 species existing and Fe ion corrosion from catalysts, which is believed to facilitate the H_2O_2 decomposition of Pt sites.

4.4 Microbial Fuel Cell

MFCs constitute a promising approach to wastewater treatment technology by capturing energy in the form of electricity or hydrogen gas [56]. Erable et al [57] run iron-nicarbazin derived platinum group metal-free electrocatalyst in scalable-size airbreathing cathodes for microbial fuel cells. Low-cost organic precursor was synthesized using Sacrificial Support Method (SSM). The tests in MFCs showed a maximum power density of 1.85 W m^{-2}. The MFCs performances due to the addition of Fe-NCB were much higher compared to the iron-free material. Considering the existing conditions, the higher overall power predicted was 3.6 mW at 22.2 S m^{-1} and at inter electrode distance of 1 cm. Kodali et al [58]investigate air breathing cathodes for microbial fuel cell using Mn-, Fe-, Co- and Ni-containing Platinum Group Metal-free Catalysts. Results showed that the addition of Mn, Fe, Co and Ni to AAPyr increased the performances compared to AC. The best performing catalyst (Fe-AAPyr) was then tested in MFC with increasing solution conductivity from 12.4 $mScm^{-1}$ to 63.1 $mScm^{-1}$. A maximum power density of 482±5 μWcm^{-2} was obtained with increasing solution conductivity, which is one of the highest values reported in the field. Kodali et al [59] report novel iron based catalysts synthesized using polymer salt pyrolysis technique were tested in RRDE and MFCs. Morphology of the novel catalysts showed a porous structure with graphitic flakes containing a large number of holes. The best electro-catalytic activity was achieved for PABA-850. The Fe-based catalyst was then integrated into air breathing cathodes and tested in the working MFCs. Fe-catalysts had the higher power density recorded that was 178 ± 3 μWcm^{-2} by PABA-850 and 173 ± 3 μWcm^{-2} by PABA-950. At last, AC had a power peak of 131 ± 4 μWcm^{-2}. Ghasemi et al [60] work on activated carbon nanofibers as an alternative cathode catalyst to platinum in a two-chamber microbial fuel cell. As a result, it was found that the MFC with the chemically activated carbon nanofibers (ACNFs) exhibited better catalytic activity than that of the physically activated ACNFs. The power per cost of ACNFs with 8 M KOH is 2.65 times greater than that of the traditionally used platinum cathode. Thus, ACNFs are a good alternative catalyst to Pt for MFCs.

5. Current Problems and Future Development

The fuel cell industry has weathered a challenging period of transition from research and development toward full commercialization, and although many manufacturers remain some distance from profitability, the long-term growth outlook stays promising [61]. In the fully sustainable energy system envisioned for the coming decades, hydrogen produced through renewable-powered electrolysis, or biofuels, is expected to serve as the primary fuel source. Yet in most current designs, the cathode and anode catalyst layers still rely on platinum (Pt), a scarce and costly precious metal that can account for 10–15% of total fuel cell stack cost. Without a reduction in Pt content, this share is projected to grow further as manufacturing volumes scale up, since platinum-group-metal (PGM) loading and system cost remain closely correlated year over year [62]. Platinum therefore continues to represent one of the principal

barriers to widespread commercial adoption of fuel cells, and reducing Pt loading without compromising catalytic performance has become a central research priority.

One well-established approach to improving cathode catalyst performance is alloying platinum with transition metals such as cobalt and nickel; however, these alloying elements are prone to leaching under fuel cell operating conditions, resulting in progressive performance degradation over time [63]. Recent work on core-shell catalyst architectures has sought to address this durability limitation directly, with reduced-Pt-content core-shell nanocatalysts shown to enhance both catalytic activity and structural stability compared with conventional alloy catalysts [64]. Building on this design philosophy, our own high-performing catalyst layer achieves a five-fold improvement in durability relative to a conventional design using the same alloy catalyst. The success of certain application segments in recent years has driven a move toward consolidating specific technologies into standard reference designs, with fuel cells increasingly developed as scalable energy solutions capable of serving multiple market segments, from auxiliary power units (APU) to unmanned aerial vehicles (UAV) [65].

Looking ahead, several complementary strategies are currently being pursued to improve platinum utilization efficiency and, ultimately, to reduce reliance on platinum-group metals altogether. These include: (i) alloying platinum with one or more other metals; (ii) depositing platinum as a surface or near-surface layer over a different base metal; (iii) employing a core–shell approach in which a cheaper metal core is coated with platinum; and (iv) alloying platinum followed by selective dealloying. Beyond these Pt-based strategies, growing attention is being directed toward platinum-group-metal-free (PGM-free) catalysts, such as iron–nitrogen–carbon (Fe–N–C) systems, alongside advances in nanostructured supports and membrane technology, which have recently improved power density and operational stability considerably [66]. Nevertheless, durability under real-world operating conditions remains the primary technical barrier constraining the commercial readiness of current PGM-free catalysts, suggesting that future development of fuel cell catalysis will likely follow a combined pathway: continued refinement of ultralow-Pt core-shell and dealloyed architectures in the near term, progressively complemented by PGM-free alternatives as their stability and activity converge with performance targets.

6. Conclusion

Platinum remains the most efficient catalyst for accelerating the electrochemical reactions within hydrogen fuel cells, owing to its unique ability to withstand the highly acidic operating environment that few other metals can tolerate; it is this same property, however, that anchors its position as the rate-determining component of catalytic performance, including its strong activity toward oxygen reduction and the decomposition of hydrogen peroxide into water and oxygen. Yet this catalytic advantage comes at a considerable cost, as platinum's scarcity and price have long constrained the broad, large-scale deployment of fuel cell technology. This scarcity is compounded by a highly concentrated global supply chain, with approximately 90% of the world's platinum originating from only two countries, South Africa and Russia, exposing the industry to significant geopolitical and economic risk. From a geological standpoint, platinum's rarity is further explained by its natural occurrence: it forms within ultramafic igneous rocks and is typically associated with minerals such as chromite and olivine, rarely crystallising in pure, well-formed structures and instead being recovered mainly as nuggets or fine grains disseminated through host rock. Taken together, these geological, economic, and supply-chain constraints underscore why reducing platinum content, without sacrificing catalytic efficiency, remains one of the most pressing challenges in advancing fuel cell

technology toward wider commercial viability, even as platinum's unmatched catalytic properties continue to affirm its central and, for the foreseeable future, largely irreplaceable role in this field. This challenge is closely aligned with several Sustainable Development Goals (SDGs): platinum-based fuel cells support SDG 7 (Affordable and Clean Energy) by enabling efficient, low-emission power generation, while efforts to reduce platinum loading and diversify supply chains contribute to SDG 9 (Industry, Innovation and Infrastructure) through the advancement of more resilient and sustainable catalyst technologies. Furthermore, mitigating dependence on a geographically concentrated and environmentally intensive mining supply chain speaks to SDG 12 (Responsible Consumption and Production), reinforcing the need for resource-efficient catalyst design as a pathway toward more equitable and sustainable global energy systems.

Acknowledgements

The authors gratefully acknowledge the financial support for this work by the Universiti Kebangsaan Malaysia under Grant No: GGPM-2024-046.

Author Contributions

Omar Syah Jehan Elham: Conceptualization, supervision, writing—review and editing, funding acquisition. **Siti Kartom Kamarudin:** Conceptualization, supervision, writing—review and editing, funding acquisition. **Zulfirdaus Zakaria:** Literature investigation, data curation, writing—review. **Nur Hidayah Ahmad Zaidi:** Literature investigation, visualization, data curation. **Abul K. Azad:** Critical review, scientific validation, writing—review and editing. **Siti Hasanah Osman:** Conceptualization, literature investigation, methodology, data curation, visualization, writing—original draft, project administration.

Declaration of Competing Interest

The authors declare that they have no known competing financial interests or personal relationships that could have appeared to influence the work reported in this paper. All authors have read and agreed to the published version of the manuscript.

References

[1] S. H. Osman *et al.*, “Review on Direct Methanol Fuel Cells : Bridging the Gap between Theory and Application for Sustainable Energy Solutions,” 2025, doi: 10.1021/acs.energyfuels.4c05357.

[2] Y. Luo *et al.*, “Development and application of fuel cells in the automobile industry,” *J. Energy Storage*, vol. 42, p. 103124, Oct. 2021, doi: 10.1016/J.EST.2021.103124.

[3] Q. Hassan, I. D. J. Azzawi, A. Z. Sameen, and H. M. Salman, “Hydrogen Fuel Cell Vehicles: Opportunities and Challenges,” vol. 15, no. 15, p. 11501, Jul. 2023.

[4] Z. A. Che Ramli *et al.*, "Evaluating electrocatalytic activities of Pt, Pd, Au and Ag-based catalyst on PEMFC performance: A review," *Int. J. Hydrogen Energy*, vol. 104, no. April 2024, pp. 463–486, 2025, doi: 10.1016/j.ijhydene.2024.04.177.

[5] H. Liu, Q. Song, Y. Xie, W. Zhang, Q. Xu, and H. Su, "Recent Progress of Low Pt Content Intermetallic Electrocatalysts Toward Proton Exchange Membrane Fuel Cells," *Catalysts*, vol. 15, no. 11, pp. 1–21, 2025, doi: 10.3390/catal15111070.

[6] D. Kharzeev, R. D. Pisarski, and M. H. G. Tytgat, "PARITY ODD BUBBLES IN HOT QCD."

[7] J.-P. Elsevier Science (Firm), A. Luguet, O. Alard, A. Bezos, and T. Meisel, *Chemical geology.*, vol. 248, no. 3–4. Elsevier Science Pub. Co.

[8] "USGS Mineral Resources Program Platinum-Group Elements-So Many Excellent Properties Great Dyke of Zimbabwe Implats Mimosa Project-South Hill Mine," 2014, doi: 10.3133/fs20143064.

[9] "17.2 Galvanic Cells – Chemistry." .

[10] *Fuel Cell Handbook (Seventh Edition)*. 2004.

[11] L. Chong *et al.*, "Ultralow-loading platinum-cobalt fuel cell catalysts derived from imidazolate frameworks," *Science (80-.).*, vol. 362, no. 6420, pp. 1276–1281, Dec. 2018, doi: 10.1126/science.aau0630.

[12] "Michael, Author at Michael Arthur Diamonds - Page 3 of 6." .

[13] S. Thomas and M. Zalbowitz, "Fuel Cells - Green Power," 1999.

[14] "Platinum is cheap – but will it ever get expensive again? - MoneyWeek." .

[15] J. Matthey, "PGM MARKET REPORT FEBRUARY 2018 1 Precious Metals Management," 2018.

[16] J. CIAMPAGLIA, "Special Report: The Platinum Opportunity," *Sprott USA*, 2018. .

[17] "Gold | The most precious of metals (Part 2)." .

[18] S. H. Richardson and S. B. Shirey, "Continental mantle signature of Bushveld magmas and coeval diamonds," *Nature*, vol. 453, no. 7197, pp. 910–913, Jun. 2008, doi: 10.1038/nature07073.

[19] G. Von and G. Lnstitute Lor Geological, "A REVIEW OF SOME RECENT CONCEPTS OF THE BUSHVELD GOMPLEX' WNN PARTICULAR REFERENCE TO SULFIDE MINERALIZATION," 1979.

[20] W. Hustrulid, W. Hustrulid, R. Bullock, and R. Bullock, *Underground mining methods: Engineering fundamentals and international case studies*. 2001.

[21] R. Ehrlich, "A century of miners' compensation in South Africa," *Am. J. Ind. Med.*, vol. 55, no. 6, pp. 560–569, Jun. 2012, doi: 10.1002/ajim.22030.

[22] R. J. Howarth, "A petrologist in South Africa: Frederick Henry Hatch and the Witwatersrand Goldfield," *Proc. Geol. Assoc.*, vol. 123, no. 1, pp. 189–209, Jan. 2012, doi: 10.1016/J.PGEOLA.2011.06.001.

[23] "USGS Scientific Investigations Report 2013–5090–Q: Platinum-Group Elements in Southern Africa—Mineral Inventory and an Assessment of Undiscovered Mineral

Resources.” .

[24] B. McCarthy, T. & Rubidge, “The Bushveld Complex - Wits University,” 2005. .

[25] “Platinum ~ Learning Geology.” .

[26] Mertie JB, “Economic geology of the platinum metals,” *Usgs P820*, 1969.

[27] “Geology of Platinum | Properties, Mining, and Formation of Platinum.” .

[28] “Platinum | Platinum | Metals.” .

[29] M. Becker, C. Brough, D. Reid, D. Smith, and D. Bradshaw, “Geometallurgical characterisation of the Merensky Reef at Northam Platinum Mine - Comparison of Normal, Pothole and Transitional reef types,” *Australas. Inst. Min. Metall. Publ. Ser.*, no. September, pp. 391–399, 2008.

[30] W. Platinum and I. Council, “Platinum Essentials October 2017.”

[31] O. S. J. Elham, S. K. Kamarudin, N. Shaari, A. M. Zainoodin, Z. Zakaria, and M. R. Yusof, “Development of Low-Cost Nafion-Lignin Composite Conductive Membranes for Application in Direct Methanol Fuel Cells,” *J. Environ. Chem. Eng.*, vol. 12, no. 1, p. 111514, 2023, doi: 10.1016/j.jece.2023.111514.

[32] F. Si, Y. Zhang, L. Yan, J. Zhu, M. Xiao, and C. Liu, “Electrochemical Oxygen Reduction Reaction,” *Rotating Electrode Methods Oxyg. Reduct. Electrocatal.*, pp. 133–170, Jan. 2014, doi: 10.1016/B978-0-444-63278-4.00004-5.

[33] V. Bambagioni *et al.*, “Pd and Pt – Ru anode electrocatalysts supported on multi-walled carbon nanotubes and their use in passive and active direct alcohol fuel cells with an anion-exchange membrane (alcohol = methanol , ethanol , glycerol),” vol. 190, pp. 241–251, 2009, doi: 10.1016/j.jpowsour.2009.01.044.

[34] S. Sen Gupta, S. S. Mahapatra, and J. Datta, “A potential anode material for the direct alcohol fuel cell,” vol. 131, pp. 169–174, 2004, doi: 10.1016/j.jpowsour.2004.01.009.

[35] O. S. . J. Elham *et al.*, “Energy Nexus From Methanol Concentration to Thermal Performance : Insight into Nafion / Lignosulfonate-Hydroxyapatite Composite Membranes for Direct Methanol Fuel,” *Energy Nexus*, vol. 19, no. July, p. 100494, 2025, doi: 10.1016/j.nexus.2025.100494.

[36] F. Ye, H. Liu, Y. Feng, J. Li, X. Wang, and J. Y. Acta, “A solvent approach to the size-controllable synthesis of ultrafine Pt catalysts for methanol oxidation in direct methanol fuel cells,” *Electrochimica*, vol. 117, pp. 480–485, 2014, doi: https://doi.org/10.1016/j.electacta.2013.11.171.

[37] W. Yuan, B. Zhou, J. Deng, Y. Tang, … Z. Z.-I. J. of, and undefined 2014, “Overview on the developments of vapor-feed direct methanol fuel cells,” *Elsevier*.

[38] V. Johánek, A. Ostroverkh, and R. Fiala, “Vapor-feed low temperature direct methanol fuel cell with Pt and PtRu electrodes: Chemistry insight,” *Renew. Energy*, vol. 138, pp. 409–415, Aug. 2019, doi: 10.1016/j.renene.2019.01.109.

[39] S. Basri, S. K. Kamarudin, W. R. W. W. Daud, Z. Yaakob, and A. A. H. H. Kadhum, “Novel anode catalyst for direct methanol fuel cells.,” *ScientificWorldJournal.*, vol. 2014, no. 547604, p. 547604, Apr. 2014, doi: 10.1155/2014/547604.

[40] X. Li, L. Luo, F. Peng, H. Wang, and H. Yu, “Enhanced activity of Pt/CNTs anode

catalyst for direct methanol fuel cells using Ni2P as co-catalyst," *Appl. Surf. Sci.*, vol. 434, pp. 534–539, 2018, doi: 10.1016/j.apsusc.2017.10.218.

[41] Y. Mu, H. Liang, J. Hu, L. Jiang, and L. Wan, "Pt–Co supported on single-walled carbon nanotubes as an anode catalyst for direct methanol fuel cells," *Electrochim. Acta*, vol. 109, no. 47, pp. 7276–7280, 2005, doi: 10.1021/jp0555448.

[42] J. Prabhuram, T. S. Zhao, Z. K. Tang, R. Chen, and Z. X. Liang, "Multiwalled carbon nanotube supported PtRu for the anode of direct methanol fuel cells," *J. Phys. Chem. B*, vol. 110, no. 11, pp. 5245–5252, 2006, doi: 10.1021/jp0567063.

[43] W. Zhou, Z. Zhou, S. Song, and W. Li, "Pt based anode catalysts for direct ethanol fuel cells," vol. 46, pp. 273–285, 2003, doi: 10.1016/S0926-3373(03)00218-2.

[44] H. Ishitobi, Y. Ino, N. N.-I. J. of H. Energy, and undefined 2017, "Anode catalyst with enhanced ethanol electrooxidation activity by effective interaction between Pt-Sn-SiO2 for a direct ethanol fuel cell," *Elsevier*.

[45] F. Vigier, C. Coutanceau, A. Perrard, E. M. Belgsir, and C. Lamy, "Development of anode catalyst for a direct methanol fuel cell veigar (2004)," pp. 439–446, 2004, doi: 10.1023/B:JACH.0000016629.98535.ad.

[46] P. K. Mohanta and F. Regnet, "Graphitized Carbon : A Promising Stable Cathode Catalyst Support Material for Long Term PEMFC Applications," 2018, doi: 10.3390/ma11060907.

[47] Q. Lijuan *et al.*, "Effect of electrode Pt-loading and cathode flow-field plate type on the degradation of PEMFC," 2018, doi: 10.1016/j.jechem.2018.09.004.

[48] M. Renzi, G. D'Angelo, R. Marassi, F. N.-J. of P. Sources, and undefined 2016, "Low platinum loading cathode modified with Cs3H2PMo10V2O40 for polymer electrolyte membrane fuel cells," *Elsevier*.

[49] N. Karthikeyan, B. Vinayan, M. Rajesh, K. B.-F. Cells, and undefined 2015, "Highly durable platinum based cathode electrocatalysts for PEMFC application using oxygen and nitrogen functional groups attached nanocarbon supports," *Wiley Online Libr*.

[50] E. S. Lett, P. A-a, L. M. Roen, C. H. Paik, and T. D. Jarvi, "Electrocatalytic Corrosion of Carbon Support in PEMFC Cathodes service Electrocatalytic Corrosion of Carbon Support in PEMFC Cathodes," vol. 7, no. 1, pp. 8–12, 2004, doi: 10.1149/1.1630412.

[51] P. Yu, M. Pemberton, and P. Plasse, "PtCo / C cathode catalyst for improved durability in PEMFCs," vol. 144, no. November 2004, pp. 11–20, 2005, doi: 10.1016/j.jpowsour.2004.11.067.

[52] M. M. Bruno, F. A. Viva, M. A. Petruccelli, and H. R. Corti, "Platinum supported on mesoporous carbon as cathode catalyst for direct methanol fuel cells," *J. Power Sources*, vol. 278, pp. 458–463, Mar. 2015, doi: 10.1016/j.jpowsour.2014.12.097.

[53] K. Makino, K. Furukawa, K. Okajima, and M. Sudoh, "Optimization of the sputter-deposited platinum cathode for a direct methanol fuel cell," *Electrochim. Acta*, vol. 51, no. 5, pp. 961–965, 2005, doi: 10.1016/j.electacta.2005.04.062.

[54] G. Wang *et al.*, "Novel synthesis of highly active Pt/C cathode electrocatalyst for direct methanol fuel cell," *Chem. Commun.*, no. 3, pp. 394–395, 2003, doi: 10.1039/b211075j.

[55] W. Li *et al.*, "Nano-stuctured Pt-Fe/C as cathode catalyst in direct methanol fuel cell," *Electrochim. Acta*, vol. 49, no. 7, pp. 1045–1055, 2004, doi: 10.1016/j.electacta.2003.10.015.

[56] B. Logan, *Microbial Fuel Cells Chapter 3 Voltage Generation*. 2008.

[57] B. Erable, M. Oliot, R. Lacroix, A. Bergel, … A. S.-E., and undefined 2018, "Iron-Nicarbazin derived platinum group metal-free electrocatalyst in scalable-size air-breathing cathodes for microbial fuel cells," *Elsevier*.

[58] M. Kodali *et al.*, "Mn Fe," *Electrochim. Acta*, 2017, doi: 10.1016/j.electacta.2017.02.033.

[59] M. Kodali, R. Gokhale, C. Santoro, A. Serov, K. Artyushkova, and P. Atanassov, "High Performance Platinum Group Metal-Free Cathode Catalysts for Microbial Fuel Cell (MFC)," vol. 164, no. 3, pp. 78–83, 2017, doi: 10.1149/2.0061703jes.

[60] M. Ghasemi, S. Shahgaldi, M. Ismail, and B. Hong, "Activated carbon nanofibers as an alternative cathode catalyst to platinum in a two-chamber microbial fuel cell," *Int. J. Hydrogen Energy*, vol. 36, no. 21, pp. 13746–13752, 2011, doi: 10.1016/j.ijhydene.2011.07.118.

[61] A. ur Rehman, M. J. Sanjari, R. M. Elavarasan, and T. Jamal, "Sustainability-aligned pathways for energy transition: A review of low-carbon energy network solutions," *Renew. Sustain. Energy Rev.*, vol. 226, p. 116428, Jan. 2026, doi: 10.1016/J.RSER.2025.116428.

[62] M. Bampaou and K. D. Panopoulos, "An overview of hydrogen valleys: Current status, challenges and their role in increased renewable energy penetration," *Renewable and Sustainable Energy Reviews*. 2025, doi: 10.1016/j.rser.2024.114923.

[63] M. Yasin *et al.*, "Pt-based electrocatalyst for hydrogen evolution in acidic electrolytes," *Electrochemistry Communications*. 2025, doi: 10.1016/j.elecom.2025.108057.

[64] R. M. A. Iqbal, M. Du, Z. U. Rehman, L. Sun, A. Munir, and F. Liu, "Surface segregation and reconstruction of core–shell electrocatalysts for water splitting," *J. Mater. Chem. A*, 2026, doi: 10.1039/D6TA01795A/1262239.

[65] L. V. Bühre, K. Khedekar, K. S. Reeves, H. Yu, S. M. Alia, and B. S. Pivovar, "The Impact of Catalyst Layer Composition and Structure on Performance and Durability of PEMWE Anodes," *Adv. Mater. Technol.*, 2025, doi: 10.1002/admt.202501870.

[66] L. MacDonald, D. Zhang, A. Alptekinoğlu, and A. K. Karamalidis, "Enhancing the Resilience of Platinum Group Metal Supply Chains: Mine to (Re)use," *Sustain. Dev.*, 2025, doi: 10.1002/sd.3499.

About MyJEA

Malaysian Journal of Energy and Applications (MyJEA) is a peer-reviewed journal published by the Fuel Cell Institute (SELFUEL), Universiti Kebangsaan Malaysia. The journal features high-quality research, innovations and reviews in clean energy systems, fuel cell science, electrochemistry and green technology applications.

Focus Areas

- Fuel cells and hydrogen energy
- Electrochemistry and catalytic materials
- Energy conversion and storage
- Green technology applications

Published by:

Fuel Cell Institute (SELFUEL)
Universiti Kebangsaan Malaysia
43600 UKM Bangi, Selangor, Malaysia

www.ukm.my/myjea

ISSN 2838-0037 (Print)

ISSN 3154-8016 (Online)